Electronic Supplementary Information

Computer-aided design of high-efficiency GeTe-based thermoelectric devices

Min Hong,[a,b] Kun Zheng,[c] Wanyu Lyv,[b] Meng Li,[a] Xianlin Qu,[c] Qiang Sun,[a] Shengduo Xu,[a] Jin Zou,[*,a,d] and Zhi-Gang Chen[*,a,b]

a Centre for Future Materials, University of Southern Queensland, Springfield, Queensland 4300, Australia.

b School of Mechanical and Mining Engineering, The University of Queensland, Brisbane, Queensland 4072, Australia.

c Beijing Key Lab of Microstructure and Property of Solids, Institute of Microstructure and Properties of Advanced Materials, Beijing University of Technology, Beijing, 100124, China.

d Centre for Microscopy and Microanalysis, The University of Queensland, Brisbane, Queensland 4072, Australia.

*Email: zhigang.chen@usq.edu.au (Z. G. C.); zhigang.chen@uq.edu.au (Z. G. C.); j.zou@uq.edu.au (J. Z.)

1. Details of modeling study based on the Kane energy relation

Thermoelectric properties of single-band Kane model are given by [1]

Seebeck coefficient

$$S=\frac{k_B}{e}\left[\frac{F_{1,-2}^{1}(\eta,\beta)}{F_{1,-2}^{0}(\eta,\beta)}-\eta\right],$$ * MERGEFORMAT (S1)

Hall carrier concentration

$$n_H=\frac{N\left(2m_b^*k_BT\right)^{\frac{3}{2}}}{3\pi^2\hbar^3}\frac{F_{3/2,0}^{0}(\eta,\beta)}{A},$$ * MERGEFORMAT (S2)

Hall carrier mobility

$$\mu_H=A\frac{2\pi\hbar^4eC_l}{m_I^*\left(2m_b^*k_BT\right)^{3/2}E_{def}^2}\frac{3F_{1,-2}^{0}(\eta,\beta)}{F_{3/2,0}^{0}(\eta,\beta)},$$ * MERGEFORMAT (S3)

Hall factor

$$A=\frac{3K(K+2)}{(2K+1)^2}\frac{F_{1/2,-4}^{0}F_{3/2,0}^{0}}{\left(F_{1,-2}^{0}\right)^2},$$ * MERGEFORMAT (S4)

Electrical conductivity

$$\sigma=n_H\mu_He=\frac{2e^2N\hbar C_l}{\pi m_I^*E_{def}^2}F_{1,2}^{0}(\eta,\beta),$$ * MERGEFORMAT (S5)

Generalized Fermi integration

$$F_{m,k}^{n}(\eta,\beta)=\int_0^\infty\left[-\frac{\partial f(\eta)}{\partial\varepsilon}\right]\varepsilon^n\left(\varepsilon+\beta\varepsilon^2\right)^m\left[(1+2\beta\varepsilon)^2+2\right]^{\frac{k}{2}}d\varepsilon,$$ * MERGEFORMAT

(S6)

Electrical thermal conductivity is calculated according to the Wiedemann–Franz law, namely

$$\kappa_e=L\sigma T,$$ * MERGEFORMAT (S7)

with L representing the Lorenz number, and give by

$$L=\left(\frac{k_B}{e}\right)^2\left[\frac{F_{1,-2}^{2}(\eta,\beta)}{F_{1,-2}^{0}(\eta,\beta)}-\left(\frac{F_{1,-2}^{1}(\eta,\beta)}{F_{1,-2}^{0}(\eta,\beta)}\right)^2\right]. \text{* MERGEFORMAT (S8)}$$

In the above equations, η is the reduced Fermi level, $\beta=\frac{k_BT}{E_g}$ (E_g is the band gap) is the reciprocal reduced band gap, k_B is Boltzmann constant, e is the elementary charge, N is the band degeneracy, $\hbar$ is the reduced Planck constant, C_l is the combination of elastic constants, m* I is the inertial effective mass, and E_{def} is the deformation potential, respectively [2,3]. Based on these equations, we calculate L, E_{def}, and m* d from the measured thermoelectric properties.

2. Phase examination

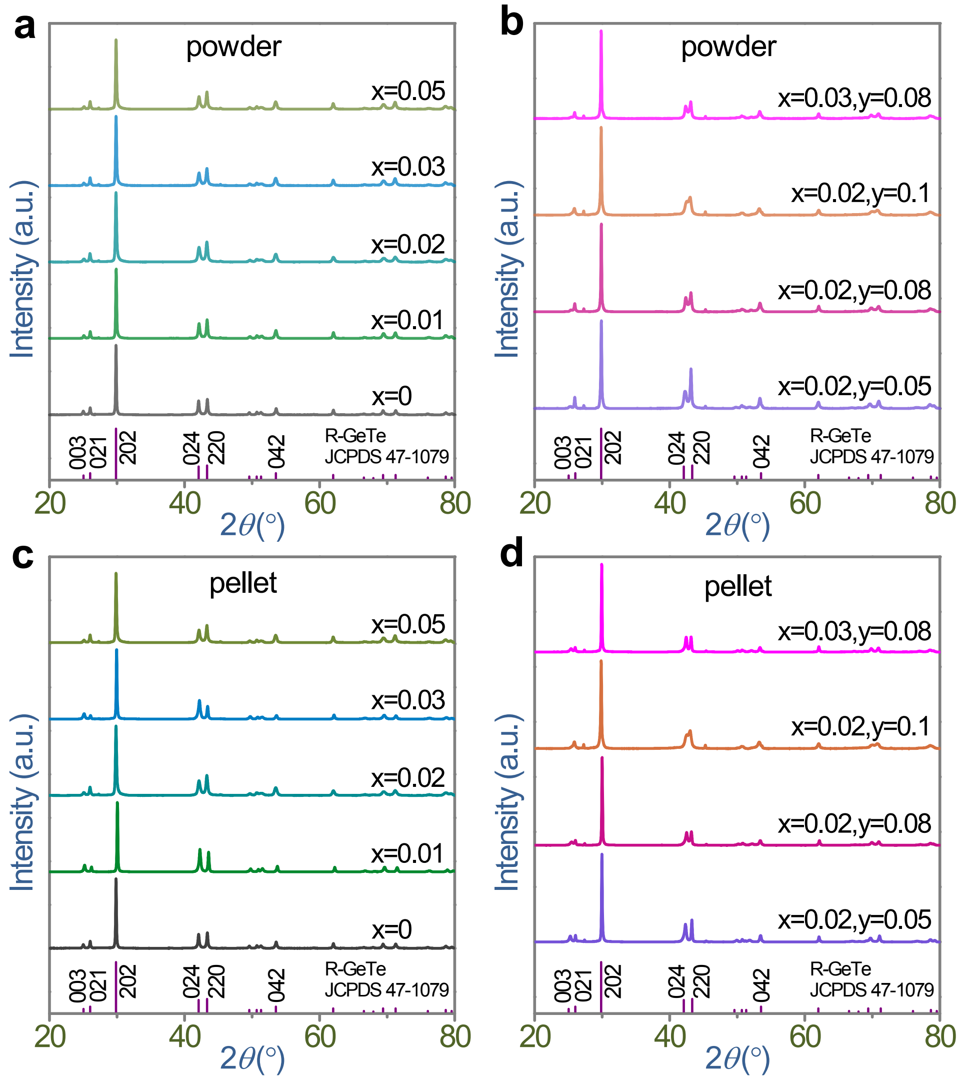

Fig. S1 XRD patterns collected from as-synthesized $Ge_{1-x-y}Cr_xSb_yTe$ (a)(b) powders and (c)(d) sintered pellets by SPS.

3. Thermoelectric properties

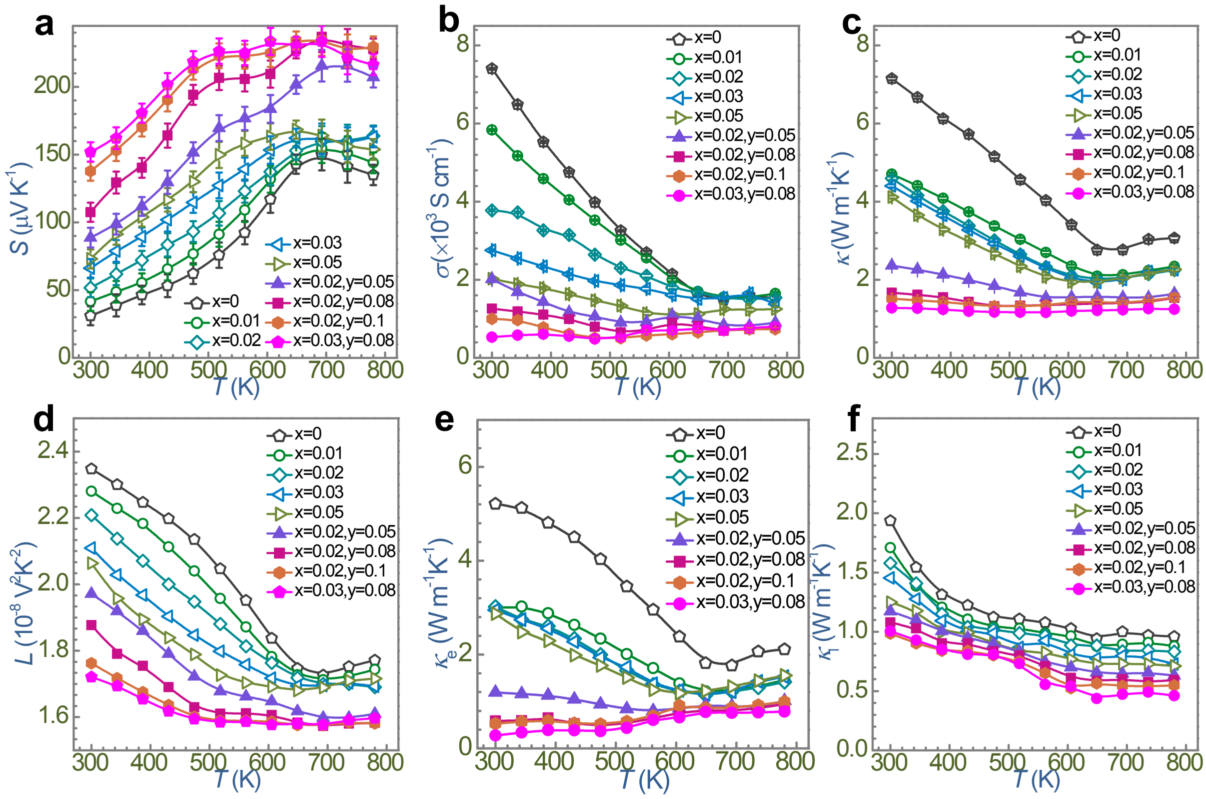

Fig. S2 Measured temperature-dependent (a) Seebeck coefficient (S), (b) electrical conductivity (σ), and (c) thermal conductivity (κ) for $Ge_{1-x-y}Cr_xSb_yTe$. Determined (d) Lorenz number (L), (e) electrical thermal conductivity (κ_e), (f) lattice thermal conductivity (κ_l).

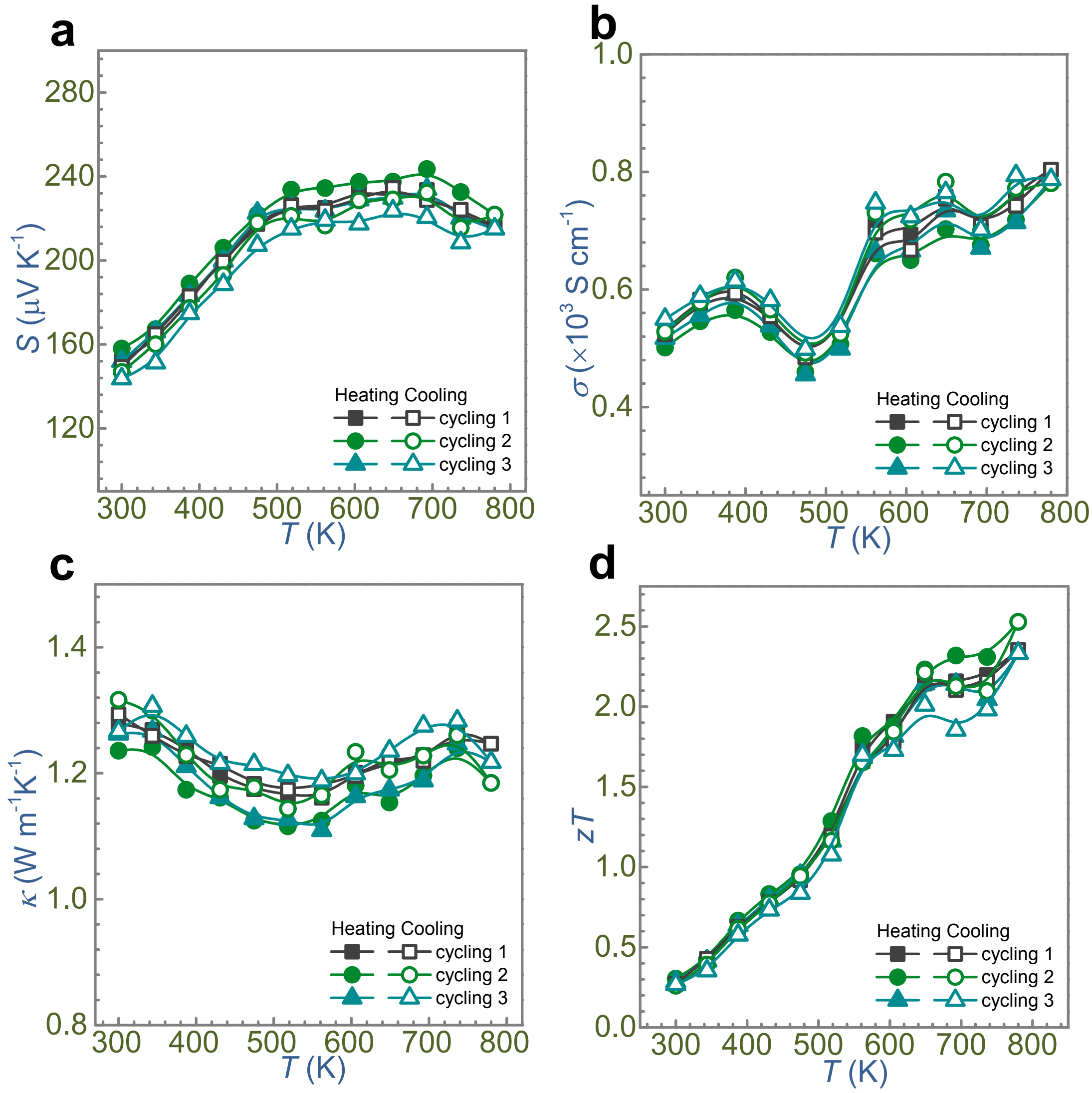

Fig. S3 Temperature-dependent (a) *S*, (b) *σ*, (c) *κ*, and (d) *zT* for $Ge_{0.89}Cr_{0.03}Sb_{0.08}Te$ measured through three heating-cooling cycles to test the thermal stability.

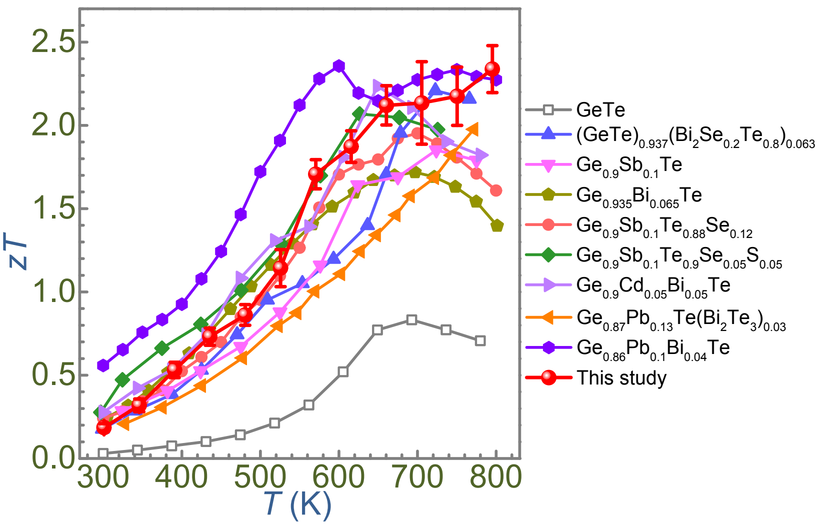

Fig. S4 Comparison of obtained highest zT in this study with the reported values for $(GeTe)_{0.937}(Bi_2Se_{0.2}Te_{0.8})_{0.063}$,[4] $Ge_{0.9}Sb_{0.1}Te$,[5] $Ge_{0.935}Bi_{0.065}Te$,[6] $Ge_{0.9}Sb_{0.1}Te_{0.88}Se_{0.12}$,[7] $Ge_{0.9}Sb_{0.1}Te_{0.9}Se_{0.05}S_{0.05}$,[8] $Ge_{0.9}Cd_{0.05}Bi_{0.05}Te$,[9] $Ge_{0.87}Pb_{0.13}Te(Bi_2Te_3)_{0.03}$,[10] and $Ge_{0.86}Pb_{0.1}Bi_{0.04}Te$.[11] The zT of GeTe is from this study.

4. Simulation results of geometry optimization

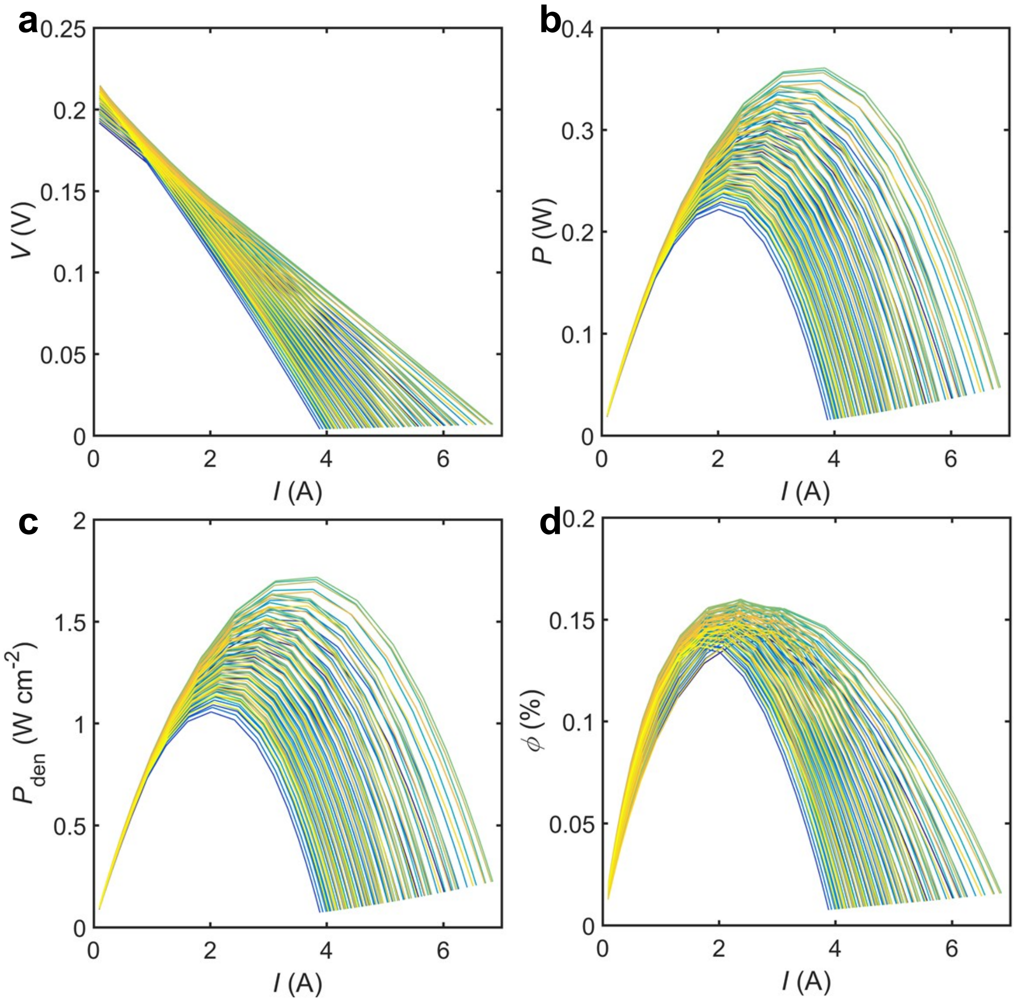

Fig. S5 During the geometry optimization of the segmented thermoelectric device with length ratios of *n*-type ($ratio_n$) and *p*-type ($ratio_p$) legs, the generated (a) voltage (V), (b) electrical output power (P), (c) electrical output power density (P_{den}), and (d) conversion efficiency (ϕ) as a function of electrical current (I).

5. More unfolded band structures

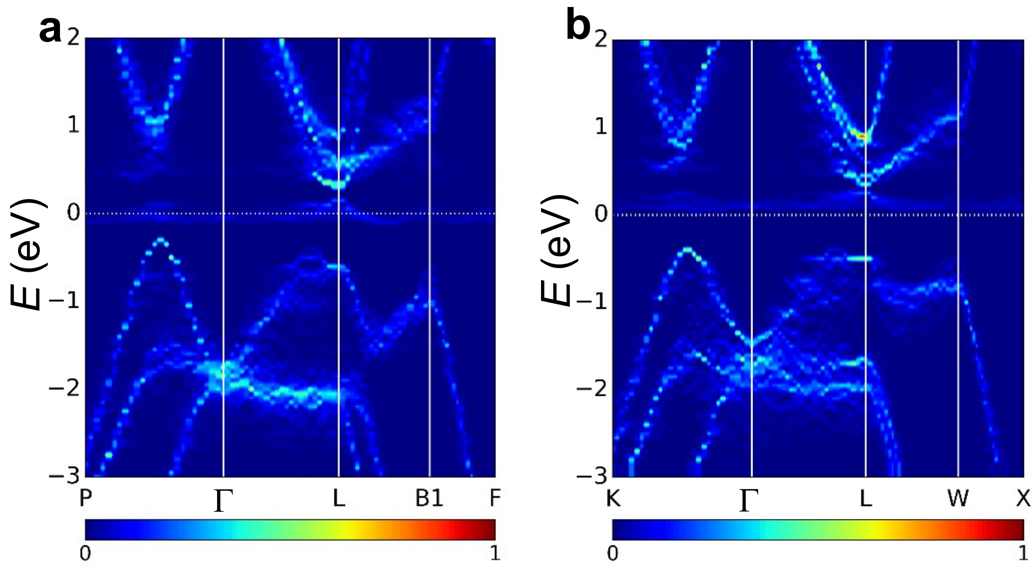

Fig. S6 Unfolded band structures into the primitive cells of (a) rhombohedral (R-) and (b) cubic (C-) $Ge_{60}Cr_3Te_{64}$.

6. Hall measurement results

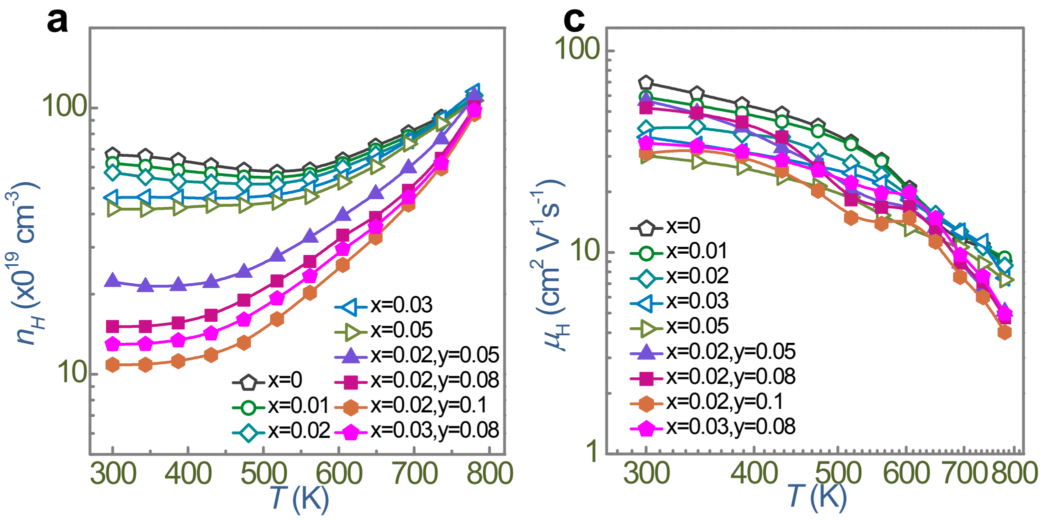

Fig. S7 Measured temperature-dependent (a) Hall carrier concentration (n_H) and (b) Hall carrier mobility (μ_H) of $Ge_{1-x-y}Cr_xSb_yTe$.

7. Determined parameters

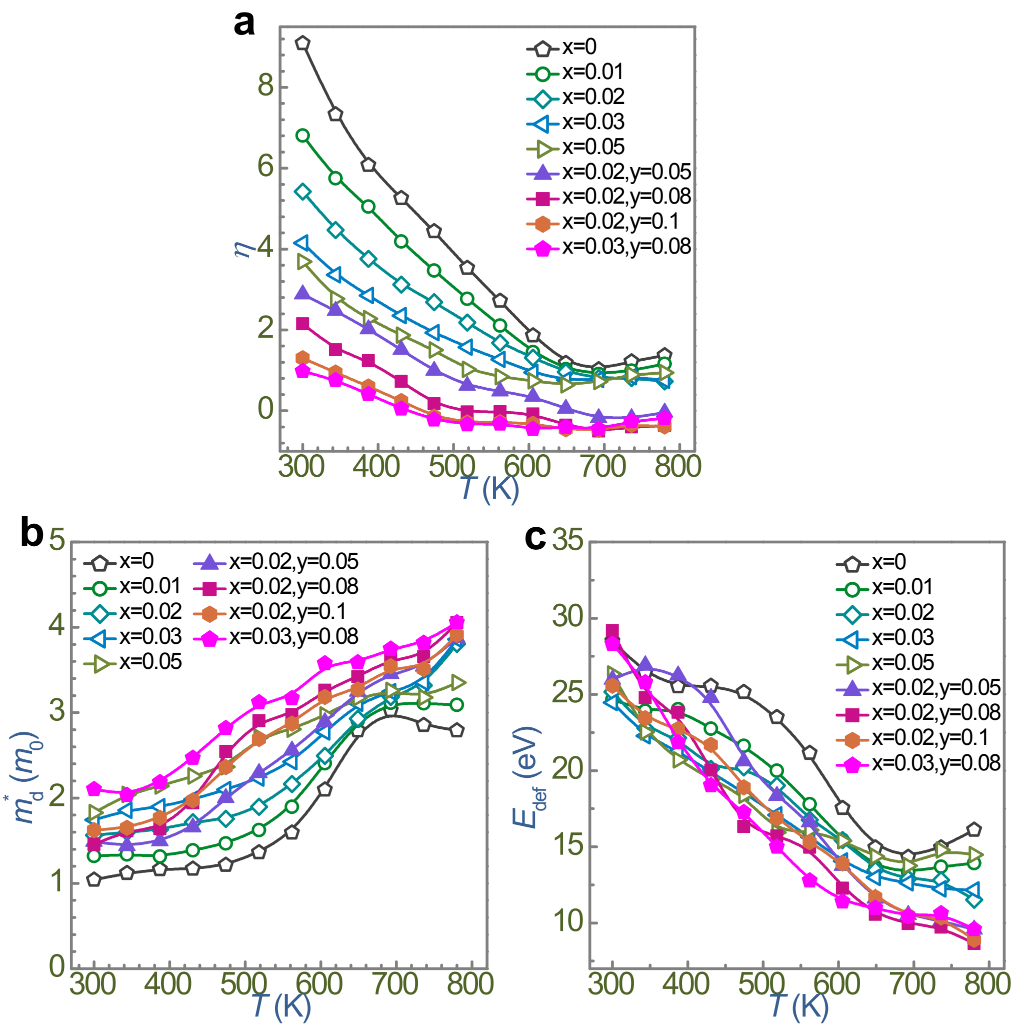

Fig. S8 Calculated (a) reduced Fermi level (η), (b) density-of-states effective mass (m^* d), and (c) deformation potential (E_{def}) of $Ge_{1-x-y}Cr_xSb_yTe$.

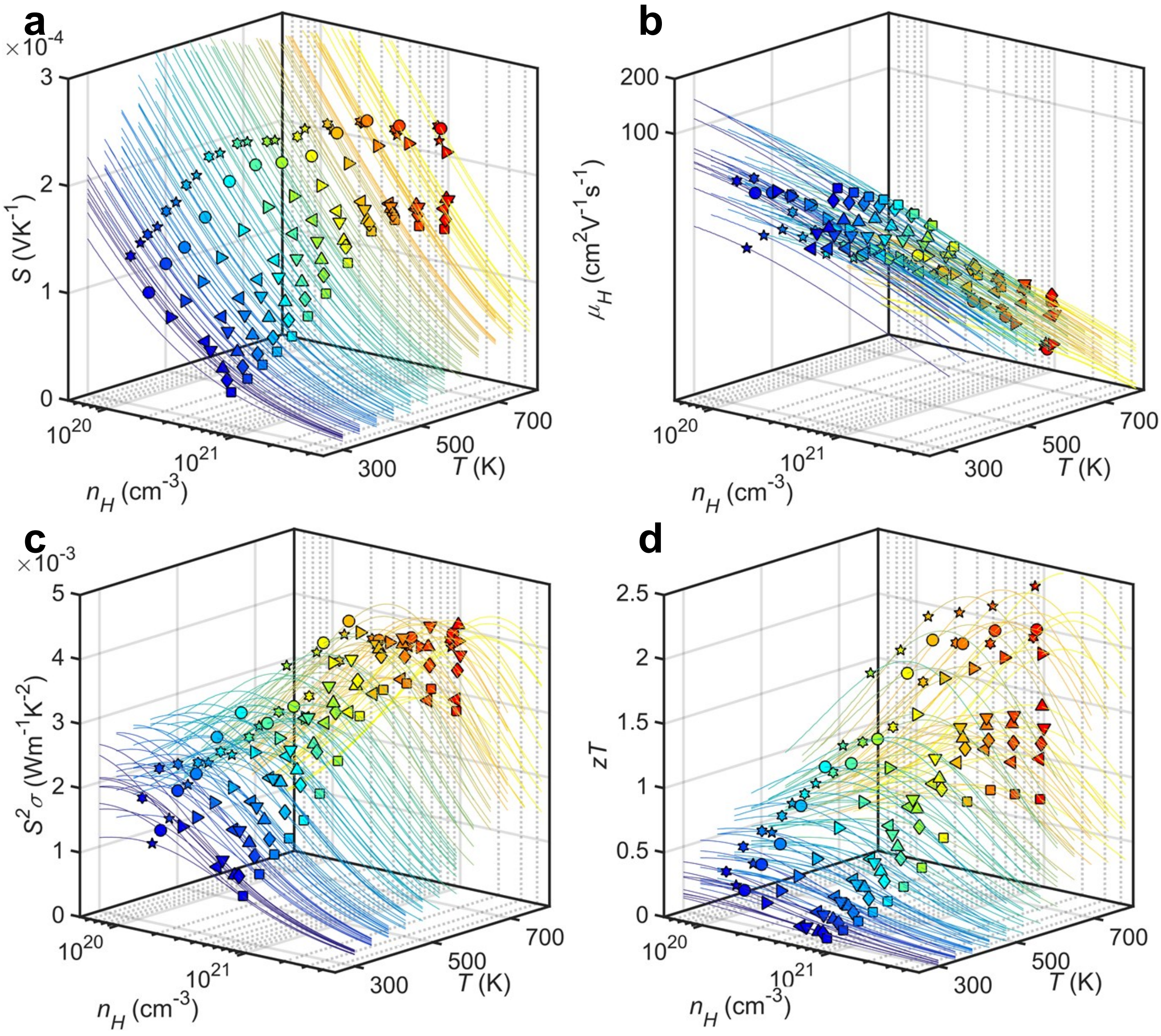

Fig. S9 Calculated curves of (a) S, (b) μ_H, (c) $S^2\sigma$, and (d) zT as functions of n_H and temperature, compared with the corresponding data points for $Ge_{1-x-y}Cr_xSb_yTe$.

8. More TEM results taken from sintered $Ge_{0.89}Cr_{0.03}Sb_{0.08}Te$ pellet

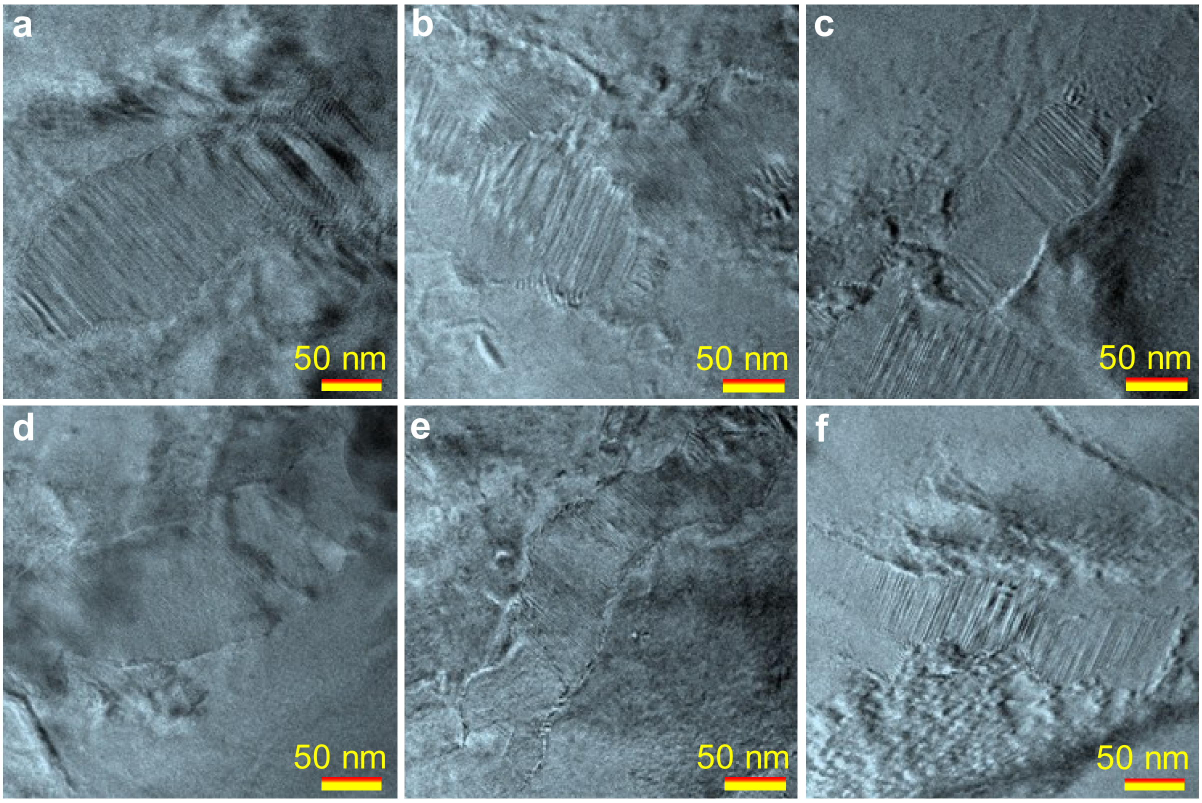

Fig. S10 TEM images taken from the sintered $Ge_{0.89}Cr_{0.03}Sb_{0.08}Te$ to demonstrate the widely existed superlattice precipitates.

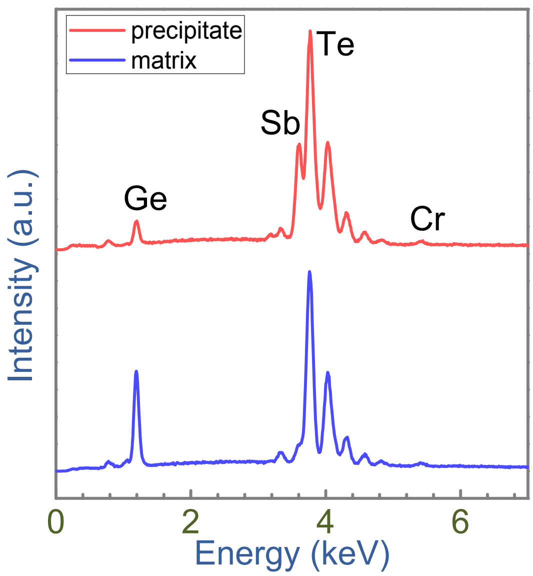

Fig. S11 Energy-dispersive X-ray spectrometry (EDS) spectra taken from the matrix (blue) and the nanoprecipitate (red).

9. FEA simulation results

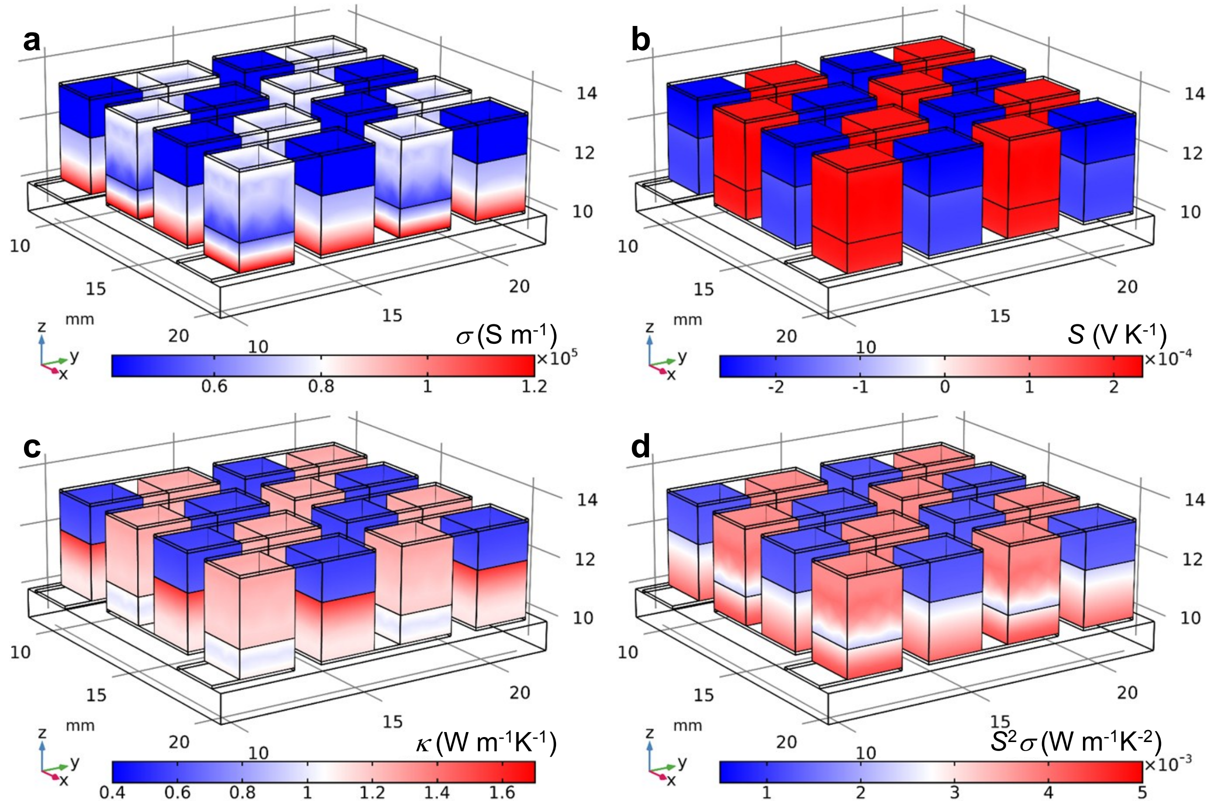

Fig. S12 Module simulation results of the thermoelectric device made of the *p*-type leg of GT ($Ge_{1-x-y}Cr_xSb_yTe$, developed in this study) and BT ($Bi_{0.5}Sb_{1.5}Te_3$)[12] and the *n*-type leg of MS ($Mg_3Sb_{1.48}Bi_{0.48}Te_{0.04}$)[13] and BT ($Bi_2Te_{2.79}Se_{0.21}$).[14] (a) S, (b) σ, (c) κ, and (d) $S^2\sigma$ profiles along the thermoelectric legs.

10. Library of thermoelectric device development

Table S1 Simulation results of the device made of as-develped p-type $Ge_{0.89}Cr_{0.03}Sb_{0.08}Te$ and reported n-type materials.

Materials	zT_{max}	T (K)	P_{max} (W)	$P_{den\text{-}max}$ (Wcm^{-2})	ϕ_{max} (%)
$Ge_{0.3}Si_{0.7}$[15]	1.1	1120	2.81	1.88	8.30
GeSe[16]	1.3	1123	2.30	1.53	10.02
$Yb_{0.3}Co_4Sb_{12}$[17]	1.3	850	3.27	2.18	10.92
$In_{0.276}Co_4Sb_{11.9}$[18]	1.2	750	3.55	2.37	12.83
$Ce_{0.17}Co_4Sb_{12}$[19]	1.3	850	3.35	2.24	11.25
$Ba_{0.3}In_{0.3}Co_4Sb_{12}$-$(BaFe_{12}O_{19})_{0.0035}$[20]	1.64	850	3.55	2.37	13.69
$Ba_{0.3}In_{0.3}Co_4Sb_{12}$-$Co_{0.002}$[21]	1.8	850	3.59	2.39	13.21
$Yb_{0.3}Co_4Sb_{12.2}$[22]	1.46	825	3.74	2.49	12.94
$In_{0.2}Ce_{0.15}Co_4Sb_{12}$/InSb[23]	1.5	800	3.50	2.33	13.49
$Co_4Sb_{11.3}Te_{0.58}Se_{0.12}$[24]	1.11	800	3.18	2.12	11.10
$Ba_{0.08}La_{0.05}Yb_{0.04}Co_4Sb_{12}$[25]	1.7	850	3.42	2.28	12.64
$Ba_8Ga_{16-x}Ge_{30+x}$[26]	0.9	860	1.84	1.23	10.82
$YbxCo_4Sb_{12}$[27]	1.3	850	3.64	2.43	12.47
$Ti_{0.95}Mn_{0.05}NiSn_{0.95}Sb_{0.05}$[28]	0.45	867	2.73	1.82	6.49
Hf_xZr_{1-x} $NiSn_{0.99}Sb_{0.01}$[29]	1	872	3.44	2.30	9.72
$Hf_{0.75}Zr_{0.25}NiSn_{0.99}Sb_{0.01}$[30]	1	900	3.32	2.21	9.64
$Zr_{0.5}Hf_{0.5}NiSn_{0.985}Sb_{0.015}$[31]	1.1	950	3.35	2.23	9.94
$Zr_{0.2}Hf_{0.8}NiSn_{0.985}Sb_{0.015}$[32]	1.1	960	3.20	2.13	8.75

$Nb_{0.8}Co_{0.92}Ni_{0.08}Sb$[33]	1.2	1100	2.25	1.50	9.09
ZrNiSn[34]	0.8	850	2.20	1.46	6.38
Br-doepd SnSe[35]	2.8	770	1.19	0.79	10.55
Bi-doped SnSe[36]	2.2	770	1.71	1.14	13.45
$Pb_{1.002}Se_{0.9982}Br_{0.0018}$[37]	1.2	850	2.54	1.69	11.56
$PbS_{0.9978}Cl_{0.0022}$[38]	0.7	850	2.35	1.57	10.79
$Pb_{0.95}SeSb_{0.033}$[39]	1.67	900	2.17	1.45	12.94
$PbIn_{0.005}Se$[40]	1.2	880	2.38	1.59	10.43
$Pb_{0.9925}Cr_{0.0075}Se$[41]	1	573	2.20	1.46	12.62
$PbTe_{0.9988}I_{0.0012}$[42]	1.4	730	2.97	1.98	13.39
$PbS(Bi_2S_3)_{0.01}(PbCl_2)_{0.01}$[43]	1.1	923	1.84	1.23	9.38
PbTe+8% PbS[44]	1.2	620	2.26	1.50	13.68
$PbTe_{0.9}S_{0.1}$ +3% Ag_2Te[45]	1.2	775	0.97	0.65	7.62
$Sb_{0.004}Pb_{0.996}Te_{0.88}S_{0.12}$[46]	1.2	678	1.40	0.93	10.69
$(Bi_{0.001}Pb_{0.999}Te)_{0.88}(PbS)_{0.12}$[47]	1.2	676	1.96	1.31	13.48
2mol%ZnTe+0.025mol%PbI_2 +PbTe[48]	1.35	650	2.86	1.91	14.50
$Pb_{0.99}SeAl_{0.01}$[49]	1.3	860	2.45	1.63	12.85
PbSe+16%PbS[50]	1.3	850	2.31	1.54	12.00
$PbTe_{0.998}T_{0.002}$-3%Sb[51]	1.8	773	3.05	2.03	13.68
$Pb_{1-x}La_xTe$[2]	1.2	830	2.62	1.75	11.11
$(Pb_{0.93}Sn_{0.07})(Te_{0.93}Se_{0.07})$[52]	1.4	780	2.45	1.63	12.00
PbTe–4%MnTe[53]	1.6	770	2.56	1.71	13.75
$Pb_{0.988}Sb_{0.012}Te$–3%GeTe[54]	1.36	770	2.23	1.49	13.57

PbTe-4%InSb[55]	1.83	760	2.26	1.50	11.56
$AgPb_mSbTe_{2+m}$[56]	2.2	560	3.03	2.02	14.87
$Pb_{0.9955}Sb_{0.0045}Se$–12%GeSe[57]	1.54	815	2.20	1.47	13.06
PbTe-5.5%Cu_2Te[58]	1.53	770	2.72	1.81	11.99
$Mg_2Sn_{0.75}Ge_{0.25}$[59]	1.4	723	3.73	2.49	12.76
$Mg_2Si_{0.3}Sn_{0.7}Sb_{0.006}$[60]	1.3	700	3.92	2.62	14.17
$Mg_2Sn_{0.78}Ge_{0.2}Sb_{0.02}$[61]	1.4	723	3.74	2.49	12.69
Sb-doped $Mg_2Si_{0.5}Sn_{0.5}$[62]	1.63	615	2.66	1.77	14.74
Sb-doped $Mg_2Si_{0.3}Sn_{0.7}$[63]	1.2	750	3.51	2.34	12.78
Sb-doped $Mg_2Si_{0.4}Sn_{0.6}$[64]	1	760	3.00	2.00	10.79
$Mg_3Sb_{0.6}Bi_{1.4}$[65]	1.2	500	2.75	1.84	14.72
$Mg_{3+\delta}Sb_{1.49}Bi_{0.5}$Te0.01[66]	1.3		2.46	1.64	15.03
Bi_2Te_3[67]	0.91	350	1.73	1.15	13.91
$(Bi_2Te_3)_{0.85}(Bi_2Se_3)_{0.15}$[68]	0.71	480	1.81	1.21	12.83
$Bi_2(Te_{1-x}Se_x)_3$-I(0.08%)[69]	1.1	340	2.67	1.78	13.58
$Cu_{0.01}Bi_2Te_{2.7}Se_{0.3}$[70]	1.1	373	2.72	1.81	14.88
$Bi_2Te_{2.79}Se_{0.21}$[14]	1.2	357	2.90	1.93	14.32
$Bi_2Te_{2.7}Se_{0.3}$[71]	1.04	398	2.57	1.71	13.75
$AgIn_5Se_8$[72]	0.72	750	3.93	2.62	20.13
$Ag_{0.9}InZn_{0.1}Se_2$[73]	1.05	810	0.61	0.41	6.63
$Ag_{0.96}Nb_{0.04}BiSe_2$[74]	1	850	0.68	0.45	6.22
$(GeSe)_{0.5}(AgBiSe_2)_{0.5}$[75]	0.5	720	0.51	0.34	5.20
$In_4Se_{2.35}$[76]	1	700	1.93	1.29	13.74
$K_{0.95}Pb_{20}Sb_{1.2}Te_{22}$[77]	1.6	700	1.27	0.84	10.11

$Ag_{0.4}Pb_{22.5}SbTe_{20}$[78]	1.5	720	2.10	1.40	12.41
$AgPb_{20}SbTe_{20}$[79]	1.2	600	1.60	1.07	11.16
$AgPb_{18}SbSe_{19.928}Cl_{0.072}$[80]	1.3	870	0.80	0.53	6.41
$AgPb_{22.5}SbTe_{20}$[81]	1.54	680	1.75	1.17	11.58
Ge-doped $AgBiSe_2$[82]	1	680	1.20	0.80	8.99
$Ag_2Se_{0.5}Te_{0.5}$[83]	1	500	0.69	0.46	7.33
$Ag_2Se_{1.08}$[84]	1	400	2.04	1.36	14.31

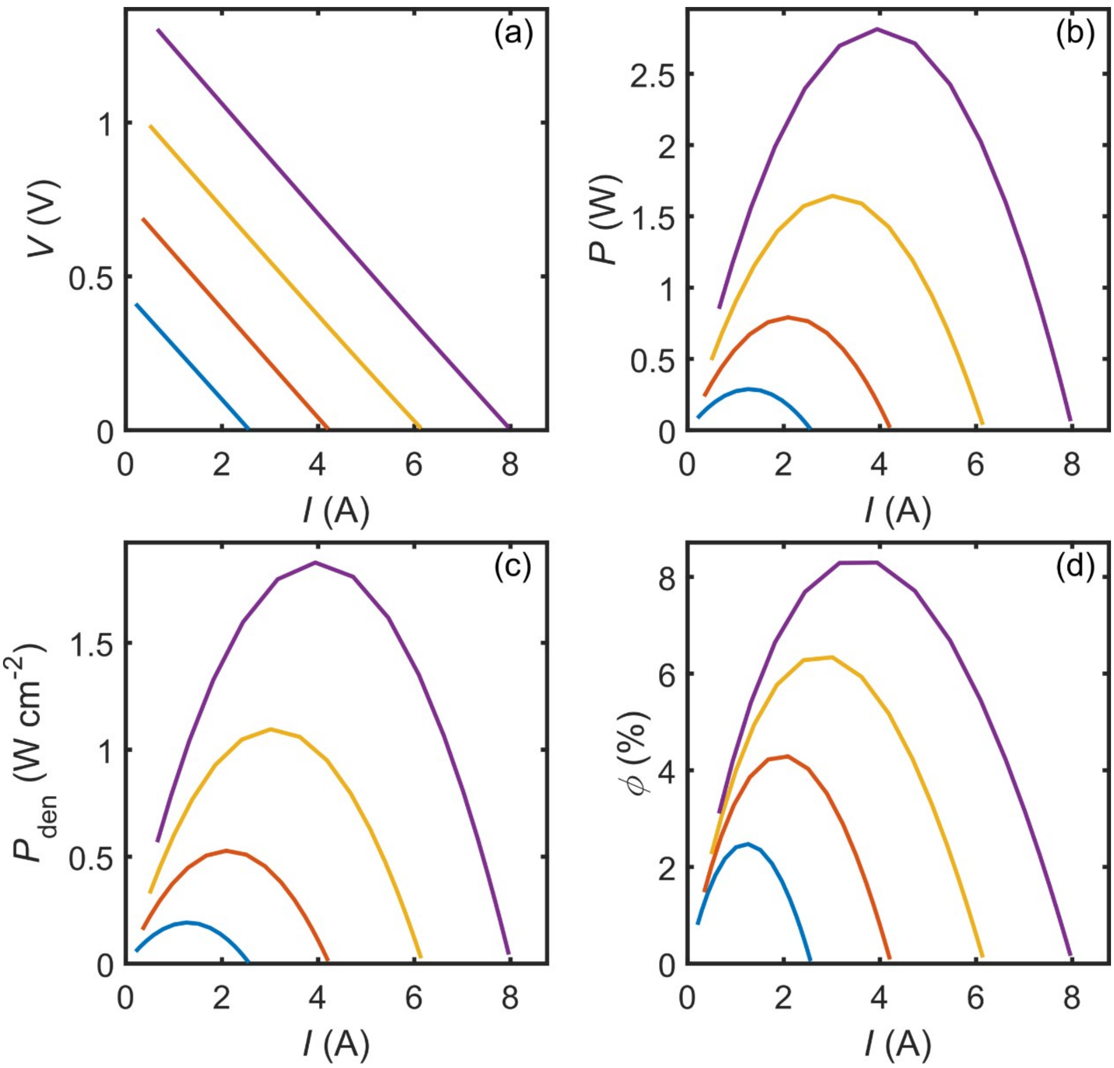

Fig. S13 Device simulation results of as-developed p-type $Ge_{0.89}Cr_{0.03}Sb_{0.08}Te$ and reported n-type $Ge_{0.3}Si_{0.7}$.[15] Generated (a) voltage (V), (b) output electrical power (P), (c) output electrical power density (P_{den}), and (d) conversion efficiency (ϕ) of the module under cold side temperature of 300 K and hot side temperatures of 480, 580, 680, and 780 K.

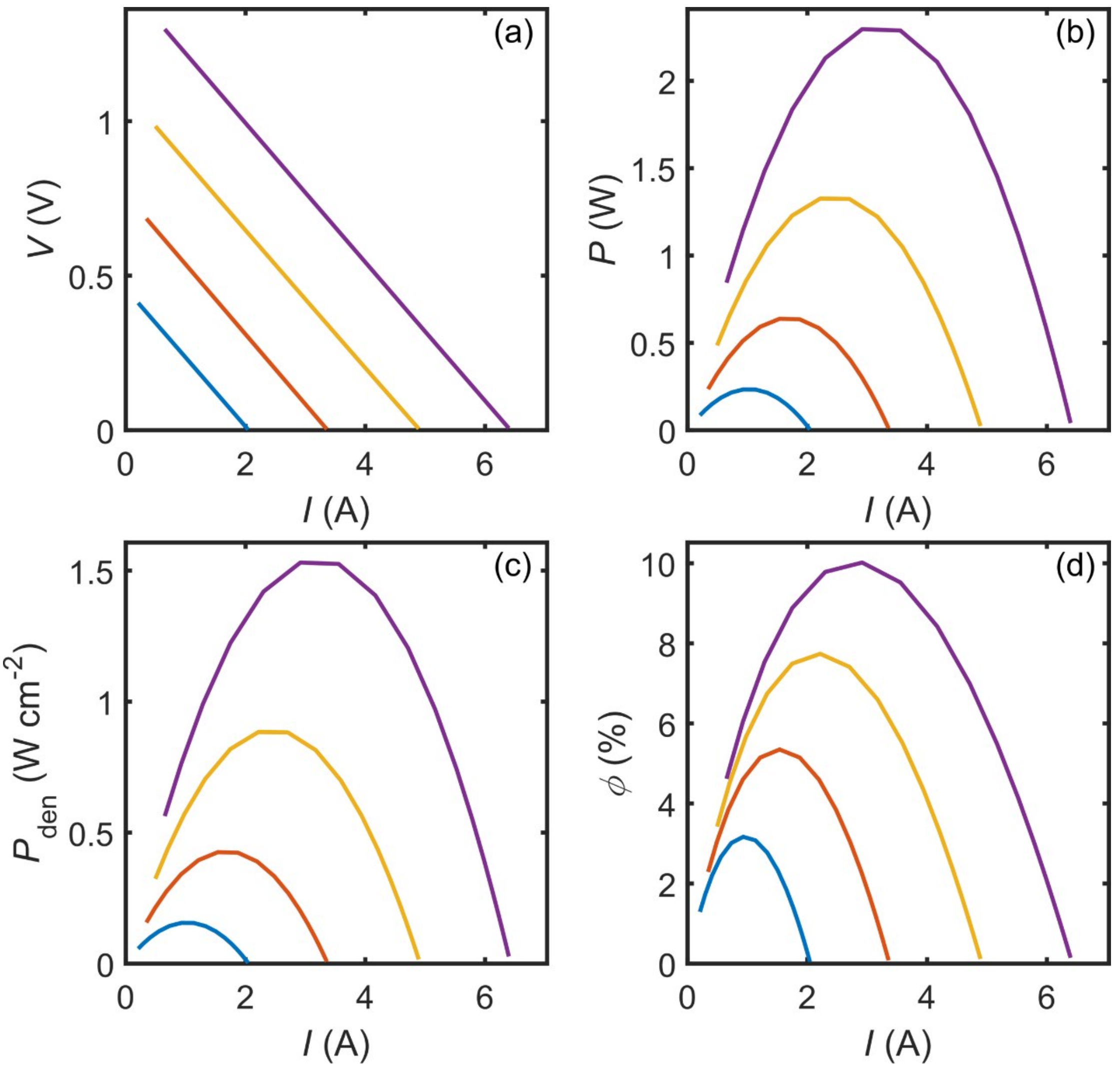

Fig. S14 Device simulation results of as-developed p-type $Ge_{0.89}Cr_{0.03}Sb_{0.08}Te$ and reported n-type GeSe.[16] Generated (a) voltage (V), (b) output electrical power (P), (c) output electrical power density (P_{den}), and (d) conversion efficiency (ϕ) of the module under cold side temperature of 300 K and hot side temperatures of 480, 580, 680, and 780 K.

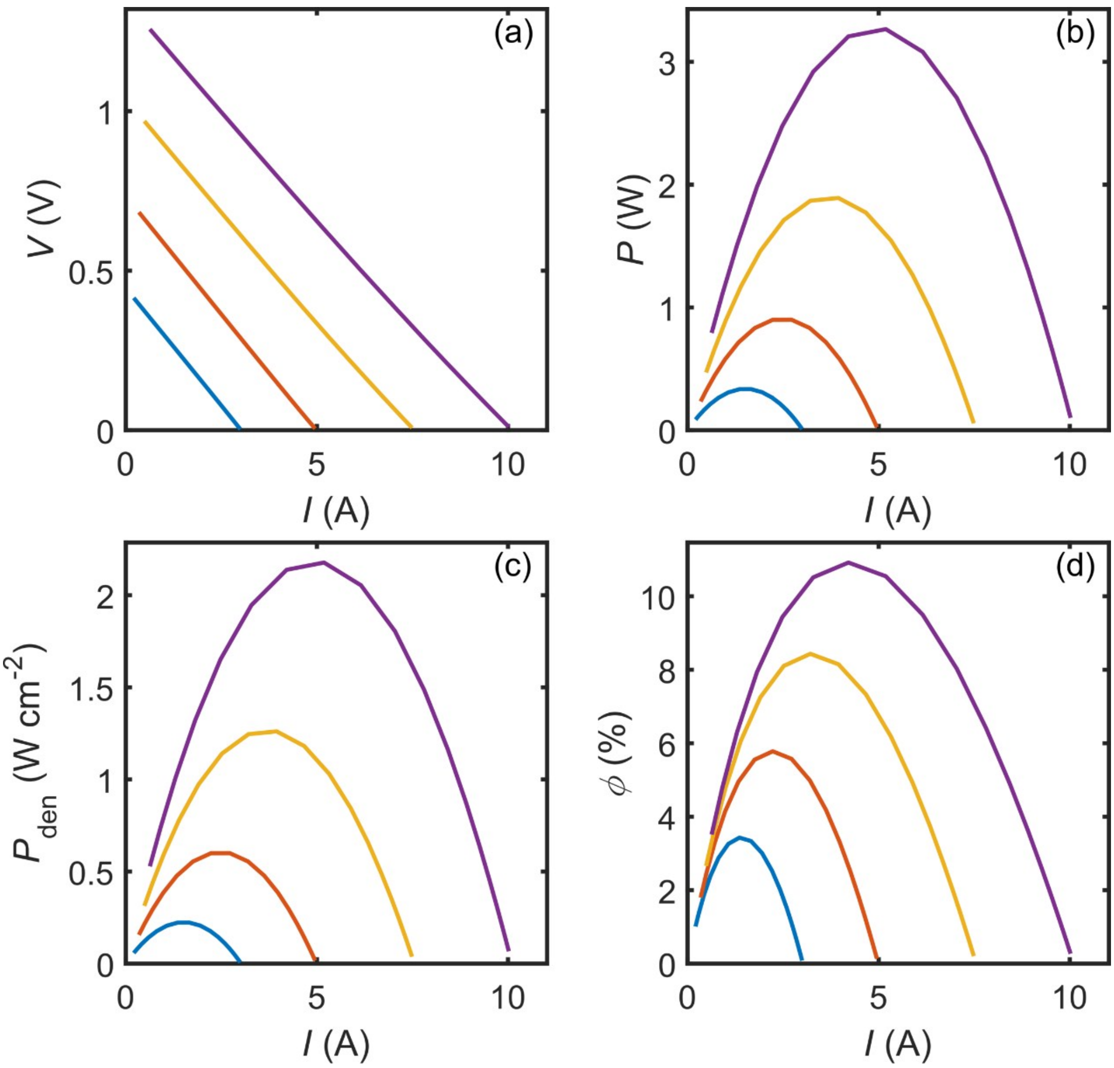

Fig. S15 Device simulation results of as-developed p-type $Ge_{0.89}Cr_{0.03}Sb_{0.08}Te$ and reported n-type $Yb_xCo_4Sb_{12}$ x=0.25, 0.3.[17] Generated (a) voltage (V), (b) output electrical power (P), (c) output electrical power density (P_{den}), and (d) conversion efficiency (ϕ) of the module under cold side temperature of 300 K and hot side temperatures of 480, 580, 680, and 780 K.

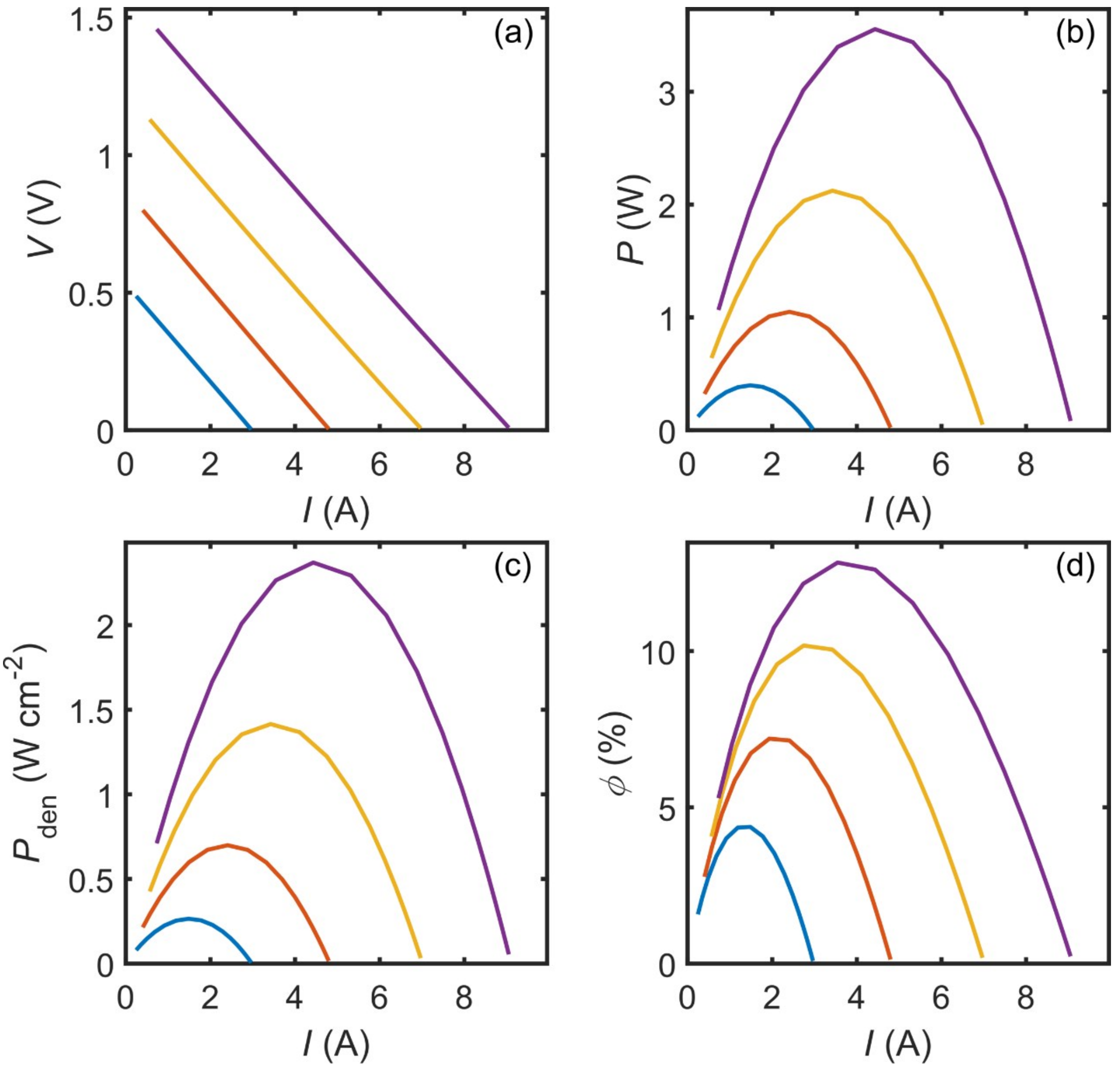

Fig. S16 Device simulation results of as-developed p-type $Ge_{0.89}Cr_{0.03}Sb_{0.08}Te$ and reported n-type $In_{0.276}Co_4Sb_{11.9}$.[18] Generated (a) voltage (V), (b) output electrical power (P), (c) output electrical power density (P_{den}), and (d) conversion efficiency (ϕ) of the module under cold side temperature of 300 K and hot side temperatures of 480, 580, 680, and 780 K.

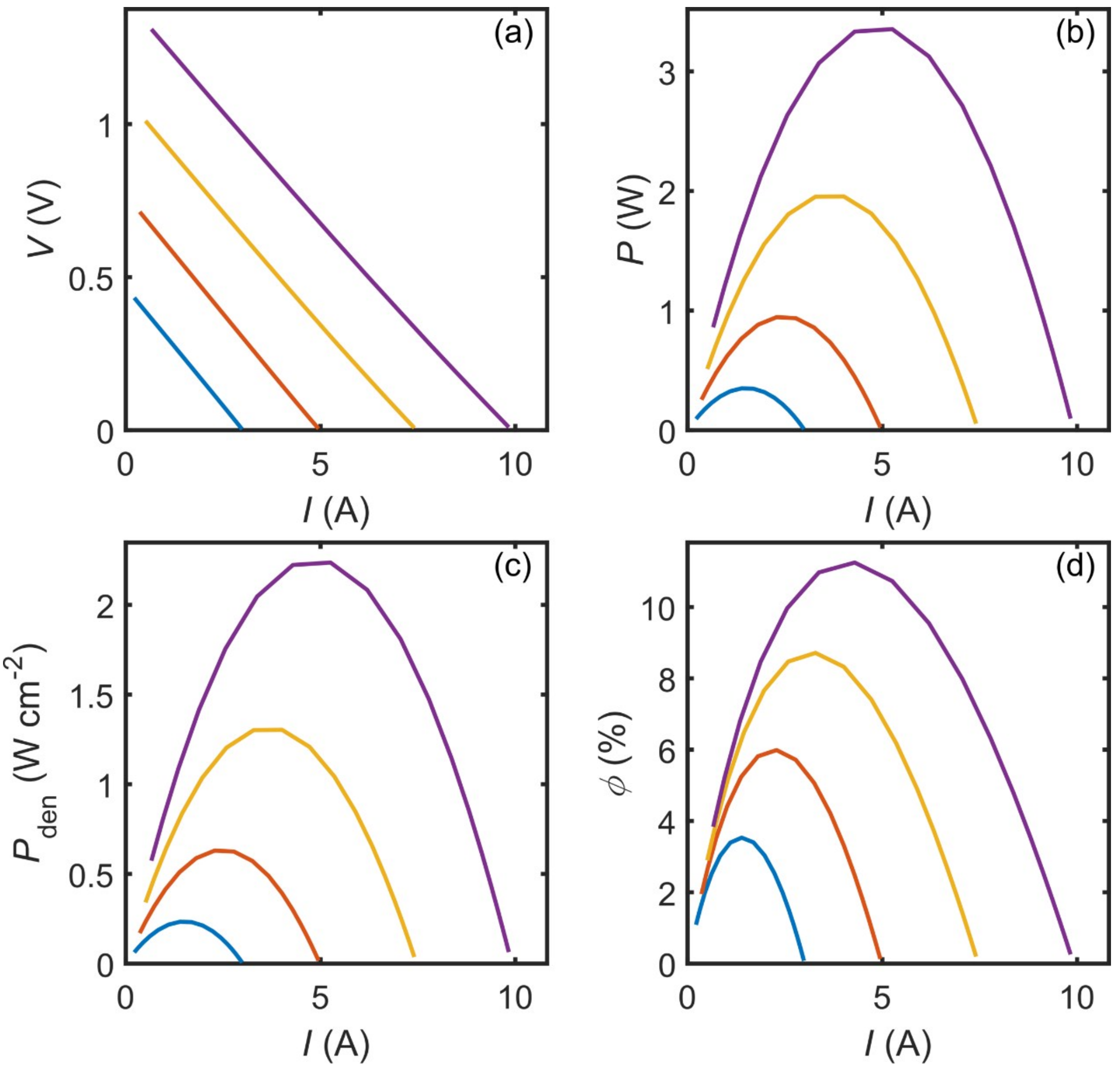

Fig. S17 Device simulation results of as-developed p-type $Ge_{0.89}Cr_{0.03}Sb_{0.08}Te$ and reported n-type $Ce_{0.17}Co_4Sb_{12}$.[19] Generated (a) voltage (V), (b) output electrical power (P), (c) output electrical power density (P_{den}), and (d) conversion efficiency (ϕ) of the module under cold side temperature of 300 K and hot side temperatures of 480, 580, 680, and 780 K.

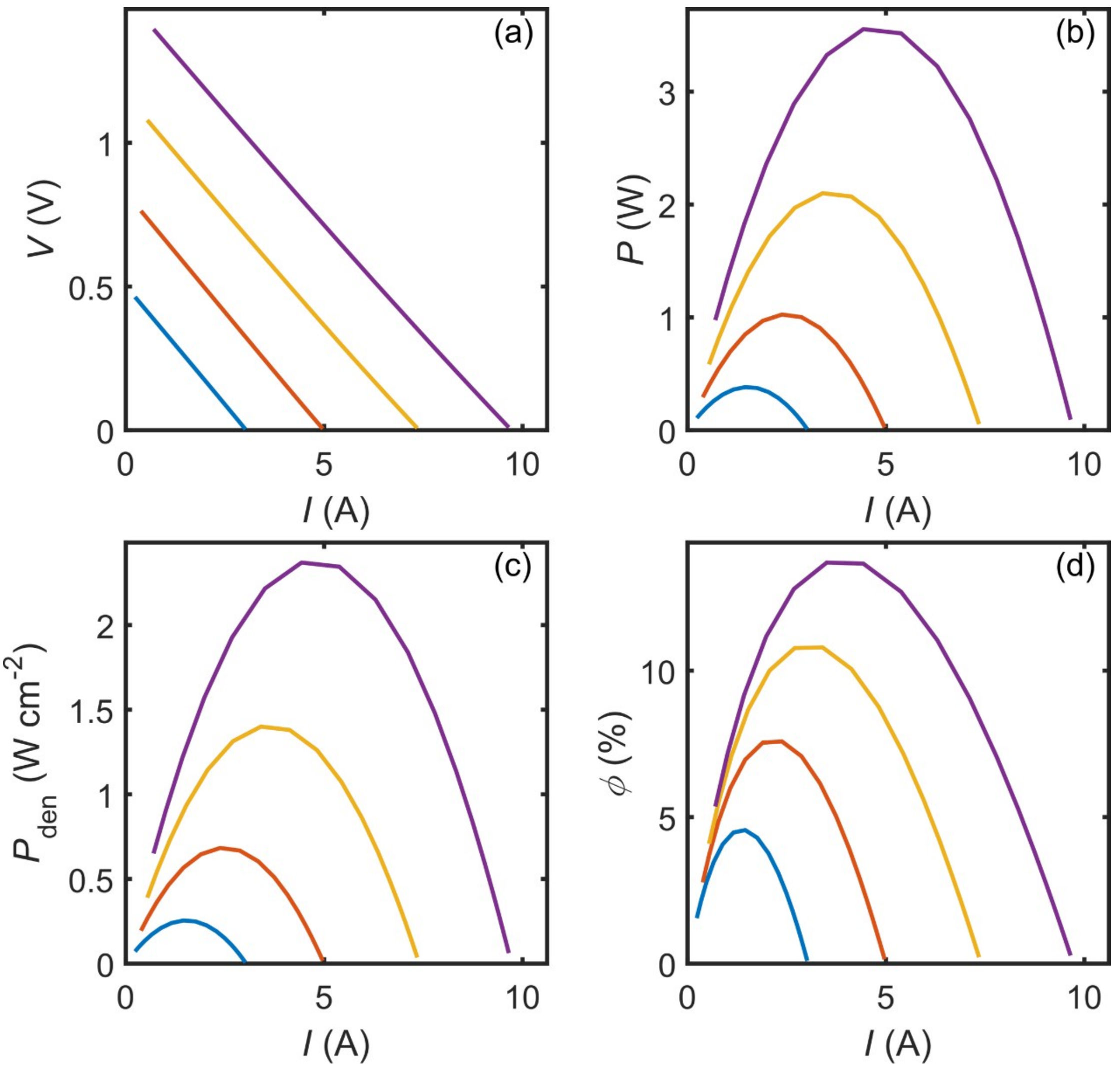

Fig. S18 Device simulation results of as-developed p-type $Ge_{0.89}Cr_{0.03}Sb_{0.08}Te$ and reported n-type $Ba_{0.3}In_{0.3}Co_4Sb_{12}$-$(BaFe_{12}O_{19})_{0.0035}$.[20] Generated (a) voltage (V), (b) output electrical power (P), (c) output electrical power density (P_{den}), and (d) conversion efficiency (ϕ) of the module under cold side temperature of 300 K and hot side temperatures of 480, 580, 680, and 780 K.

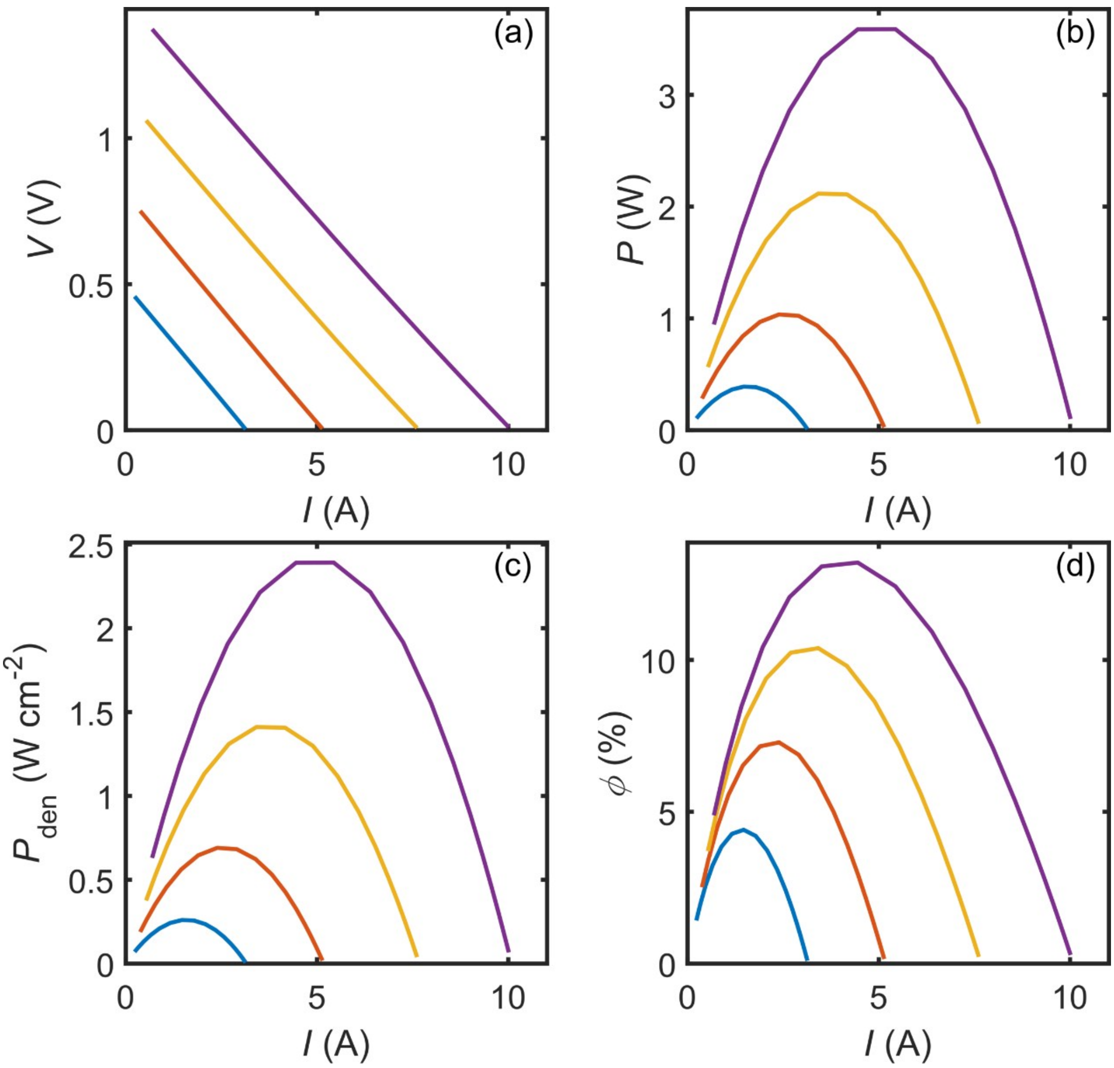

Fig. S19 Device simulation results of as-developed p-type $Ge_{0.89}Cr_{0.03}Sb_{0.08}Te$ and reported n-type $Ba_{0.3}In_{0.3}Co_4Sb_{12}$-$Co_{0.002}$.[21] Generated (a) voltage (*V*), (b) output electrical power (*P*), (c) output electrical power density (P_{den}), and (d) conversion efficiency (ϕ) of the module under cold side temperature of 300 K and hot side temperatures of 480, 580, 680, and 780 K.

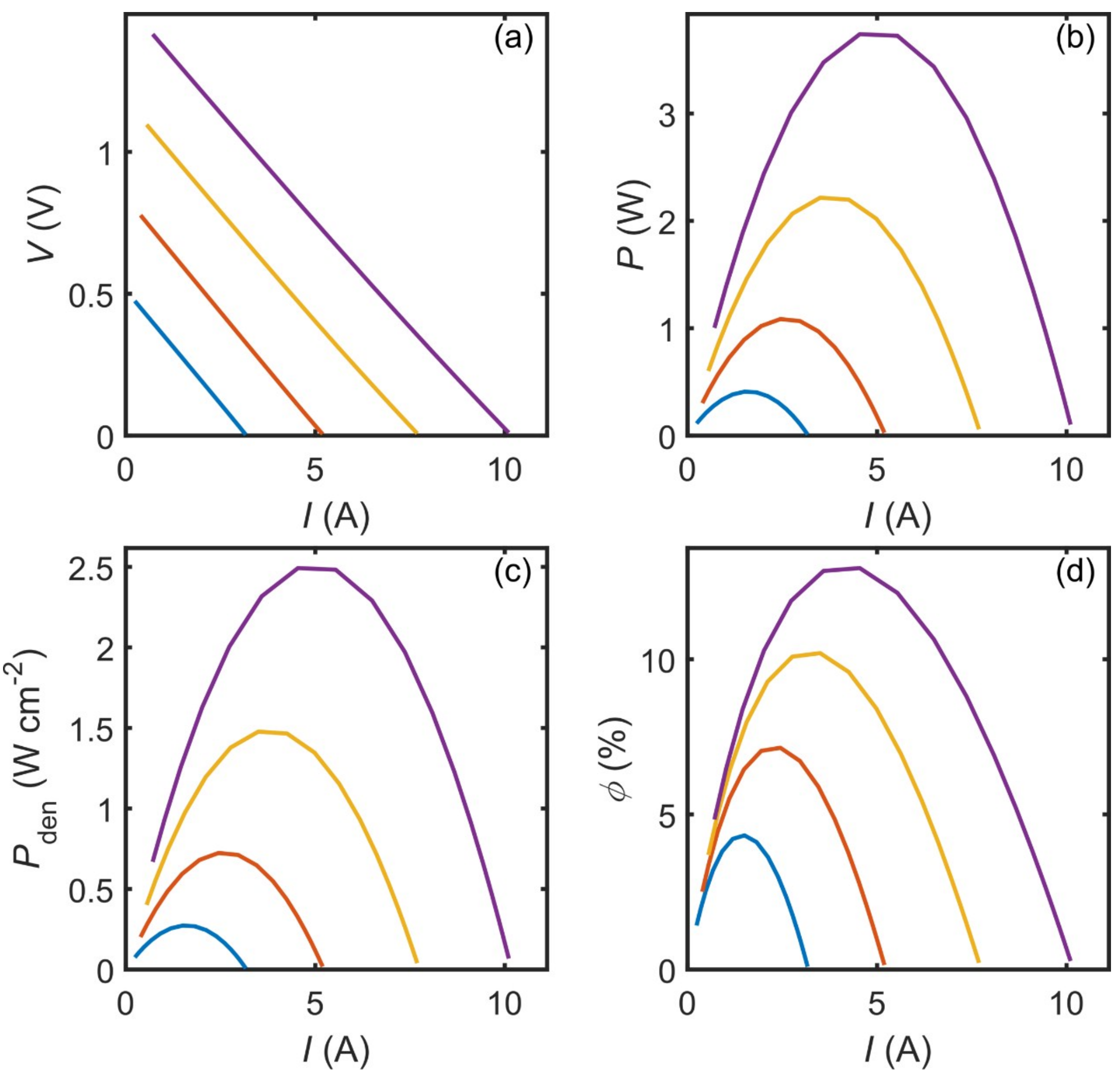

Fig. S20 Device simulation results of as-developed p-type $Ge_{0.89}Cr_{0.03}Sb_{0.08}Te$ and reported n-type $Yb_{0.3}Co_4Sb_{12.2}$.[22] Generated (a) voltage (V), (b) output electrical power (P), (c) output electrical power density (P_{den}), and (d) conversion efficiency (ϕ) of the module under cold side temperature of 300 K and hot side temperatures of 480, 580, 680, and 780 K.

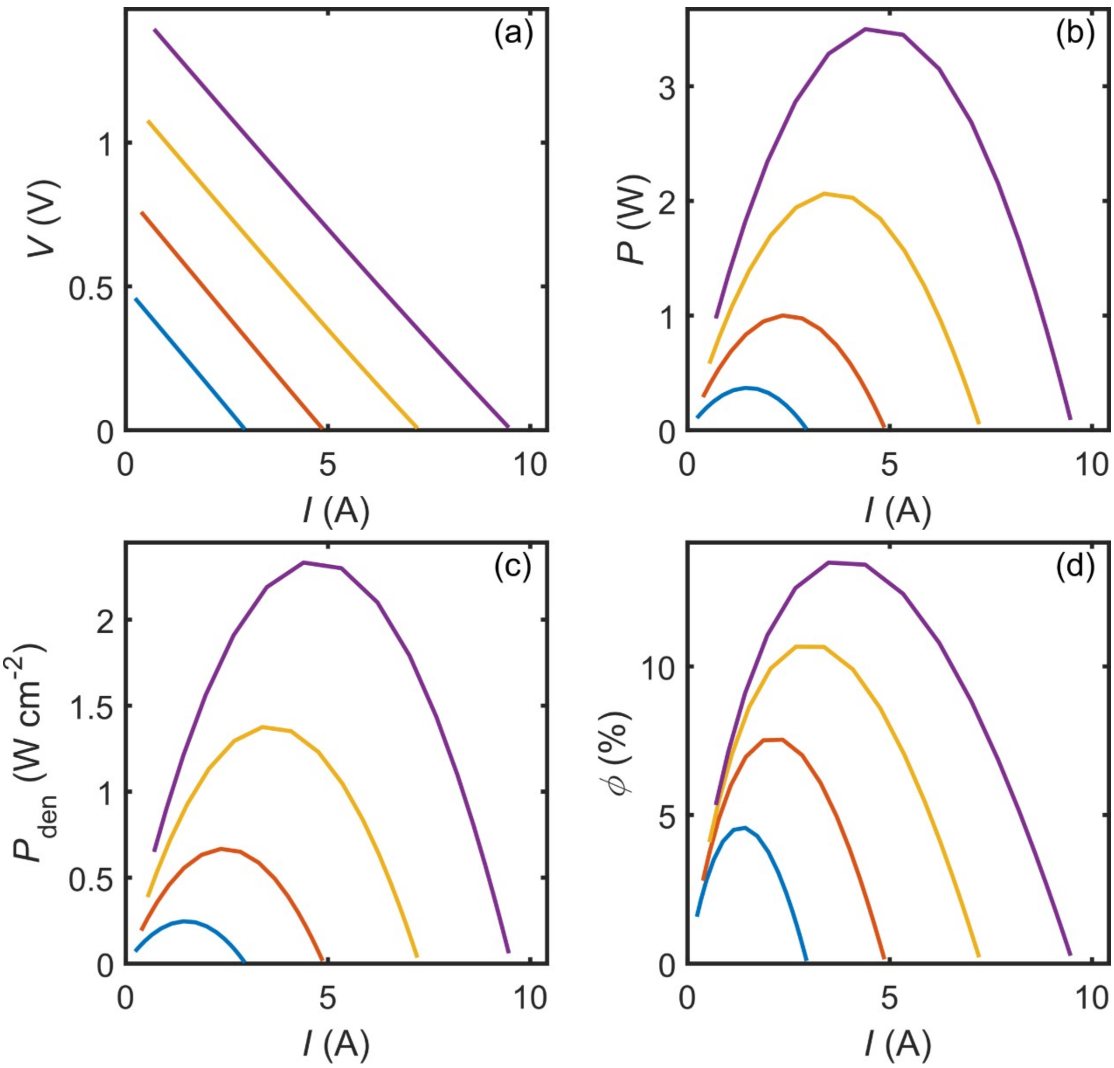

Fig. S21 Device simulation results of as-developed p-type $Ge_{0.89}Cr_{0.03}Sb_{0.08}Te$ and reported n-type $In_{0.2}Ce_{0.15}Co_4Sb_{12}/InSb$.[23] Generated (a) voltage (V), (b) output electrical power (P), (c) output electrical power density (P_{den}), and (d) conversion efficiency (ϕ) of the module under cold side temperature of 300 K and hot side temperatures of 480, 580, 680, and 780 K.

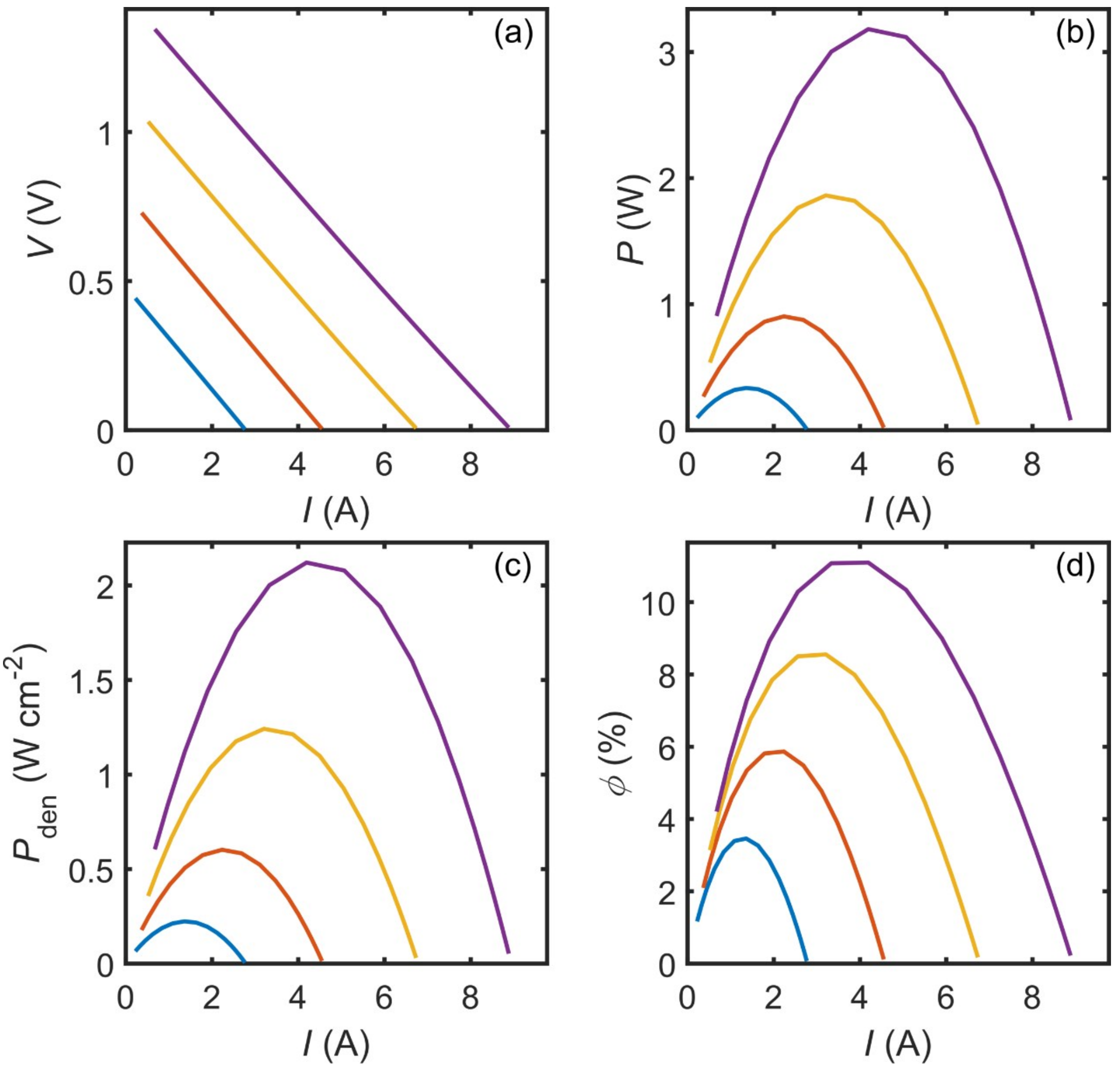

Fig. S22 Device simulation results of as-developed p-type $Ge_{0.89}Cr_{0.03}Sb_{0.08}Te$ and reported n-type $Co_4Sb_{11.3}Te_{0.58}Se_{0.12}$.[24] Generated (a) voltage (V), (b) output electrical power (P), (c) output electrical power density (P_{den}), and (d) conversion efficiency (ϕ) of the module under cold side temperature of 300 K and hot side temperatures of 480, 580, 680, and 780 K.

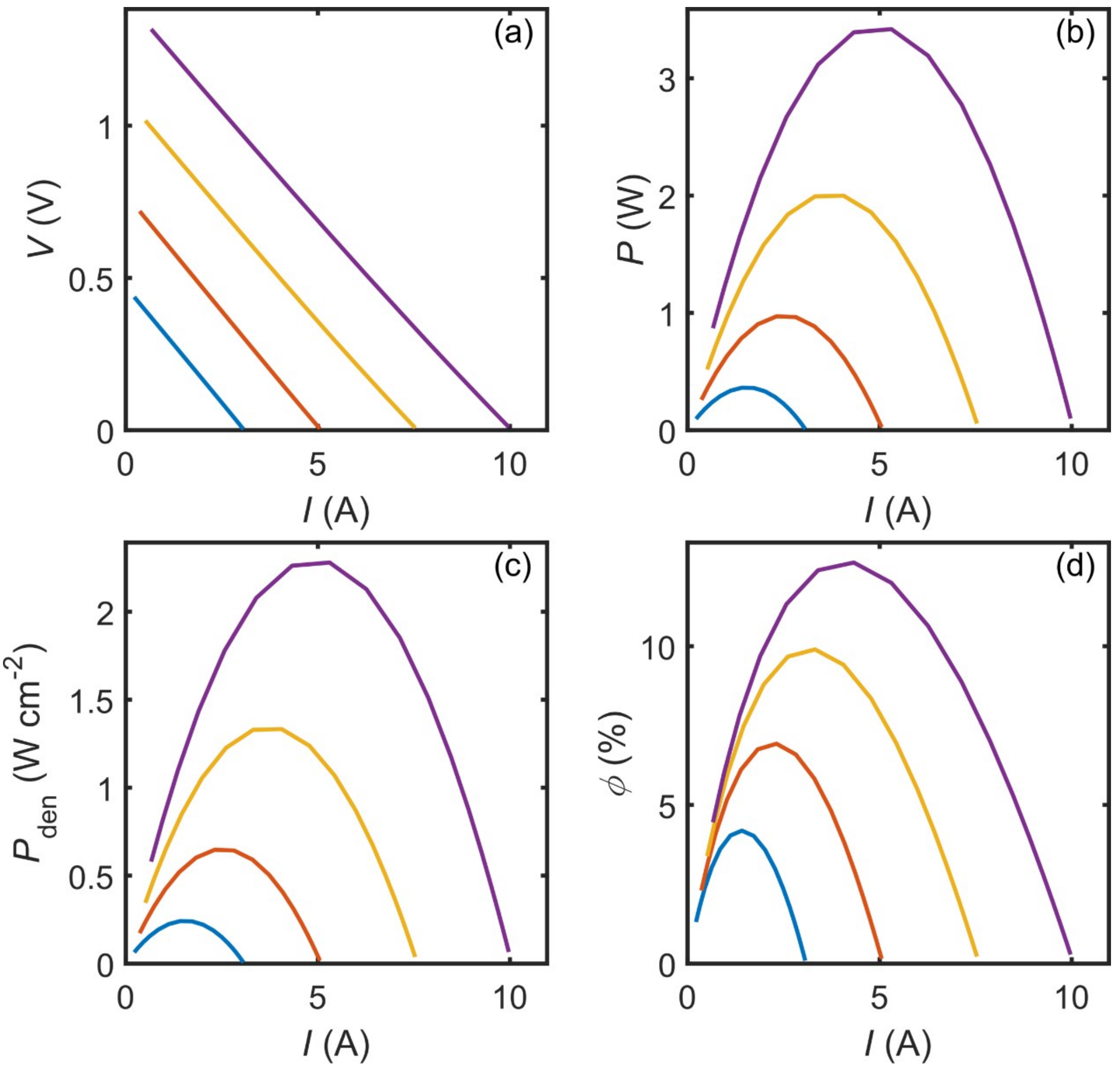

Fig. S23 Device simulation results of as-developed p-type $Ge_{0.89}Cr_{0.03}Sb_{0.08}Te$ and reported n-type $Ba_{0.08}La_{0.05}Yb_{0.04}Co_4Sb_{12}$.[25] Generated (a) voltage (V), (b) output electrical power (P), (c) output electrical power density (P_{den}), and (d) conversion efficiency (ϕ) of the module under cold side temperature of 300 K and hot side temperatures of 480, 580, 680, and 780 K.

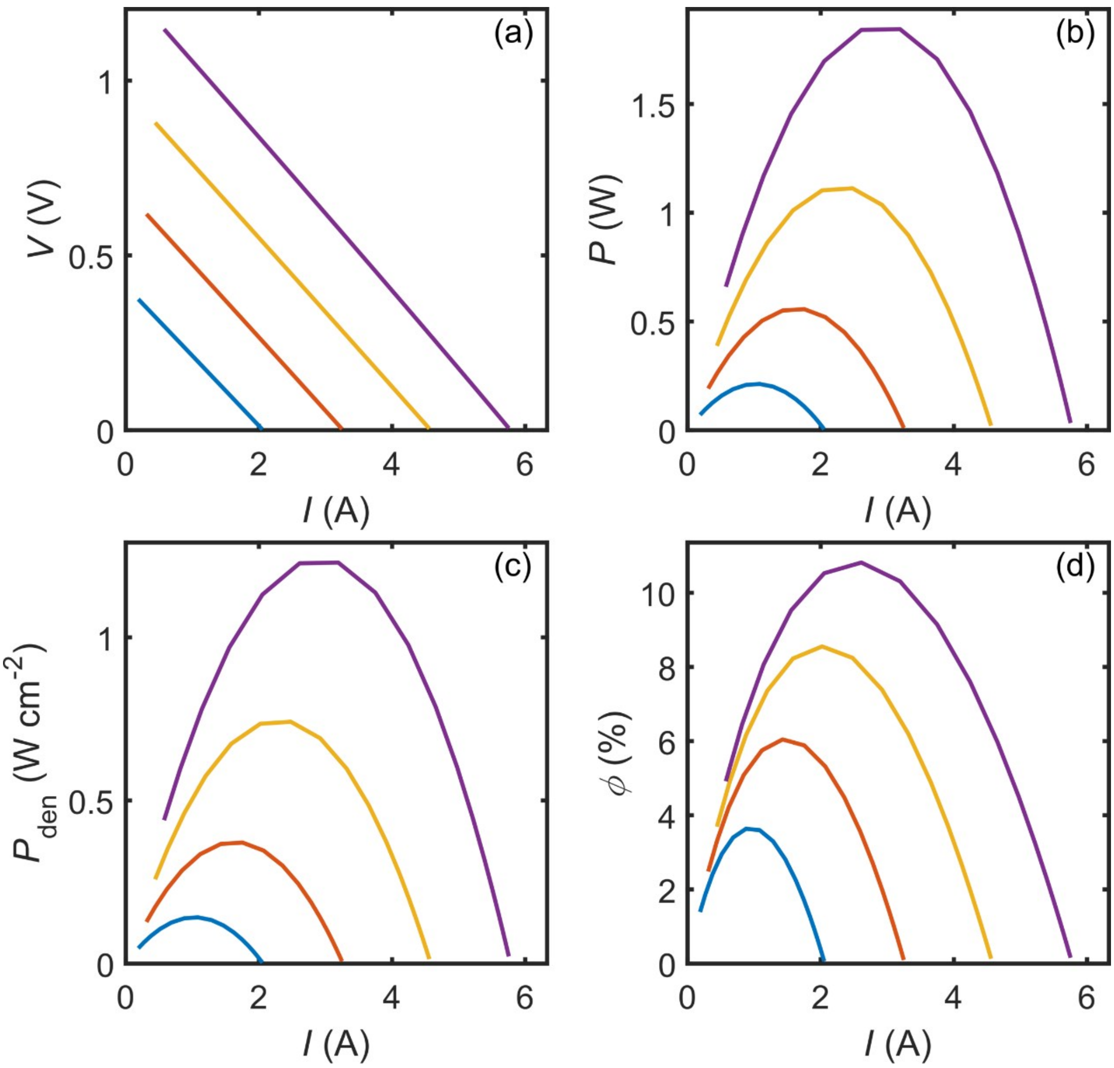

Fig. S24 Device simulation results of as-developed p-type $Ge_{0.89}Cr_{0.03}Sb_{0.08}Te$ and reported n-type $Ba_8Ga_{16-x}Ge_{30+x}$.[26] Generated (a) voltage (*V*), (b) output electrical power (*P*), (c) output electrical power density (P_{den}), and (d) conversion efficiency (ϕ) of the module under cold side temperature of 300 K and hot side temperatures of 480, 580, 680, and 780 K.

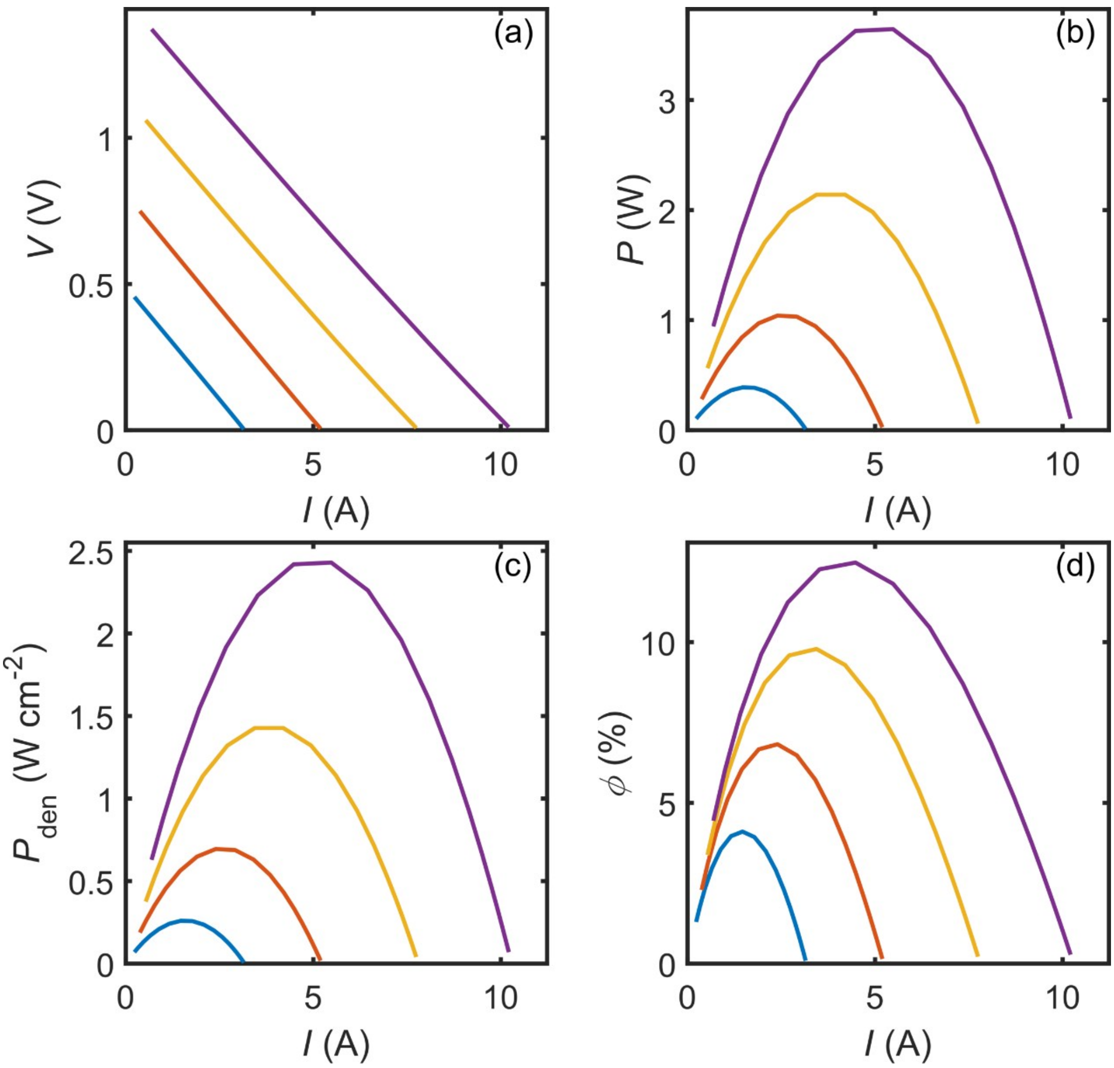

Fig. S25 Device simulation results of as-developed p-type $Ge_{0.89}Cr_{0.03}Sb_{0.08}Te$ and reported n-type $YbxCo_4Sb_{12}$.[27] Generated (a) voltage (V), (b) output electrical power (P), (c) output electrical power density (P_{den}), and (d) conversion efficiency (ϕ) of the module under cold side temperature of 300 K and hot side temperatures of 480, 580, 680, and 780 K.

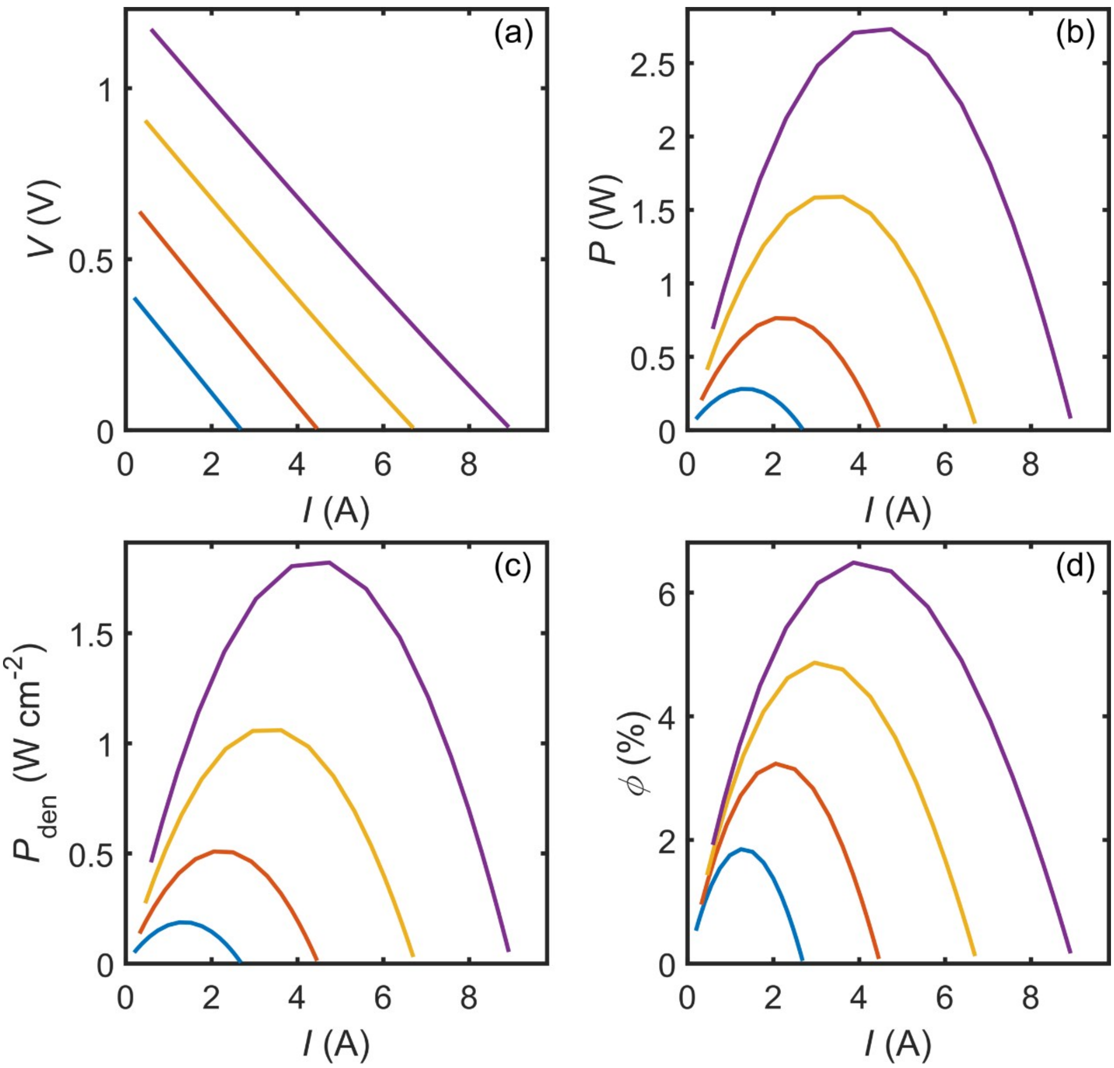

Fig. S26 Device simulation results of as-developed p-type $Ge_{0.89}Cr_{0.03}Sb_{0.08}Te$ and reported n-type $Ti_{0.95}Mn_{0.05}NiSn_{0.95}Sb_{0.05}$.[28] Generated (a) voltage (V), (b) output electrical power (P), (c) output electrical power density (P_{den}), and (d) conversion efficiency (ϕ) of the module under cold side temperature of 300 K and hot side temperatures of 480, 580, 680, and 780 K.

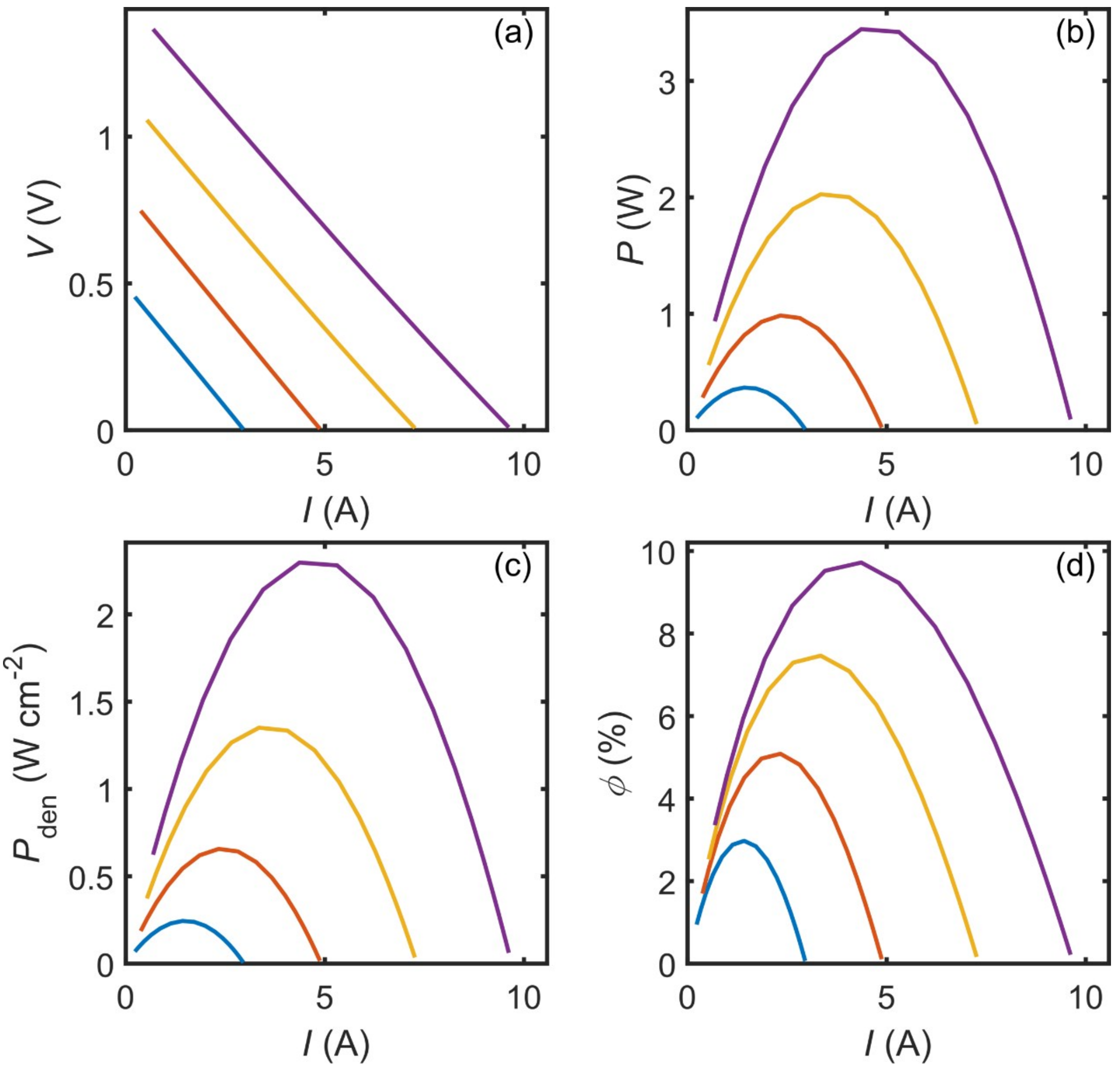

Fig. S27 Device simulation results of as-developed p-type $Ge_{0.89}Cr_{0.03}Sb_{0.08}Te$ and reported n-type Hf_xZr_{1-x} $NiSn_{0.99}Sb_{0.01}$.[29] Generated (a) voltage (V), (b) output electrical power (P), (c) output electrical power density (P_{den}), and (d) conversion efficiency (ϕ) of the module under cold side temperature of 300 K and hot side temperatures of 480, 580, 680, and 780 K.

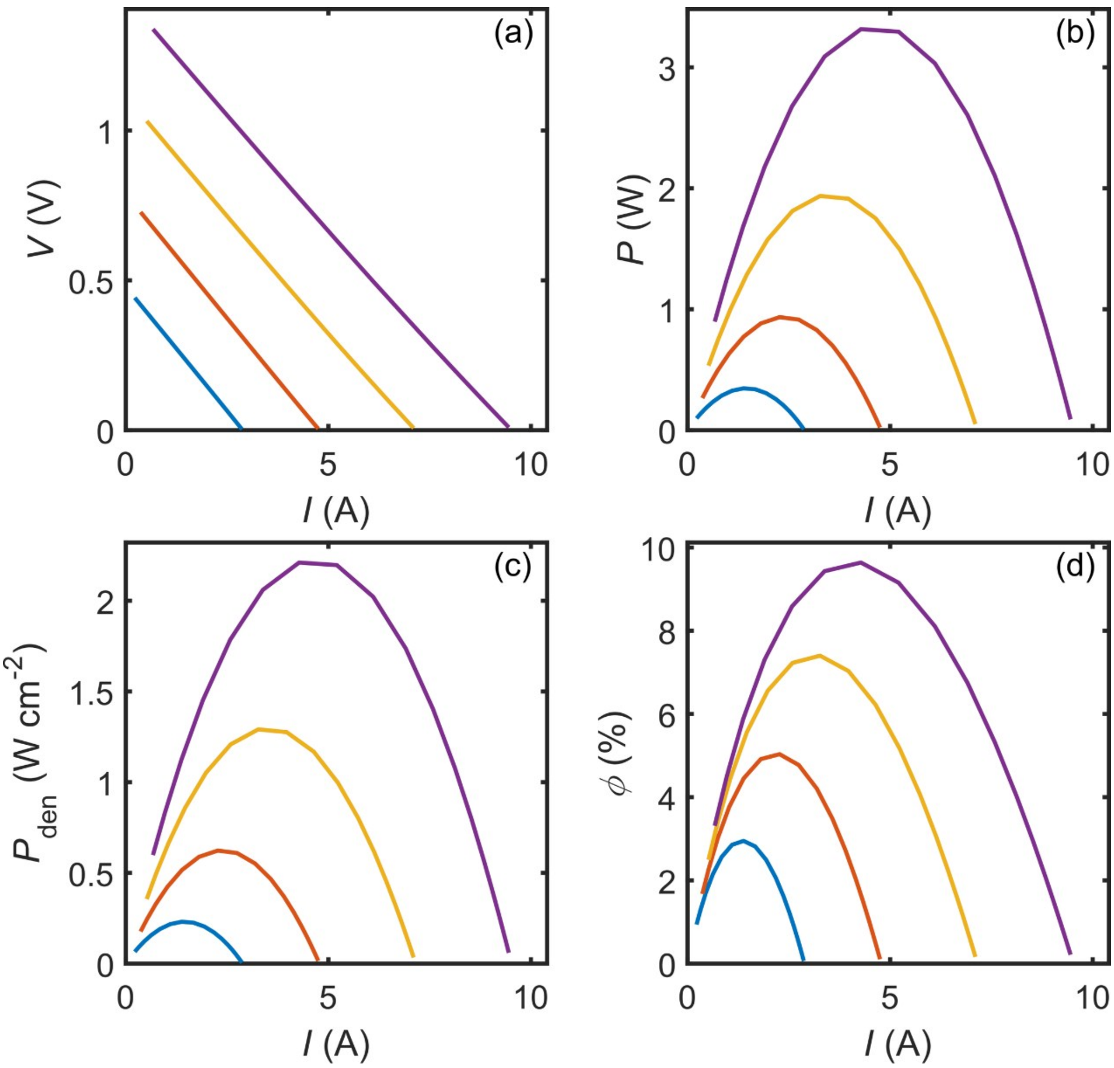

Fig. S28 Device simulation results of as-developed p-type $Ge_{0.89}Cr_{0.03}Sb_{0.08}Te$ and reported n-type $Hf_{0.75}Zr_{0.25}NiSn_{0.99}Sb_{0.01}$.[30] Generated (a) voltage (V), (b) output electrical power (P), (c) output electrical power density (P_{den}), and (d) conversion efficiency (ϕ) of the module under cold side temperature of 300 K and hot side temperatures of 480, 580, 680, and 780 K.

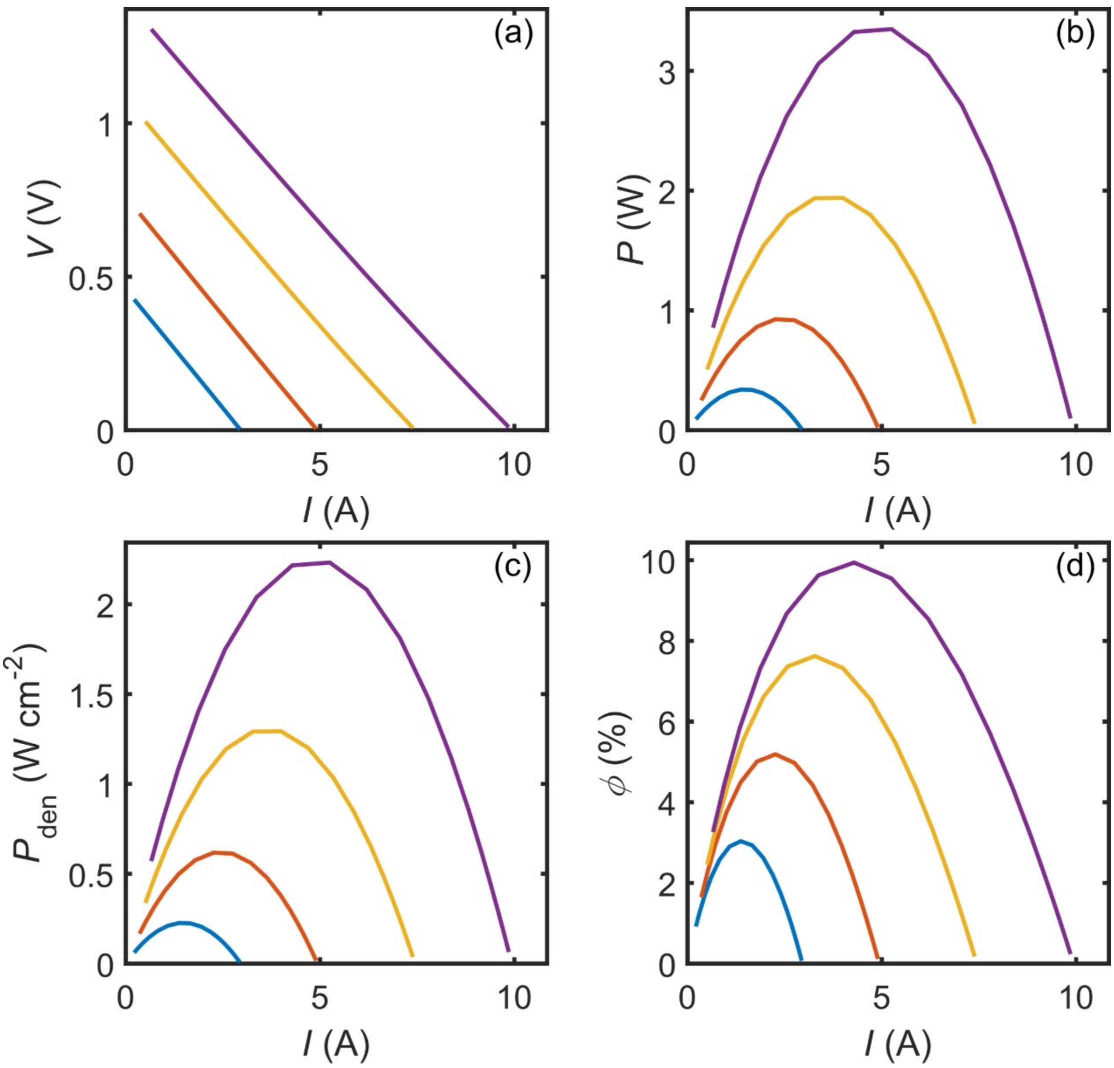

Fig. S29 Device simulation results of as-developed p-type $Ge_{0.89}Cr_{0.03}Sb_{0.08}Te$ and reported n-type $Zr_{0.5}Hf_{0.5}NiSn_{0.985}Sb_{0.015}$.[31] Generated (a) voltage (V), (b) output electrical power (P), (c) output electrical power density (P_{den}), and (d) conversion efficiency (ϕ) of the module under cold side temperature of 300 K and hot side temperatures of 480, 580, 680, and 780 K.

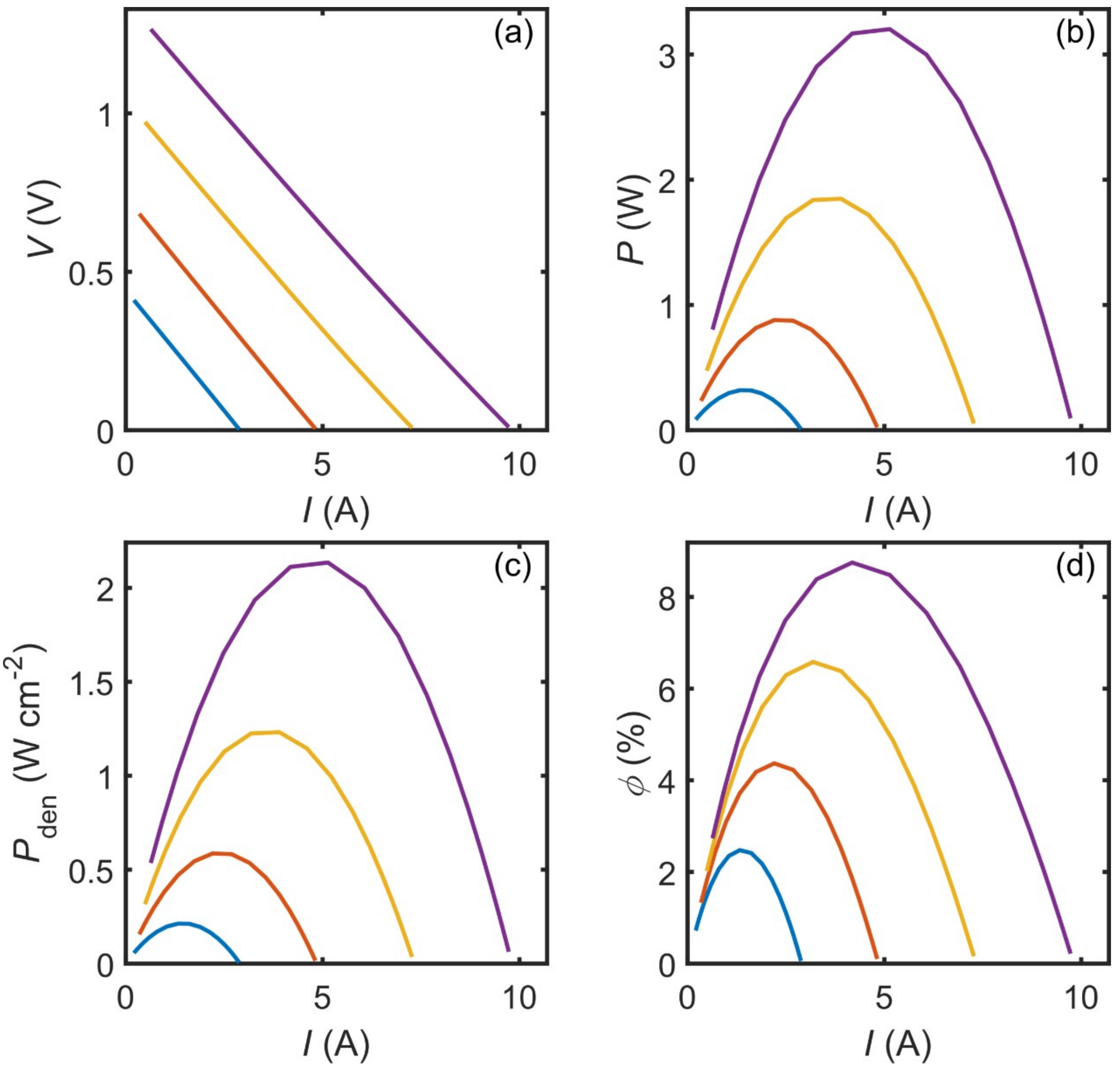

Fig. S30 Device simulation results of as-developed p-type $Ge_{0.89}Cr_{0.03}Sb_{0.08}Te$ and reported n-type $Zr_{0.2}Hf_{0.8}NiSn_{0.985}Sb_{0.015}$.[32] Generated (a) voltage (V), (b) output electrical power (P), (c) output electrical power density (P_{den}), and (d) conversion efficiency (ϕ) of the module under cold side temperature of 300 K and hot side temperatures of 480, 580, 680, and 780 K.

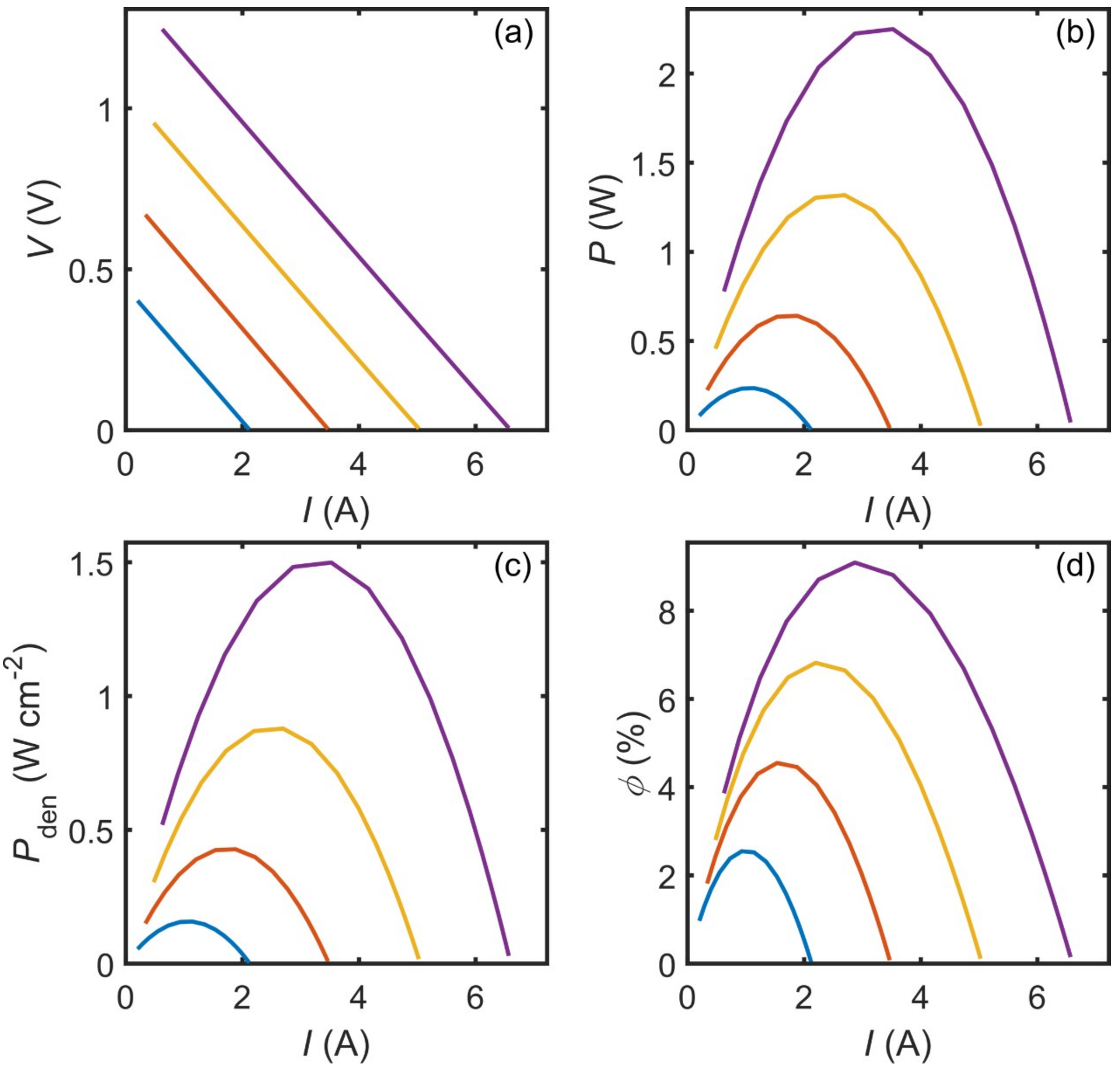

Fig. S31 Device simulation results of as-developed p-type $Ge_{0.89}Cr_{0.03}Sb_{0.08}Te$ and reported n-type $Nb_{0.8}Co_{0.92}Ni_{0.08}Sb$.[33] Generated (a) voltage (V), (b) output electrical power (P), (c) output electrical power density (P_{den}), and (d) conversion efficiency (ϕ) of the module under cold side temperature of 300 K and hot side temperatures of 480, 580, 680, and 780 K.

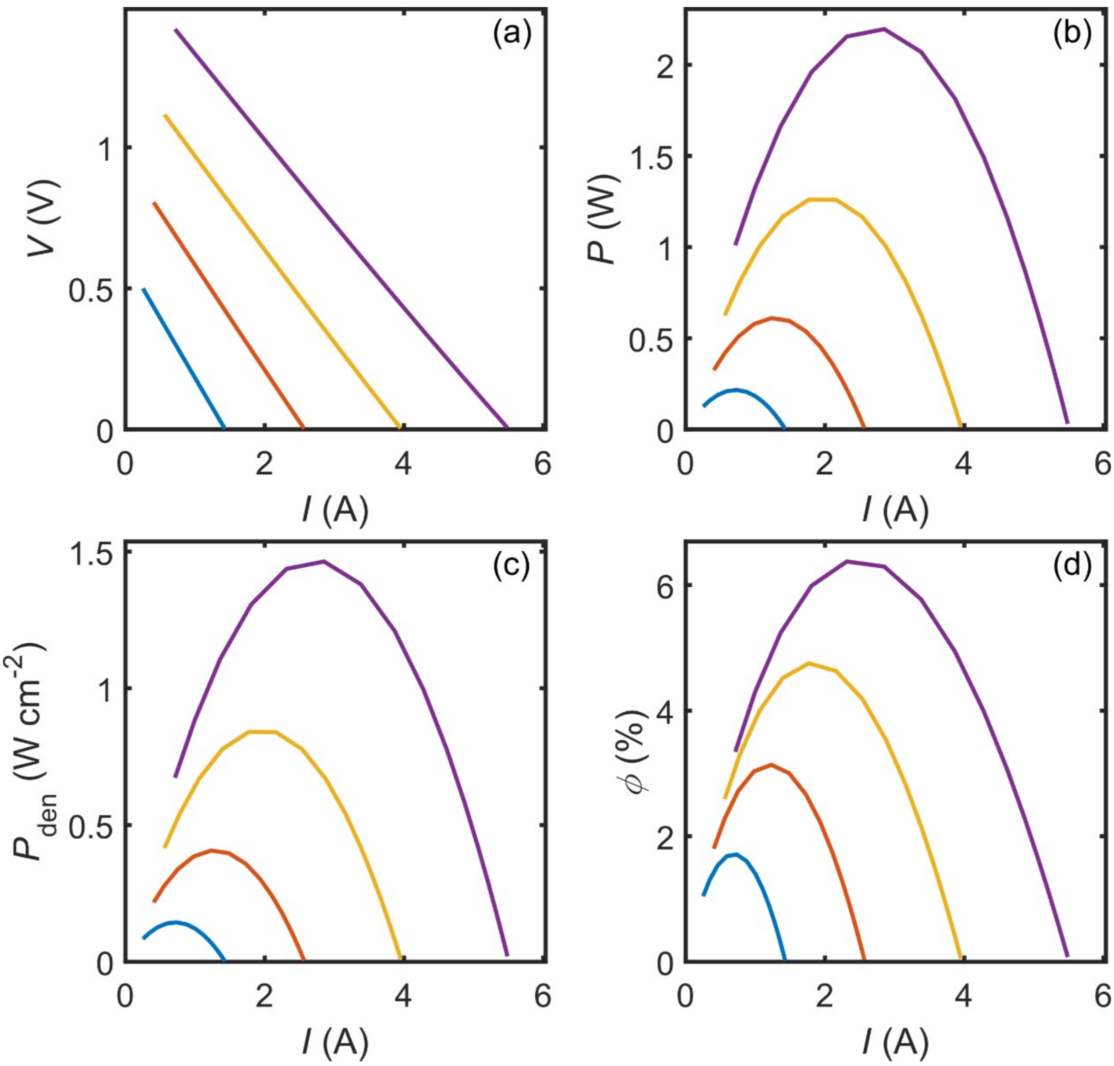

Fig. S32 Device simulation results of as-developed p-type $Ge_{0.89}Cr_{0.03}Sb_{0.08}Te$ and reported n-type ZrNiSn.[34] Generated (a) voltage (V), (b) output electrical power (P), (c) output electrical power density (P_{den}), and (d) conversion efficiency (ϕ) of the module under cold side temperature of 300 K and hot side temperatures of 480, 580, 680, and 780 K.

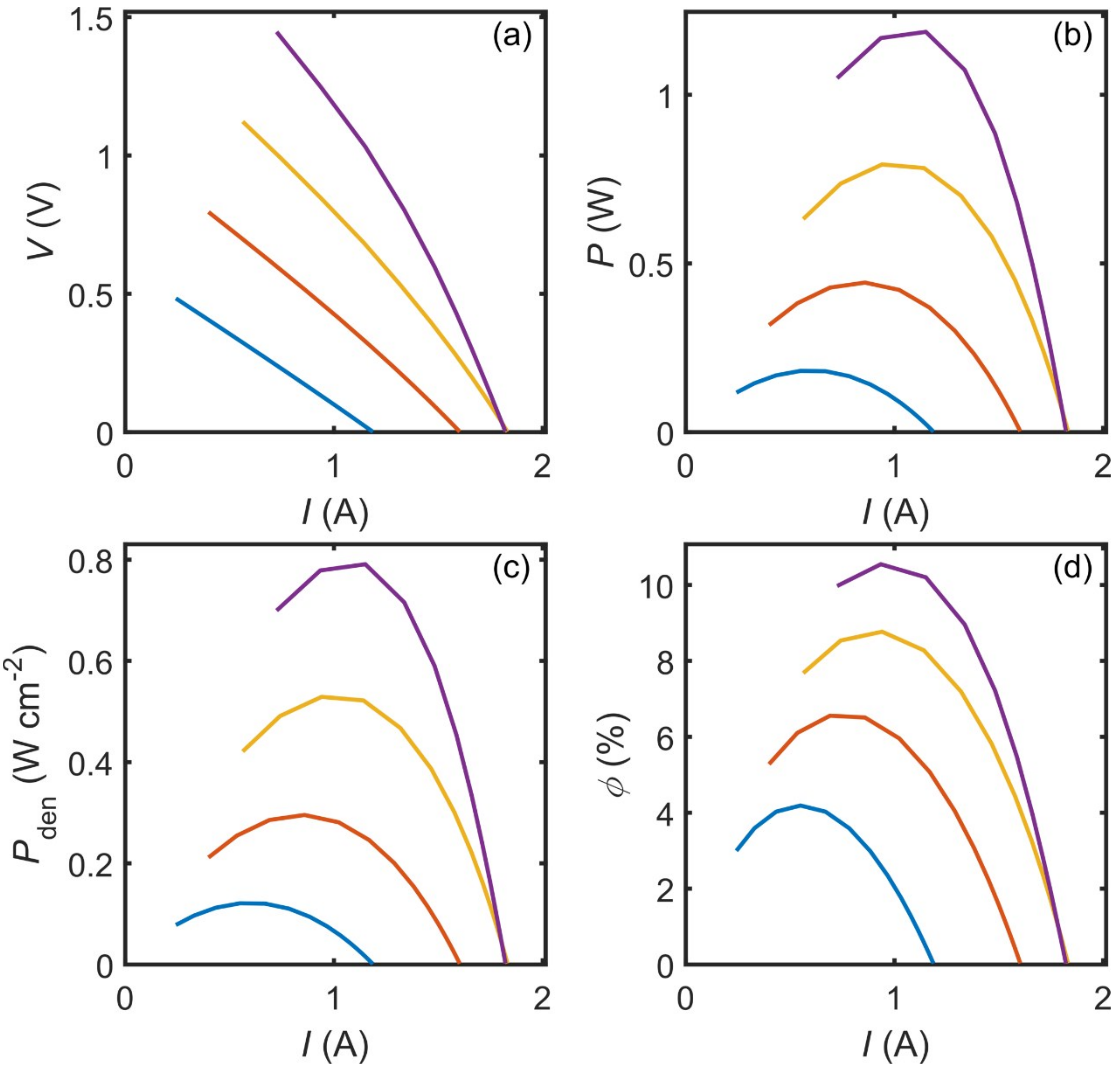

Fig. S33 Device simulation results of as-developed p-type $Ge_{0.89}Cr_{0.03}Sb_{0.08}Te$ and reported n-type Br-doepd SnSe.[35] Generated (a) voltage (V), (b) output electrical power (P), (c) output electrical power density (P_{den}), and (d) conversion efficiency (ϕ) of the module under cold side temperature of 300 K and hot side temperatures of 480, 580, 680, and 780 K.

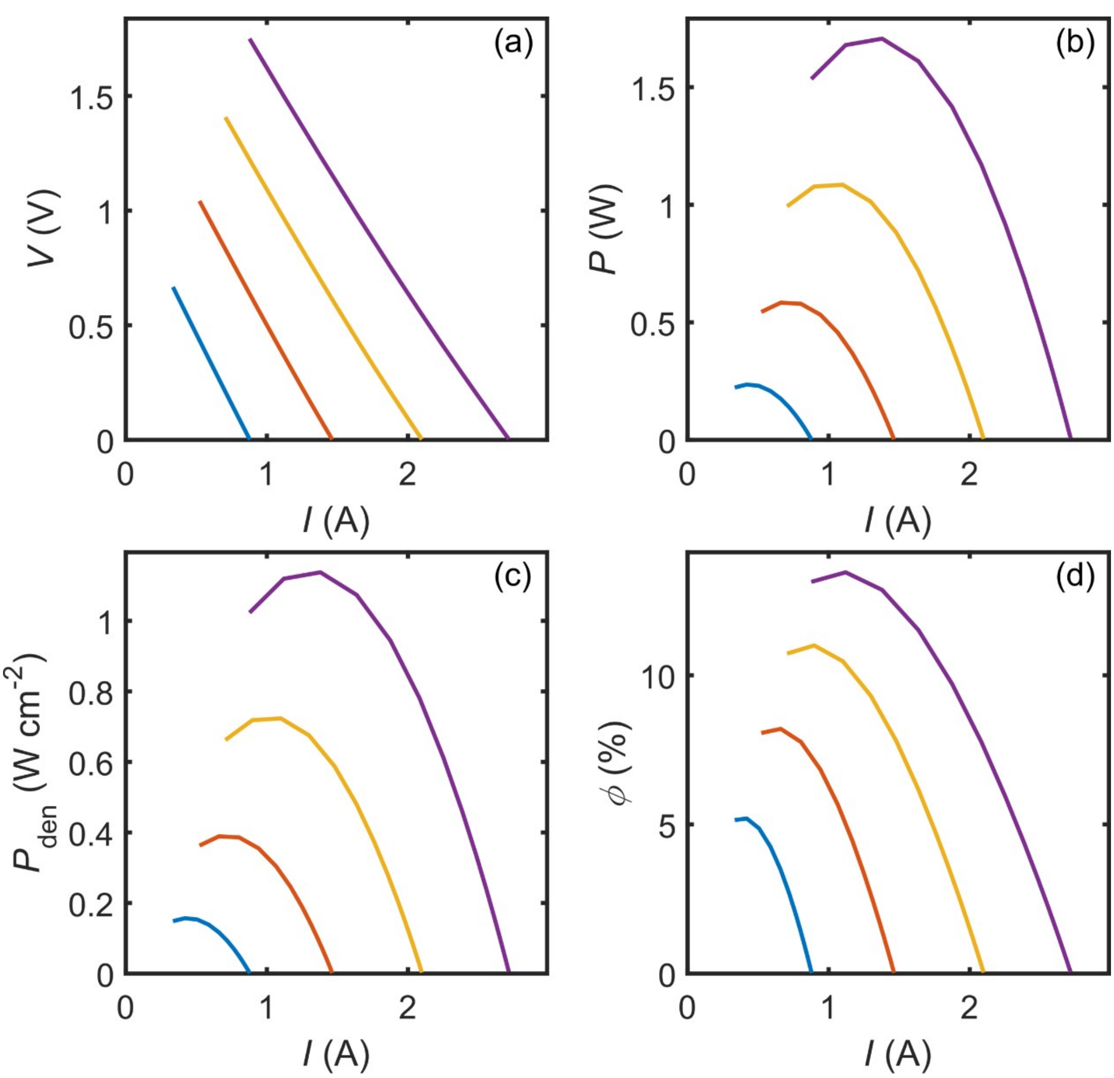

Fig. S34 Device simulation results of as-developed p-type $Ge_{0.89}Cr_{0.03}Sb_{0.08}Te$ and reported n-type Bi-doped SnSe.[36] Generated (a) voltage (V), (b) output electrical power (P), (c) output electrical power density (P_{den}), and (d) conversion efficiency (ϕ) of the module under cold side temperature of 300 K and hot side temperatures of 480, 580, 680, and 780 K.

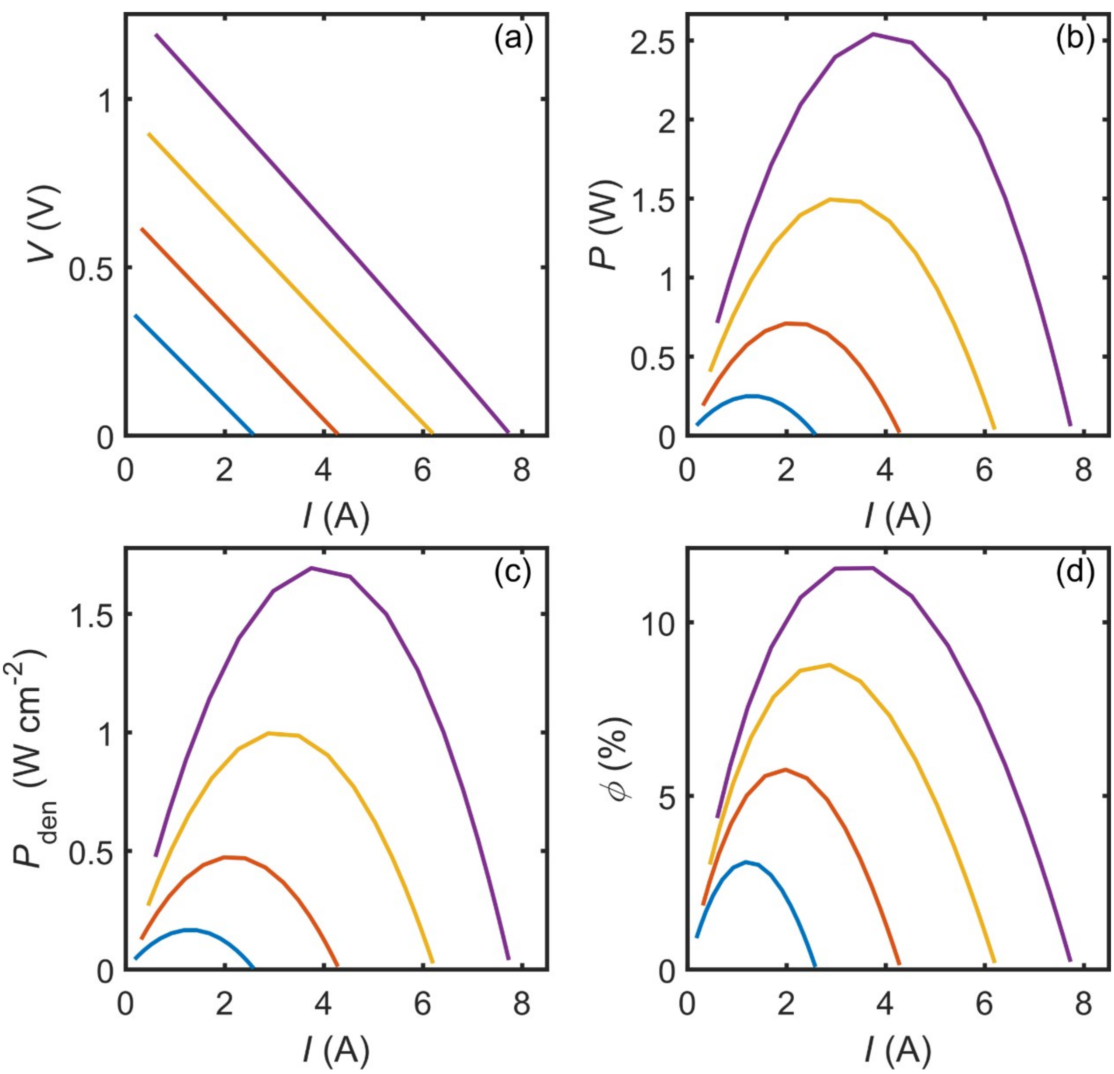

Fig. S35 Device simulation results of as-developed p-type $Ge_{0.89}Cr_{0.03}Sb_{0.08}Te$ and reported n-type $Pb_{1.002}Se_{0.9982}Br_{0.0018}$.[37] Generated (a) voltage (V), (b) output electrical power (P), (c) output electrical power density (P_{den}), and (d) conversion efficiency (ϕ) of the module under cold side temperature of 300 K and hot side temperatures of 480, 580, 680, and 780 K.

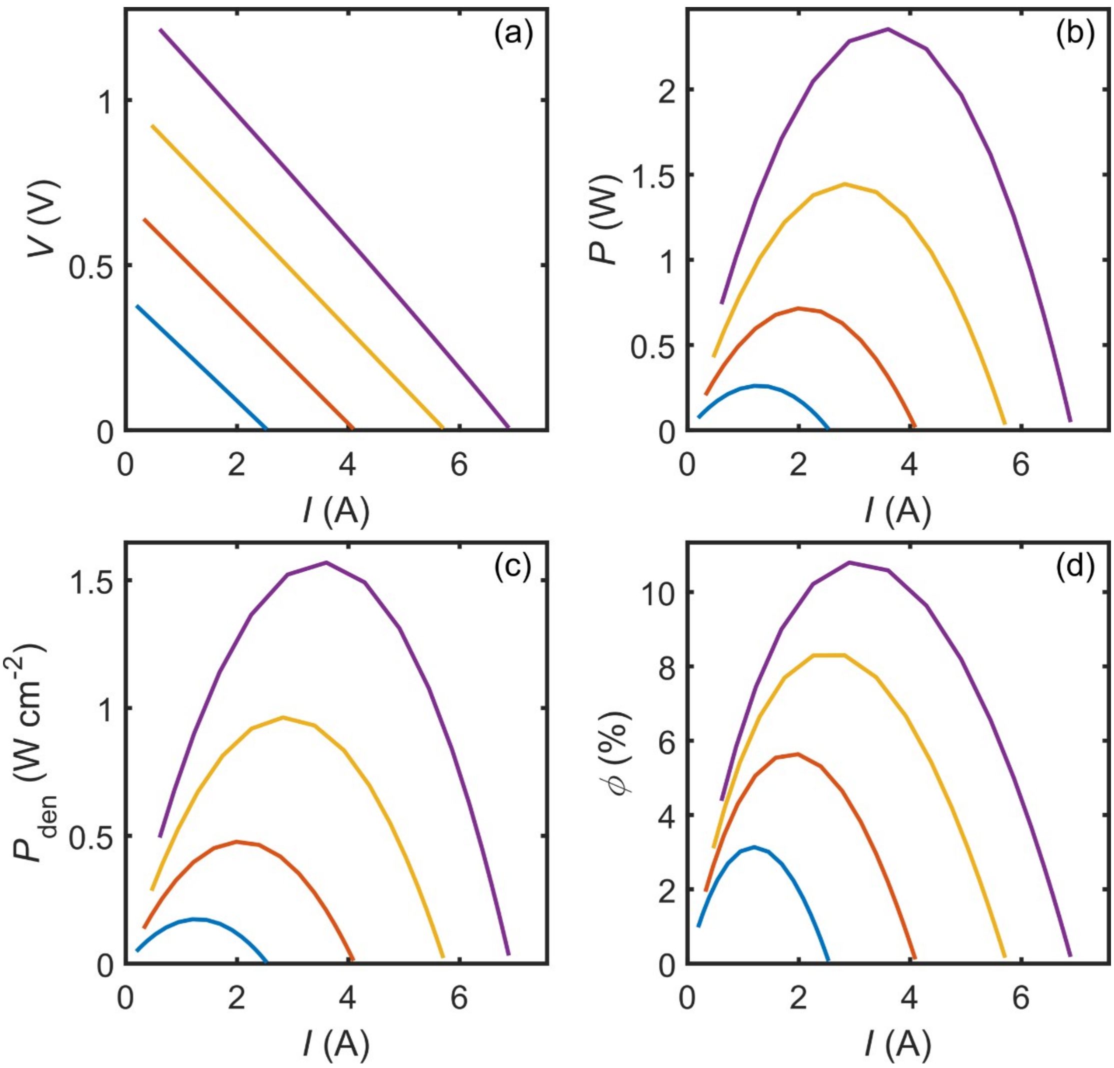

Fig. S36 Device simulation results of as-developed p-type $Ge_{0.89}Cr_{0.03}Sb_{0.08}Te$ and reported n-type $PbS_{0.9978}Cl_{0.0022}$.[38] Generated (a) voltage (V), (b) output electrical power (P), (c) output electrical power density (P_{den}), and (d) conversion efficiency (ϕ) of the module under cold side temperature of 300 K and hot side temperatures of 480, 580, 680, and 780 K.

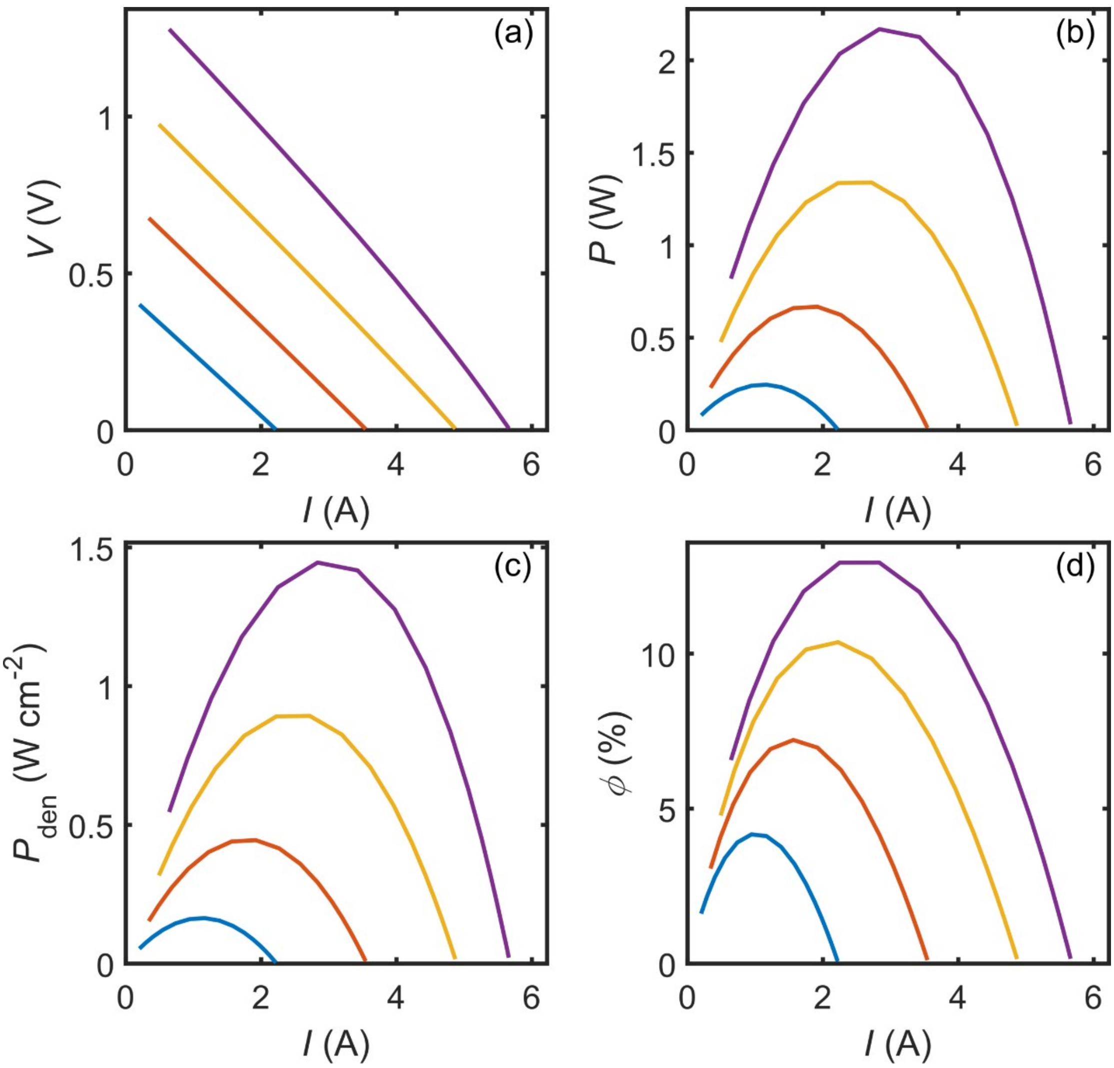

Fig. S37 Device simulation results of as-developed p-type $Ge_{0.89}Cr_{0.03}Sb_{0.08}Te$ and reported n-type $Pb_{0.95}SeSb_{0.033}$.[39] Generated (a) voltage (V), (b) output electrical power (P), (c) output electrical power density (P_{den}), and (d) conversion efficiency (ϕ) of the module under cold side temperature of 300 K and hot side temperatures of 480, 580, 680, and 780 K.

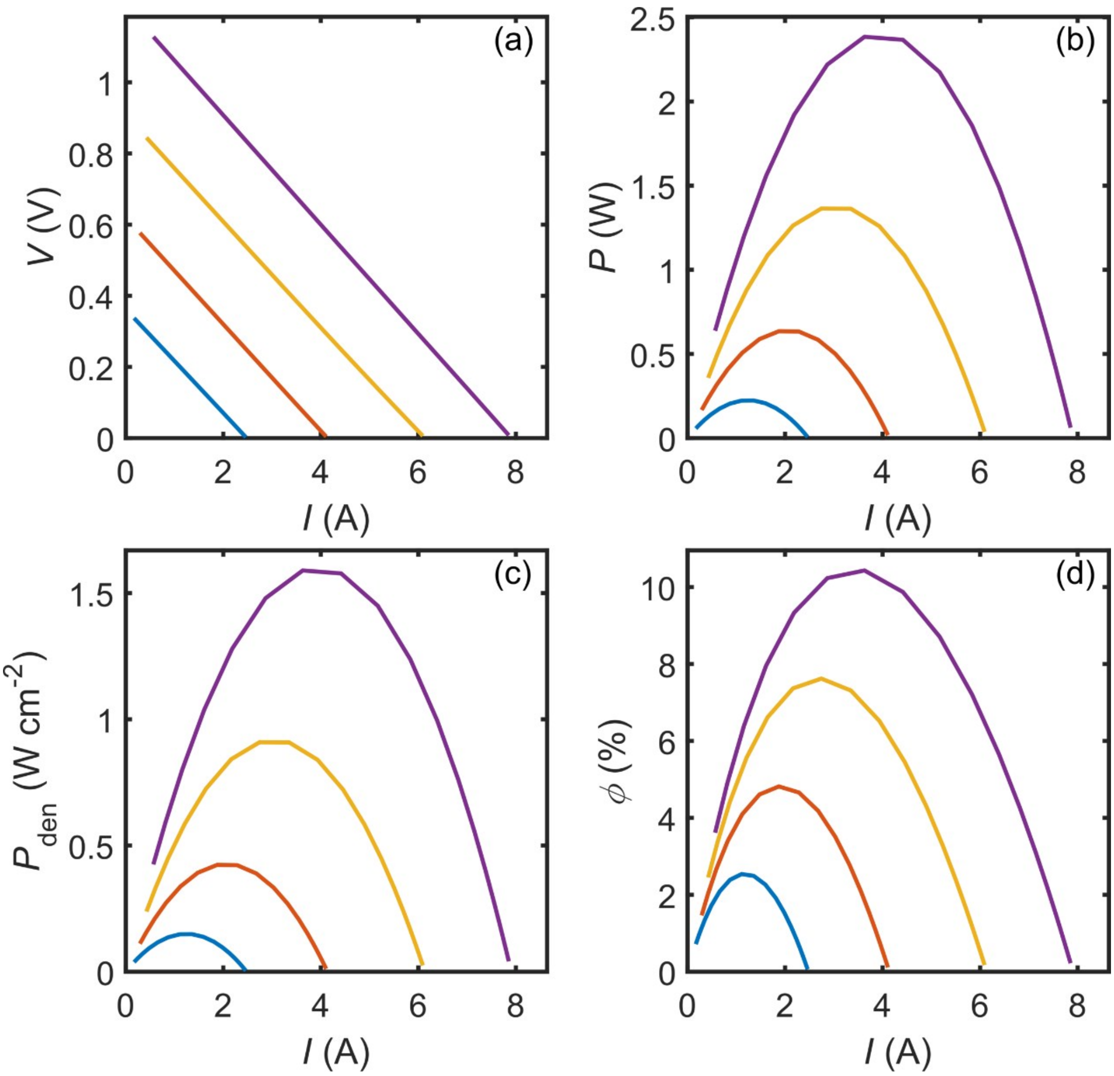

Fig. S38 Device simulation results of as-developed p-type $Ge_{0.89}Cr_{0.03}Sb_{0.08}Te$ and reported n-type $PbIn_{0.005}Se$.[40] Generated (a) voltage (V), (b) output electrical power (P), (c) output electrical power density (P_{den}), and (d) conversion efficiency (ϕ) of the module under cold side temperature of 300 K and hot side temperatures of 480, 580, 680, and 780 K.

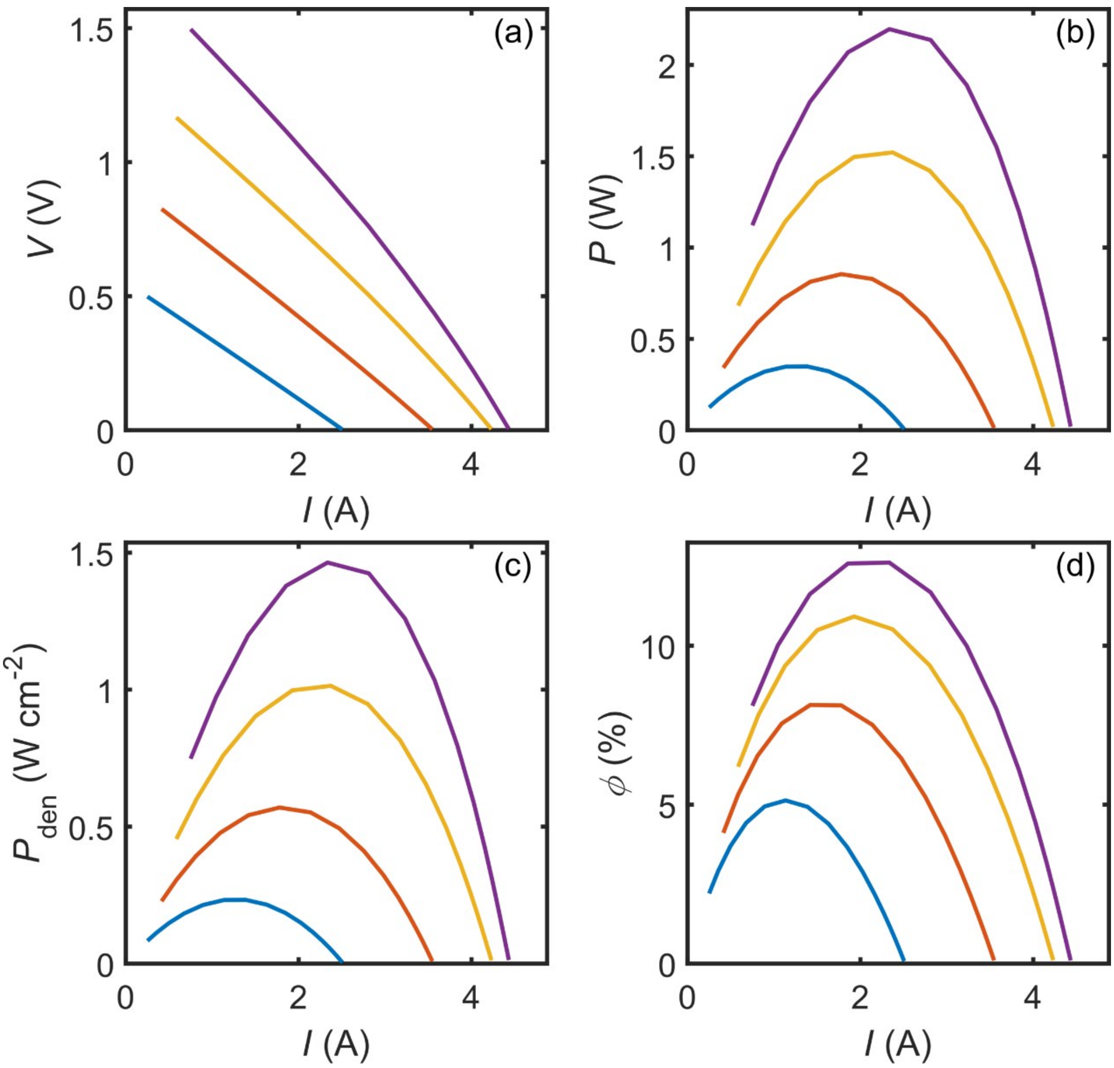

Fig. S39 Device simulation results of as-developed p-type $Ge_{0.89}Cr_{0.03}Sb_{0.08}Te$ and reported n-type $Pb_{0.9925}Cr_{0.0075}Se$.[41] Generated (a) voltage (V), (b) output electrical power (P), (c) output electrical power density (P_{den}), and (d) conversion efficiency (ϕ) of the module under cold side temperature of 300 K and hot side temperatures of 480, 580, 680, and 780 K.

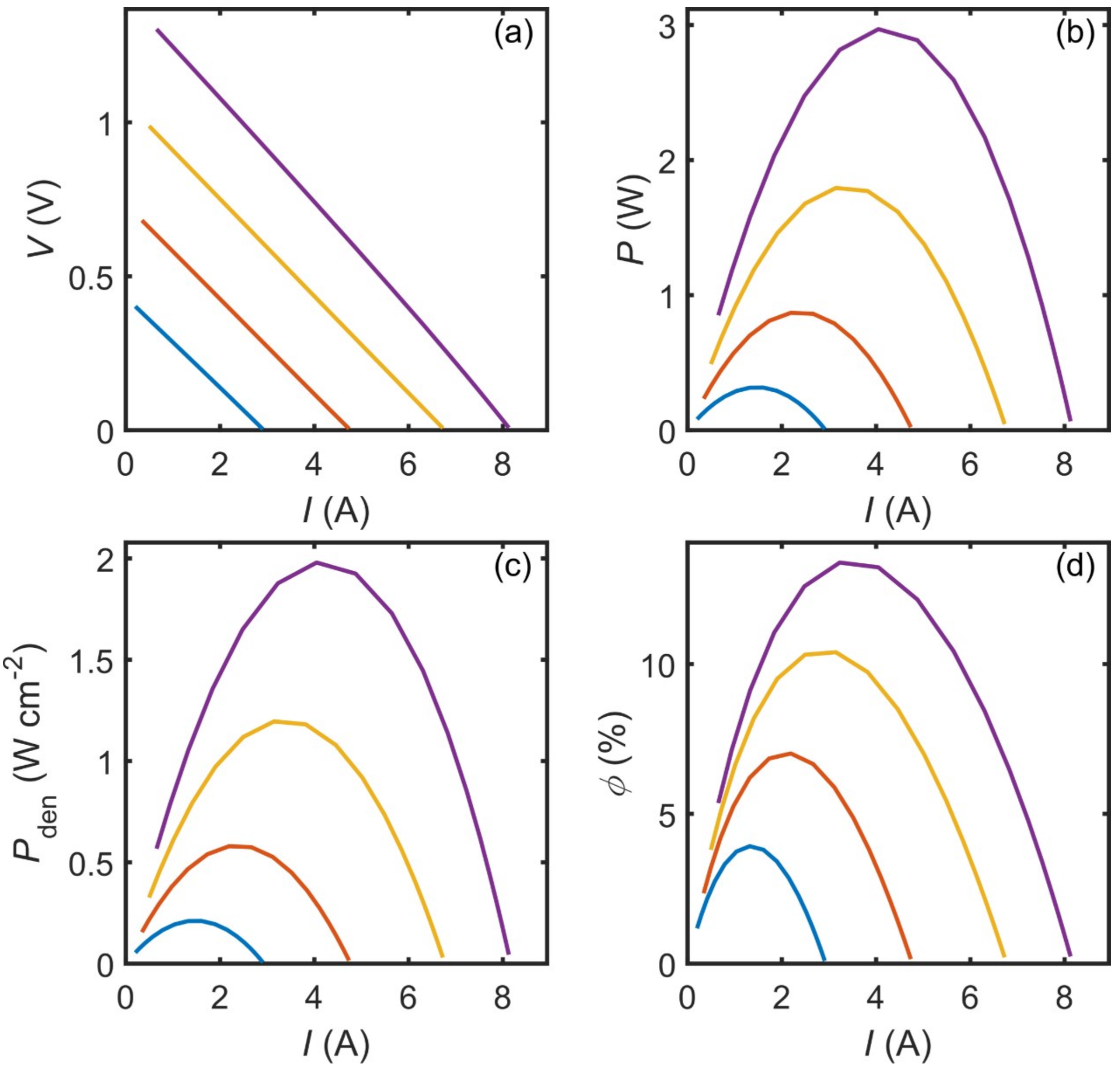

Fig. S40 Device simulation results of as-developed p-type $Ge_{0.89}Cr_{0.03}Sb_{0.08}Te$ and reported n-type $PbTe_{0.9988}I_{0.0012}$.[42] Generated (a) voltage (V), (b) output electrical power (P), (c) output electrical power density (P_{den}), and (d) conversion efficiency (ϕ) of the module under cold side temperature of 300 K and hot side temperatures of 480, 580, 680, and 780 K.

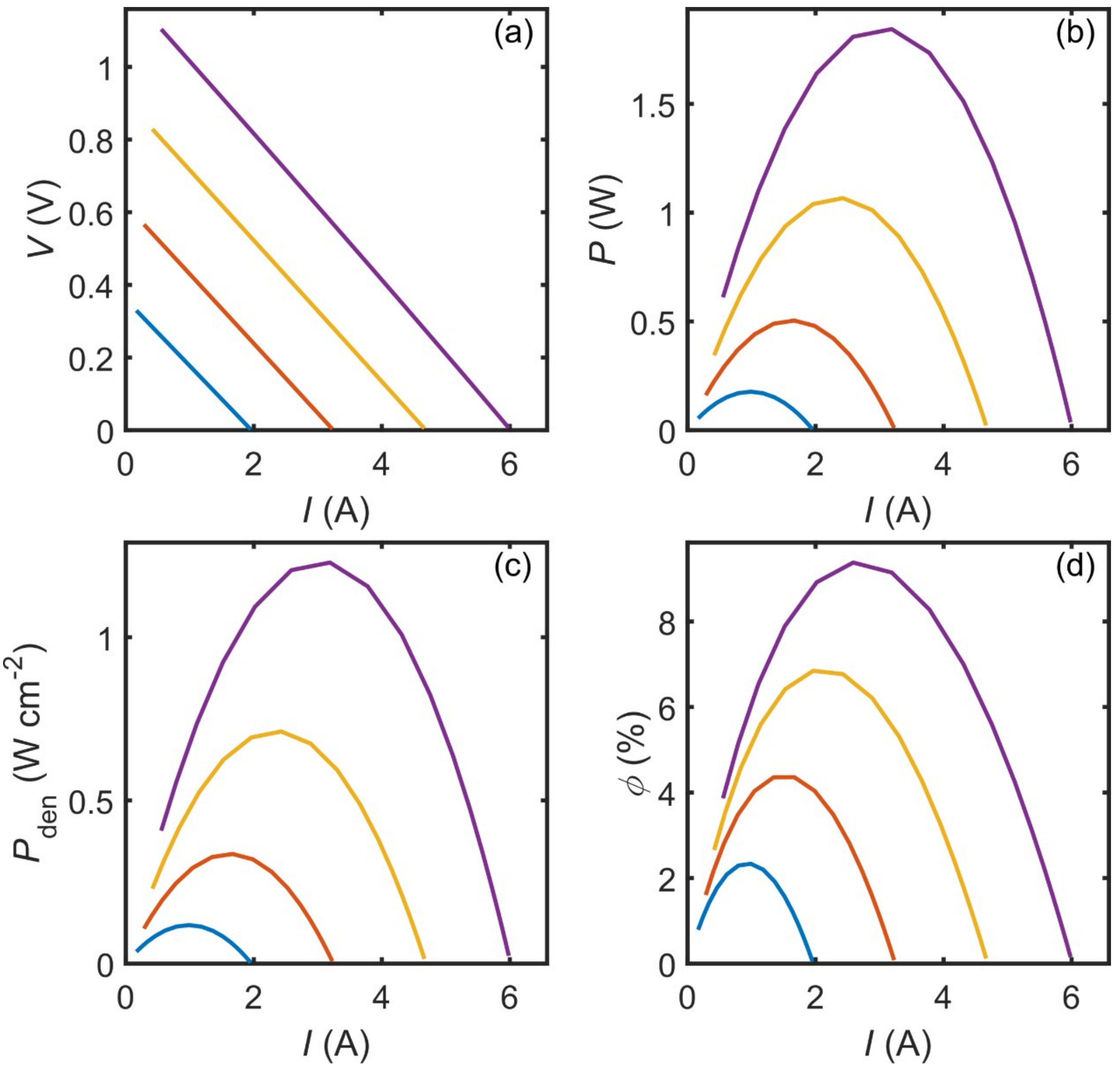

Fig. S41 Device simulation results of as-developed p-type $Ge_{0.89}Cr_{0.03}Sb_{0.08}Te$ and reported n-type $PbS(Bi_2S_3)_{0.01}(PbCl_2)_{0.01}$.[43] Generated (a) voltage (V), (b) output electrical power (P), (c) output electrical power density (P_{den}), and (d) conversion efficiency (ϕ) of the module under cold side temperature of 300 K and hot side temperatures of 480, 580, 680, and 780 K.

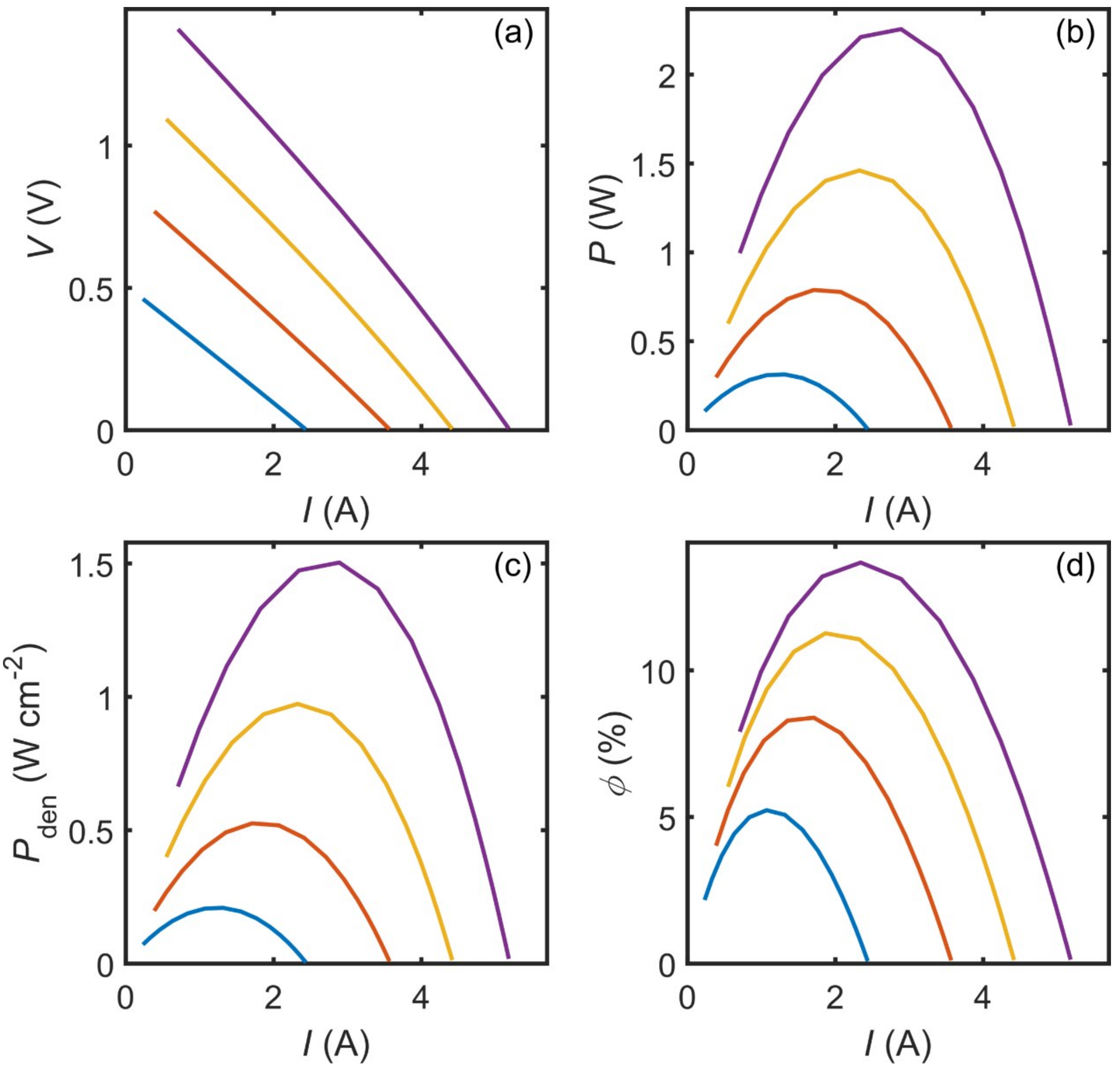

Fig. S42 Device simulation results of as-developed p-type $Ge_{0.89}Cr_{0.03}Sb_{0.08}Te$ and reported n-type PbTe+8% PbS.[44] Generated (a) voltage (V), (b) output electrical power (P), (c) output electrical power density (P_{den}), and (d) conversion efficiency (ϕ) of the module under cold side temperature of 300 K and hot side temperatures of 480, 580, 680, and 780 K.

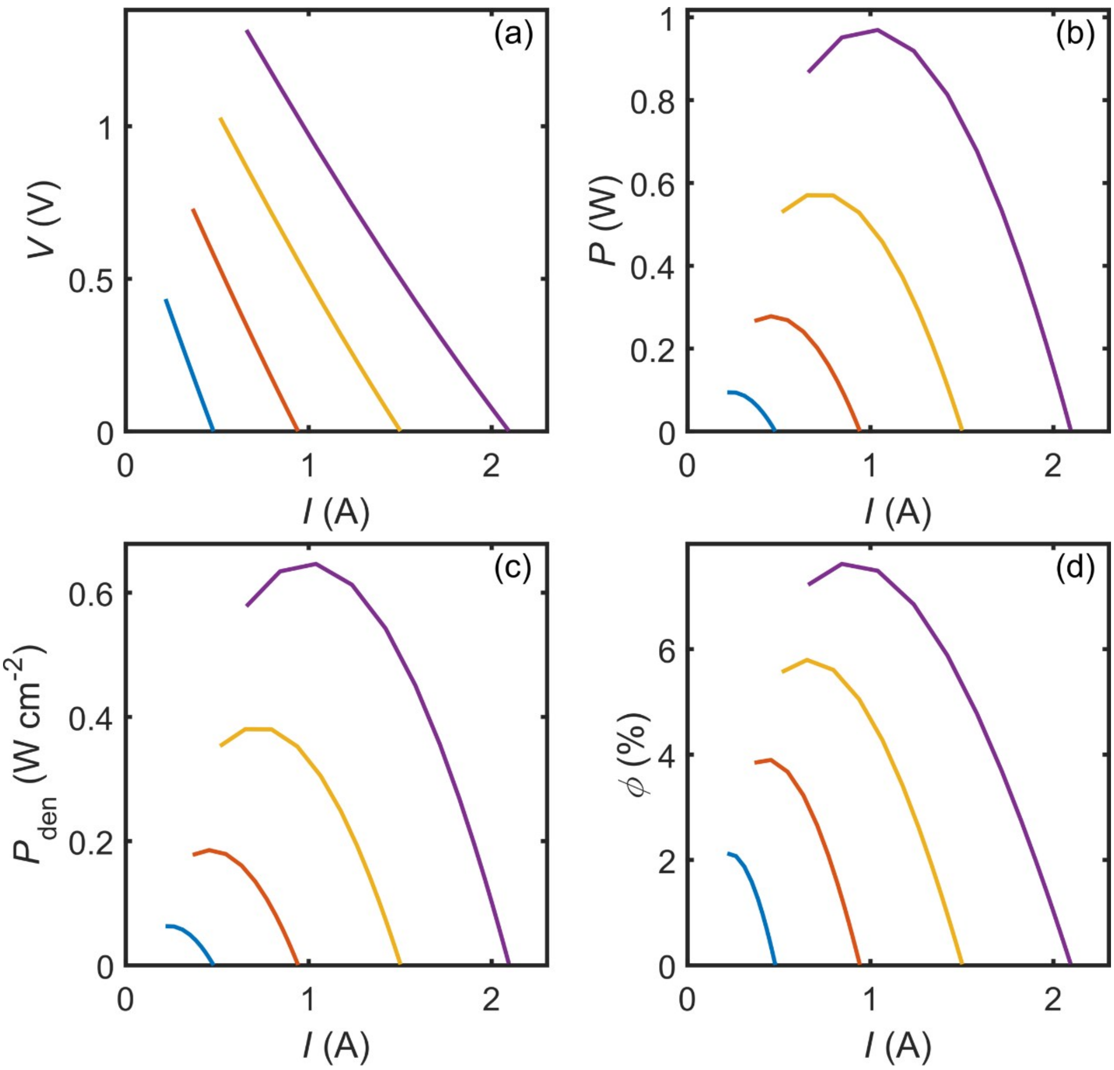

Fig. S43 Device simulation results of as-developed p-type $Ge_{0.89}Cr_{0.03}Sb_{0.08}Te$ and reported n-type $PbTe_{0.9}S_{0.1}$-3% Ag_2Te.[45] Generated (a) voltage (V), (b) output electrical power (P), (c) output electrical power density (P_{den}), and (d) conversion efficiency (ϕ) of the module under cold side temperature of 300 K and hot side temperatures of 480, 580, 680, and 780 K.

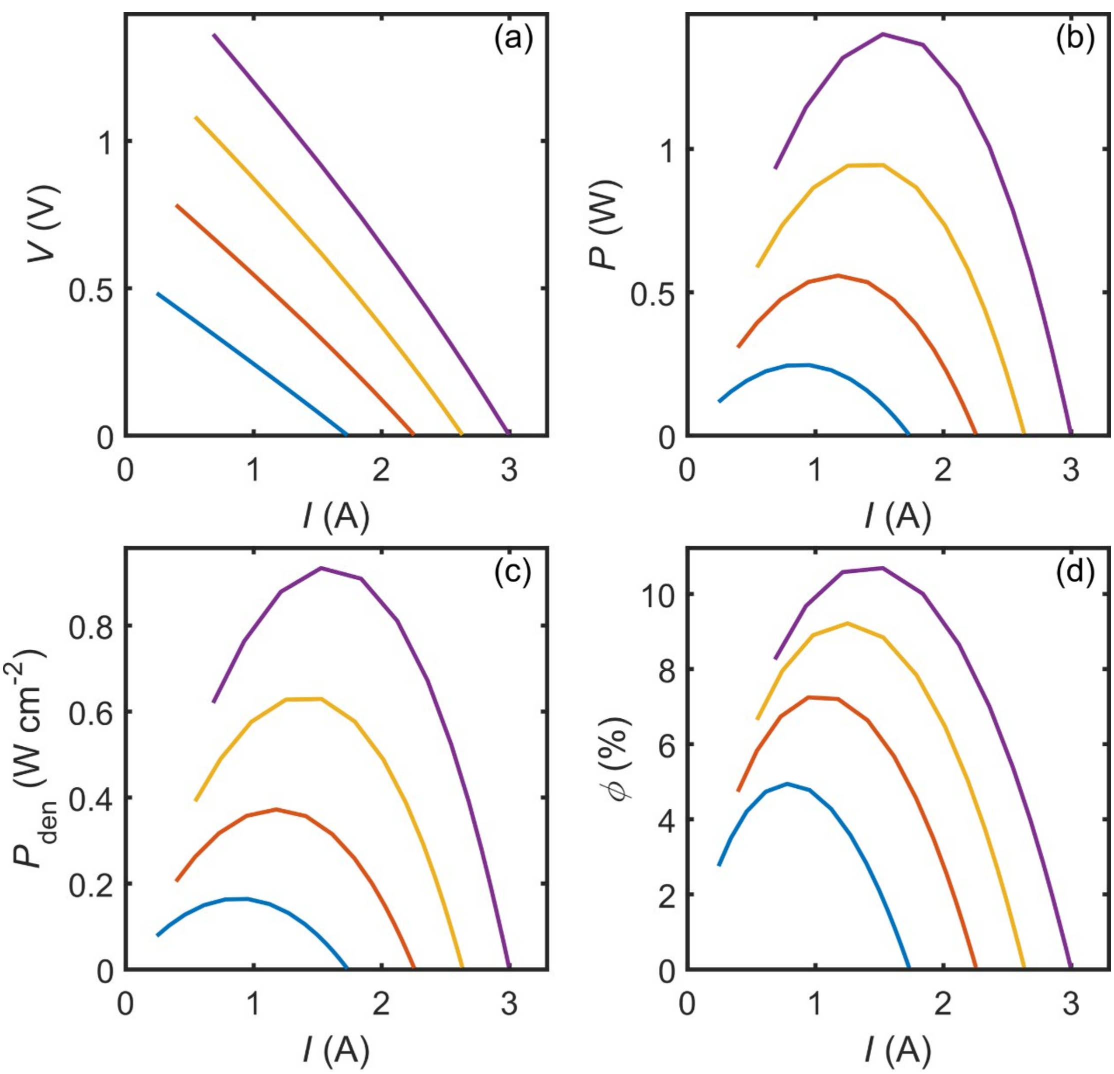

Fig. S44 Device simulation results of as-developed p-type $Ge_{0.89}Cr_{0.03}Sb_{0.08}Te$ and reported n-type $Sb_{0.004}Pb_{0.996}Te_{0.88}S_{0.12}$.[46] Generated (a) voltage (V), (b) output electrical power (P), (c) output electrical power density (P_{den}), and (d) conversion efficiency (ϕ) of the module under cold side temperature of 300 K and hot side temperatures of 480, 580, 680, and 780 K.

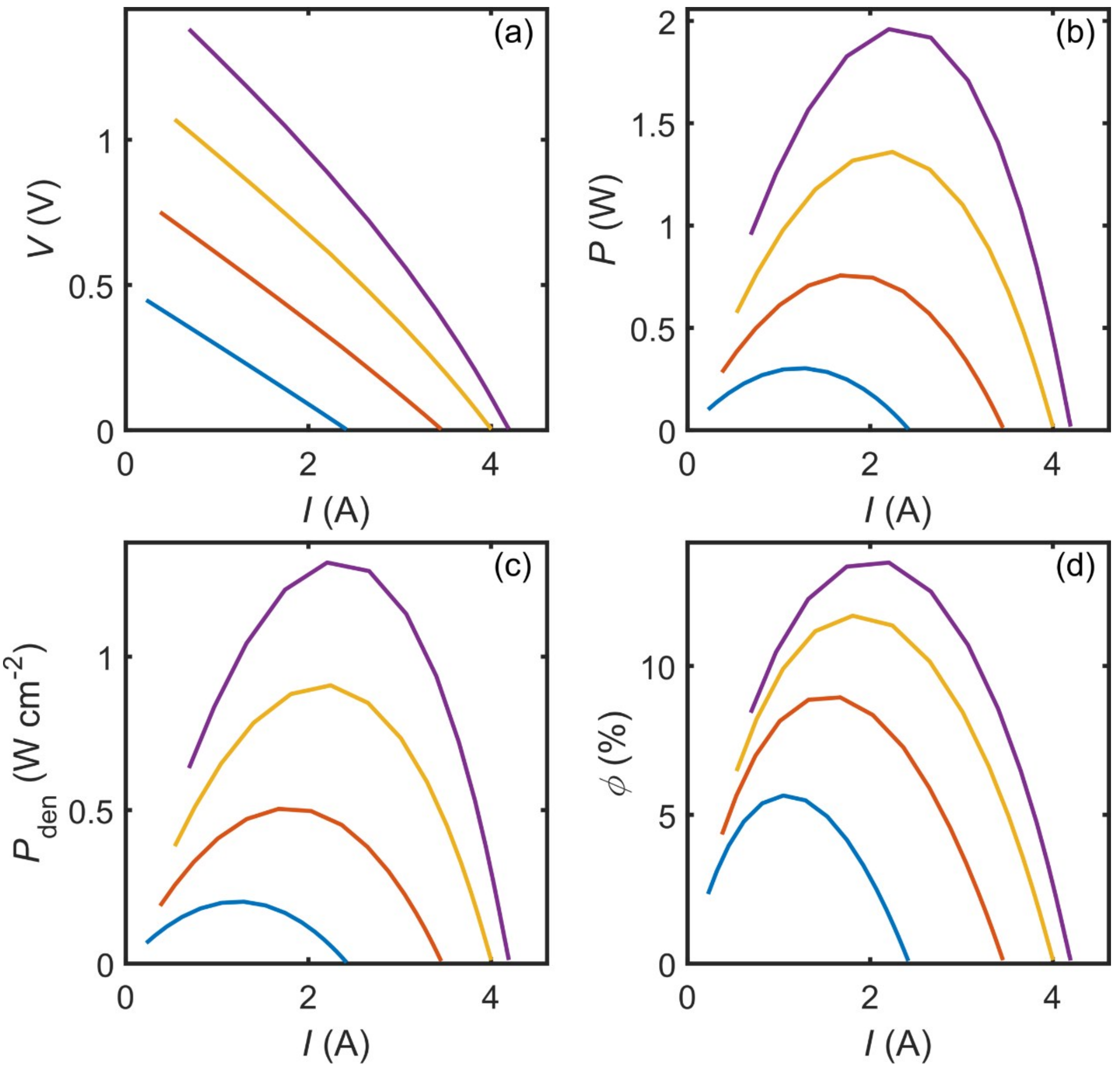

Fig. S45 Device simulation results of as-developed p-type $Ge_{0.89}Cr_{0.03}Sb_{0.08}Te$ and reported n-type $(Bi_{0.001}Pb_{0.999}Te)_{0.88}(PbS)_{0.12}$.[47] Generated (a) voltage (V), (b) output electrical power (P), (c) output electrical power density (P_{den}), and (d) conversion efficiency (ϕ) of the module under cold side temperature of 300 K and hot side temperatures of 480, 580, 680, and 780 K.

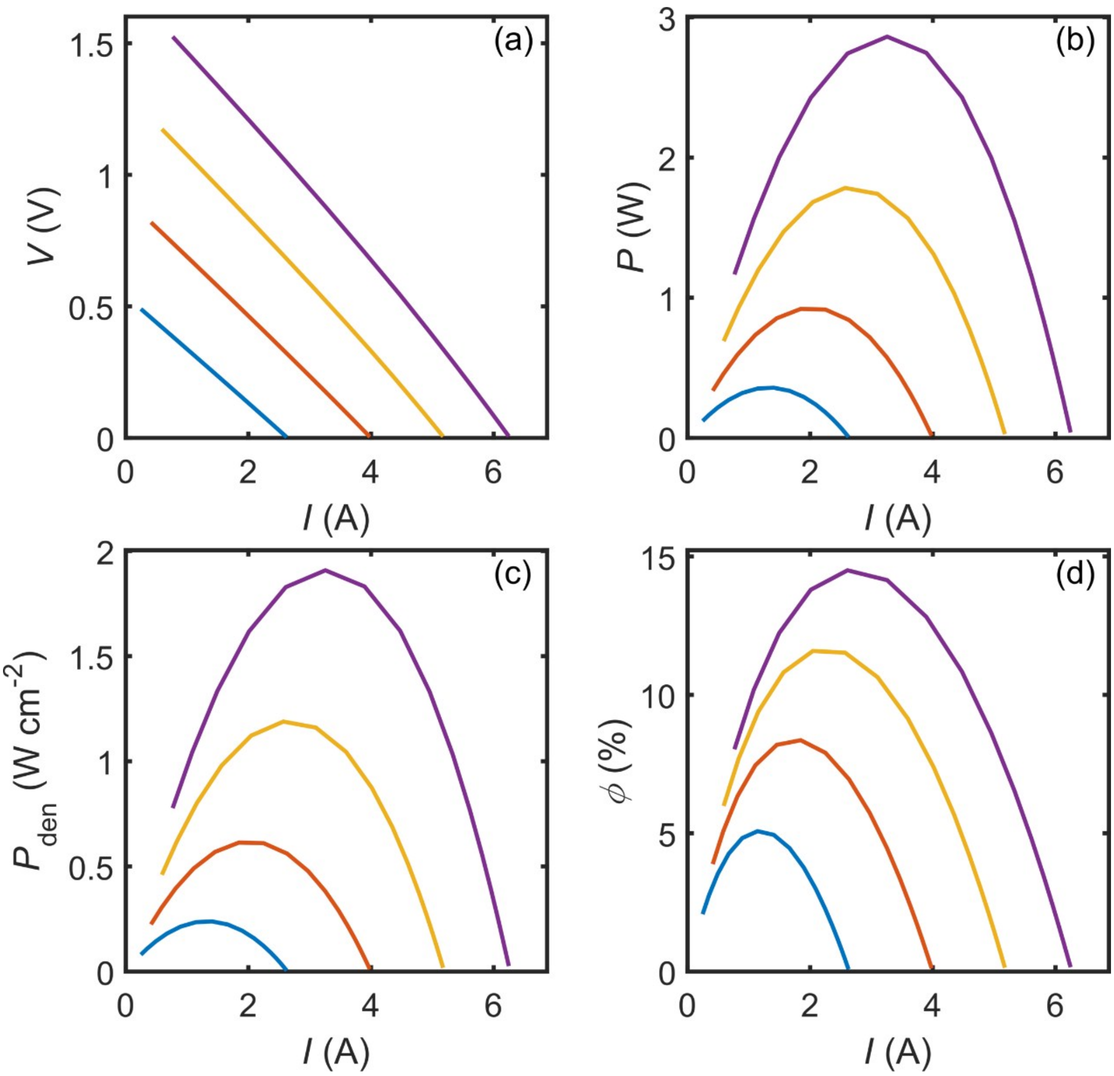

Fig. S46 Device simulation results of as-developed p-type $Ge_{0.89}Cr_{0.03}Sb_{0.08}Te$ and reported n-type 2mol%ZnTe+0.025mol%PbI_2+PbTe.[48] Generated (a) voltage (V), (b) output electrical power (P), (c) output electrical power density (P_{den}), and (d) conversion efficiency (ϕ) of the module under cold side temperature of 300 K and hot side temperatures of 480, 580, 680, and 780 K.

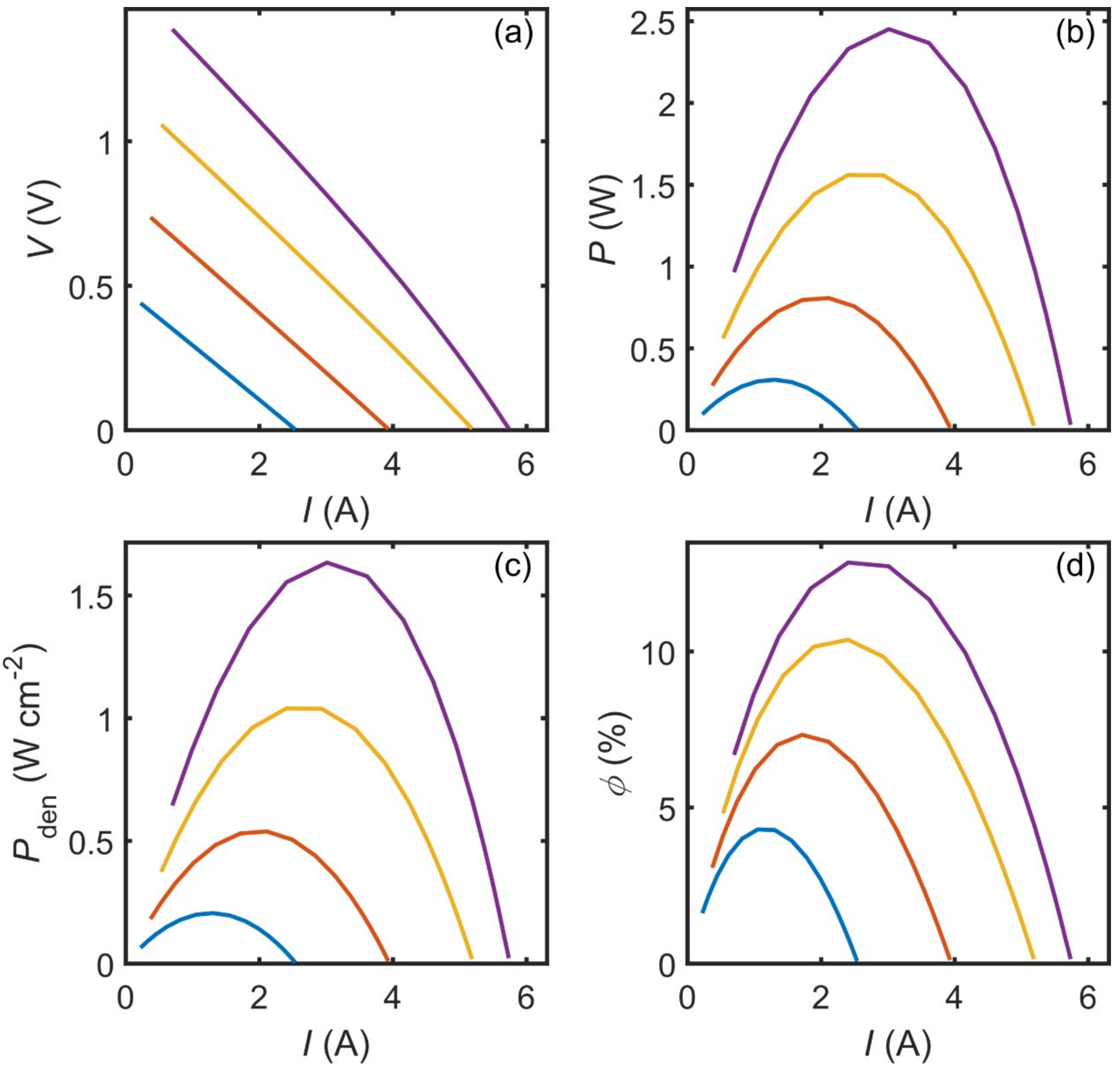

Fig. S47 Device simulation results of as-developed p-type $Ge_{0.89}Cr_{0.03}Sb_{0.08}Te$ and reported n-type $Pb_{0.99}SeAl_{0.01}$.[49] Generated (a) voltage (V), (b) output electrical power (P), (c) output electrical power density (P_{den}), and (d) conversion efficiency (ϕ) of the module under cold side temperature of 300 K and hot side temperatures of 480, 580, 680, and 780 K.

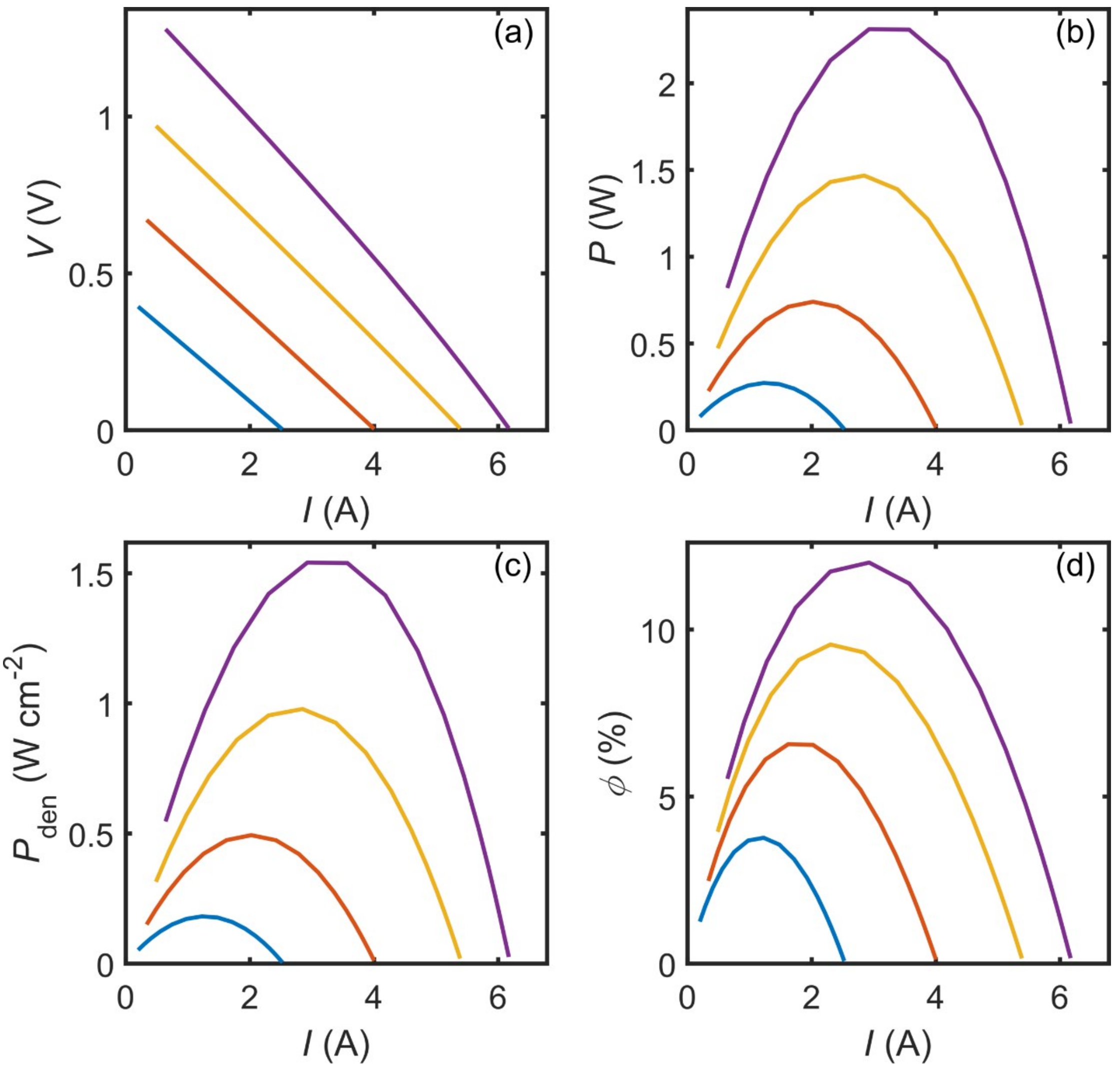

Fig. S48 Device simulation results of as-developed p-type $Ge_{0.89}Cr_{0.03}Sb_{0.08}Te$ and reported n-type PbSe-16%PbS.[50] Generated (a) voltage (V), (b) output electrical power (P), (c) output electrical power density (P_{den}), and (d) conversion efficiency (ϕ) of the module under cold side temperature of 300 K and hot side temperatures of 480, 580, 680, and 780 K.

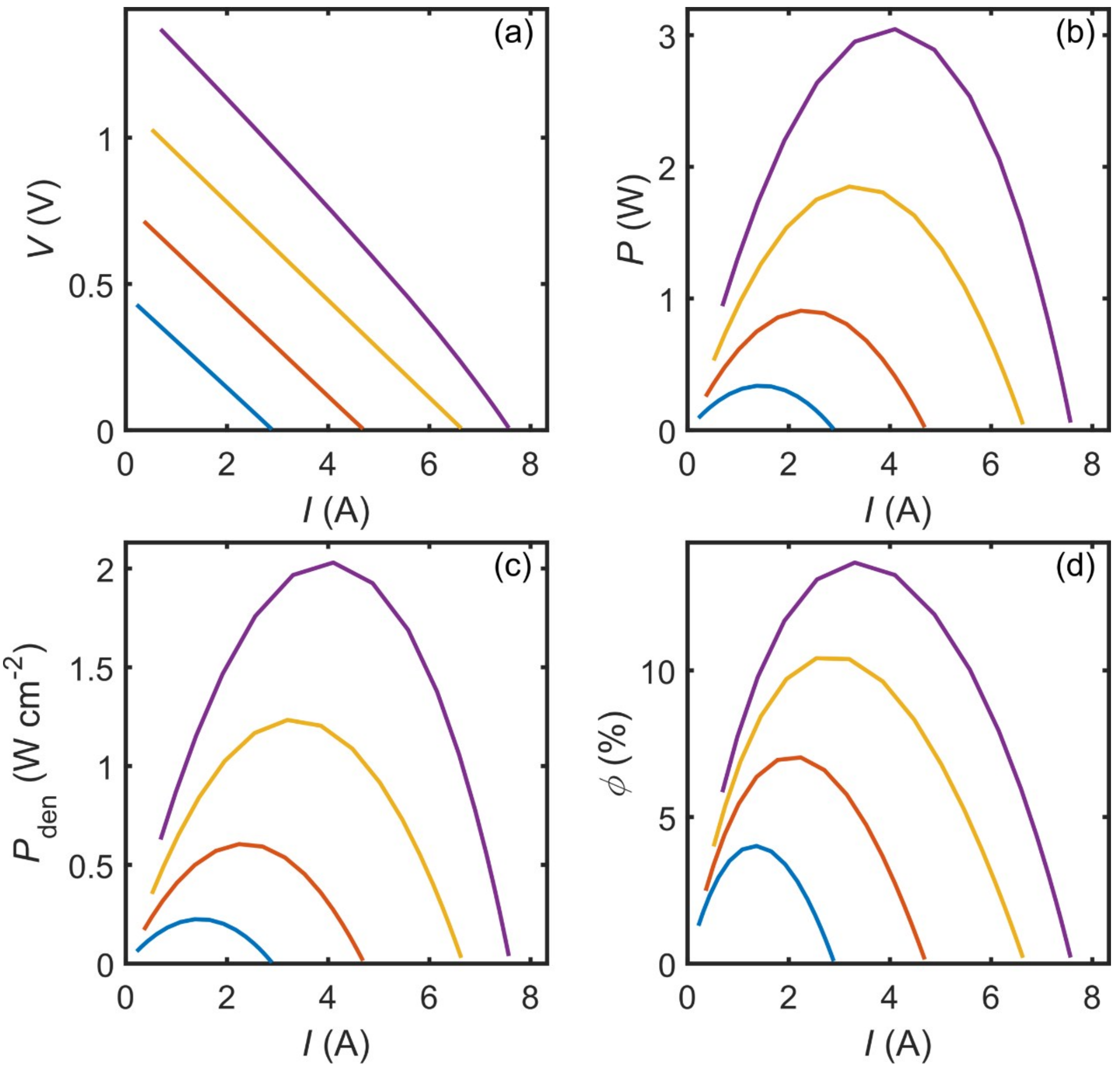

Fig. S49 Device simulation results of as-developed p-type $Ge_{0.89}Cr_{0.03}Sb_{0.08}Te$ and reported n-type $PbTe_{0.998}T_{0.002}$-3%Sb.[51] Generated (a) voltage (V), (b) output electrical power (P), (c) output electrical power density (P_{den}), and (d) conversion efficiency (ϕ) of the module under cold side temperature of 300 K and hot side temperatures of 480, 580, 680, and 780 K.

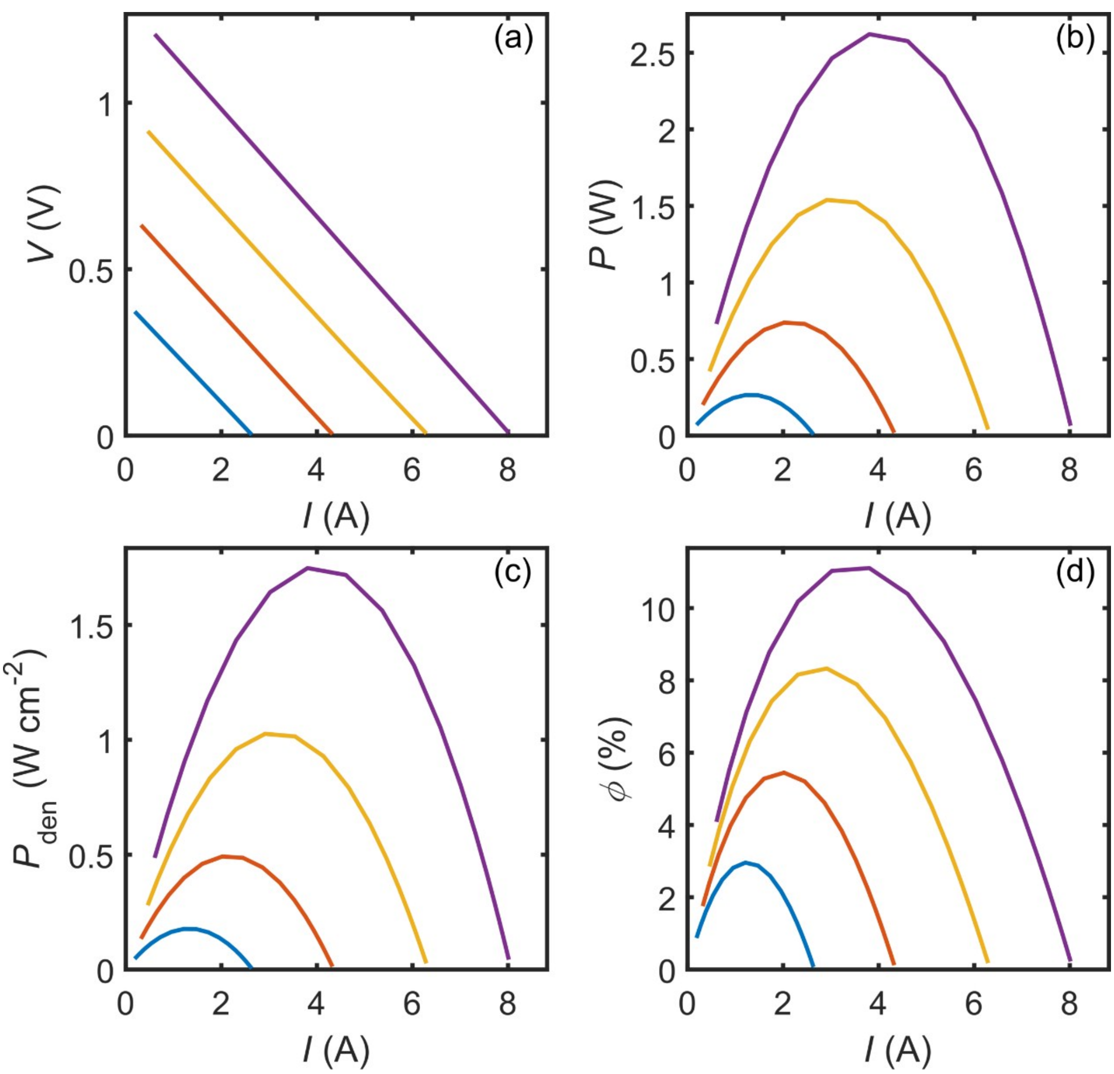

Fig. S50 Device simulation results of as-developed p-type $Ge_{0.89}Cr_{0.03}Sb_{0.08}Te$ and reported n-type $Pb_{1-x}La_xTe$.[2] Generated (a) voltage (V), (b) output electrical power (P), (c) output electrical power density (P_{den}), and (d) conversion efficiency (ϕ) of the module under cold side temperature of 300 K and hot side temperatures of 480, 580, 680, and 780 K.

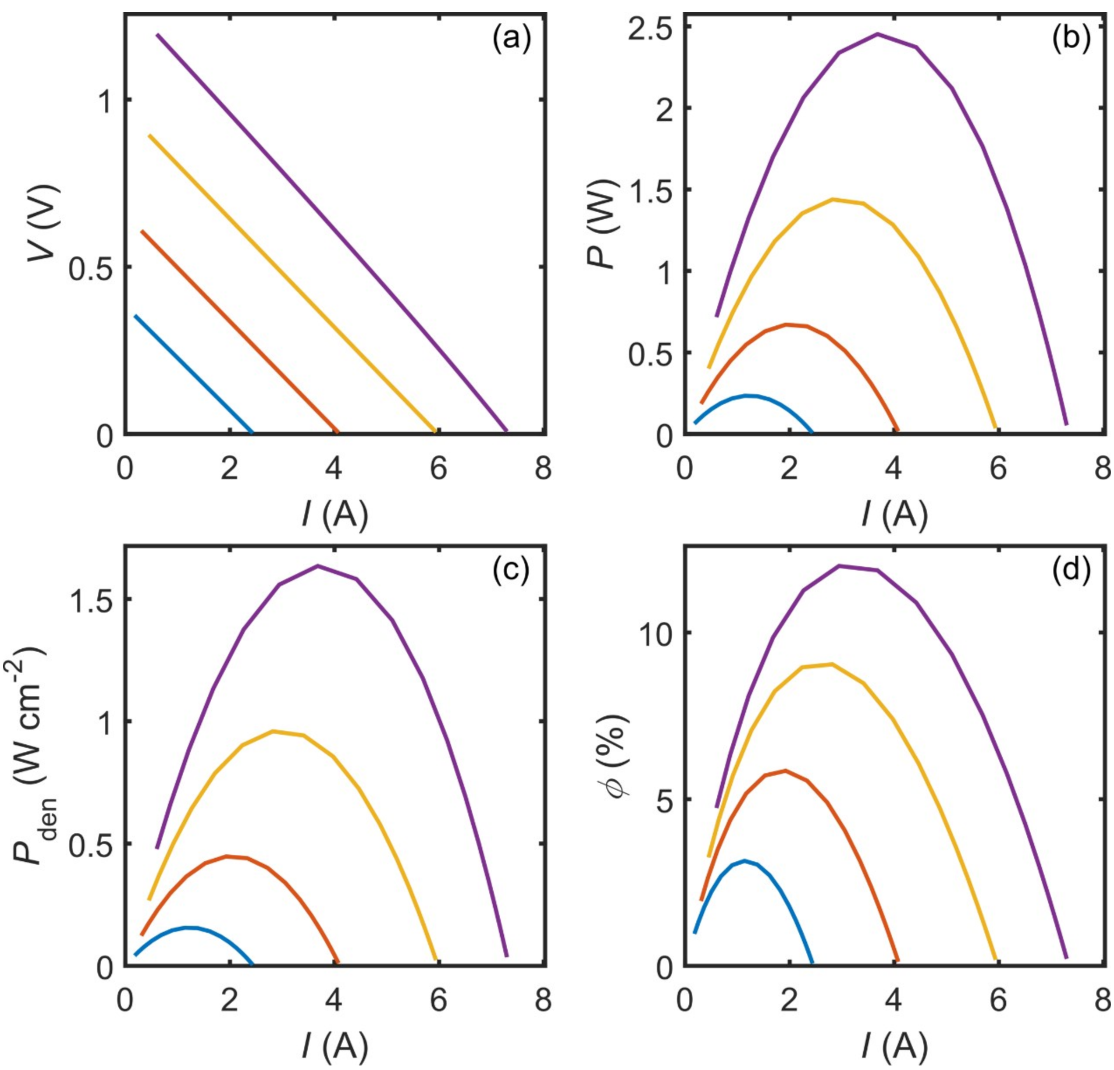

Fig. S51 Device simulation results of as-developed p-type $Ge_{0.89}Cr_{0.03}Sb_{0.08}Te$ and reported n-type $(Pb_{0.93}Sn_{0.07})(Te_{0.93}Se_{0.07})$.[52] Generated (a) voltage (V), (b) output electrical power (P), (c) output electrical power density (P_{den}), and (d) conversion efficiency (ϕ) of the module under cold side temperature of 300 K and hot side temperatures of 480, 580, 680, and 780 K.

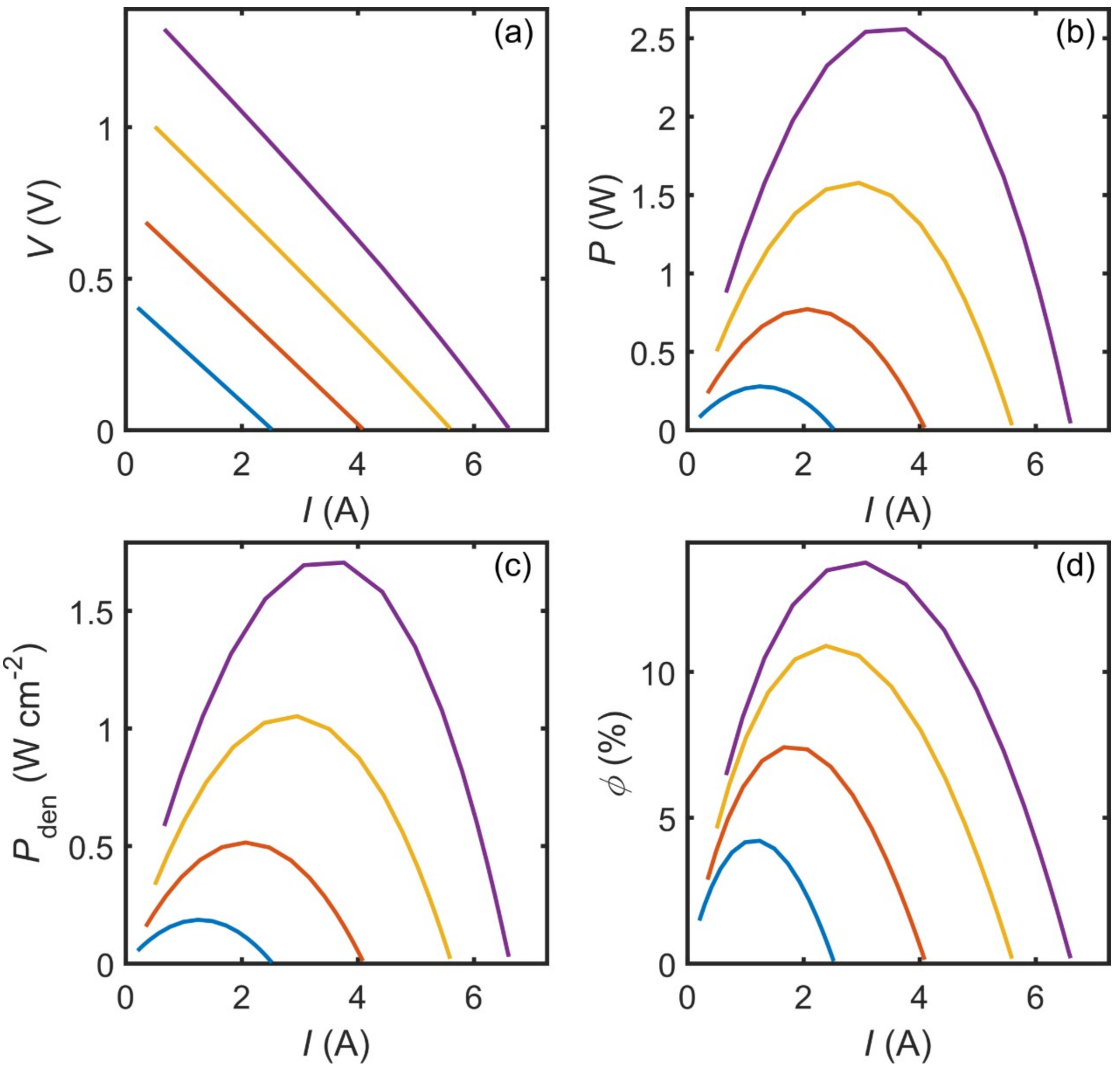

Fig. S52 Device simulation results of as-developed p-type $Ge_{0.89}Cr_{0.03}Sb_{0.08}Te$ and reported n-type PbTe–4%MnTe.[53] Generated (a) voltage (V), (b) output electrical power (P), (c) output electrical power density (P_{den}), and (d) conversion efficiency (ϕ) of the module under cold side temperature of 300 K and hot side temperatures of 480, 580, 680, and 780 K.

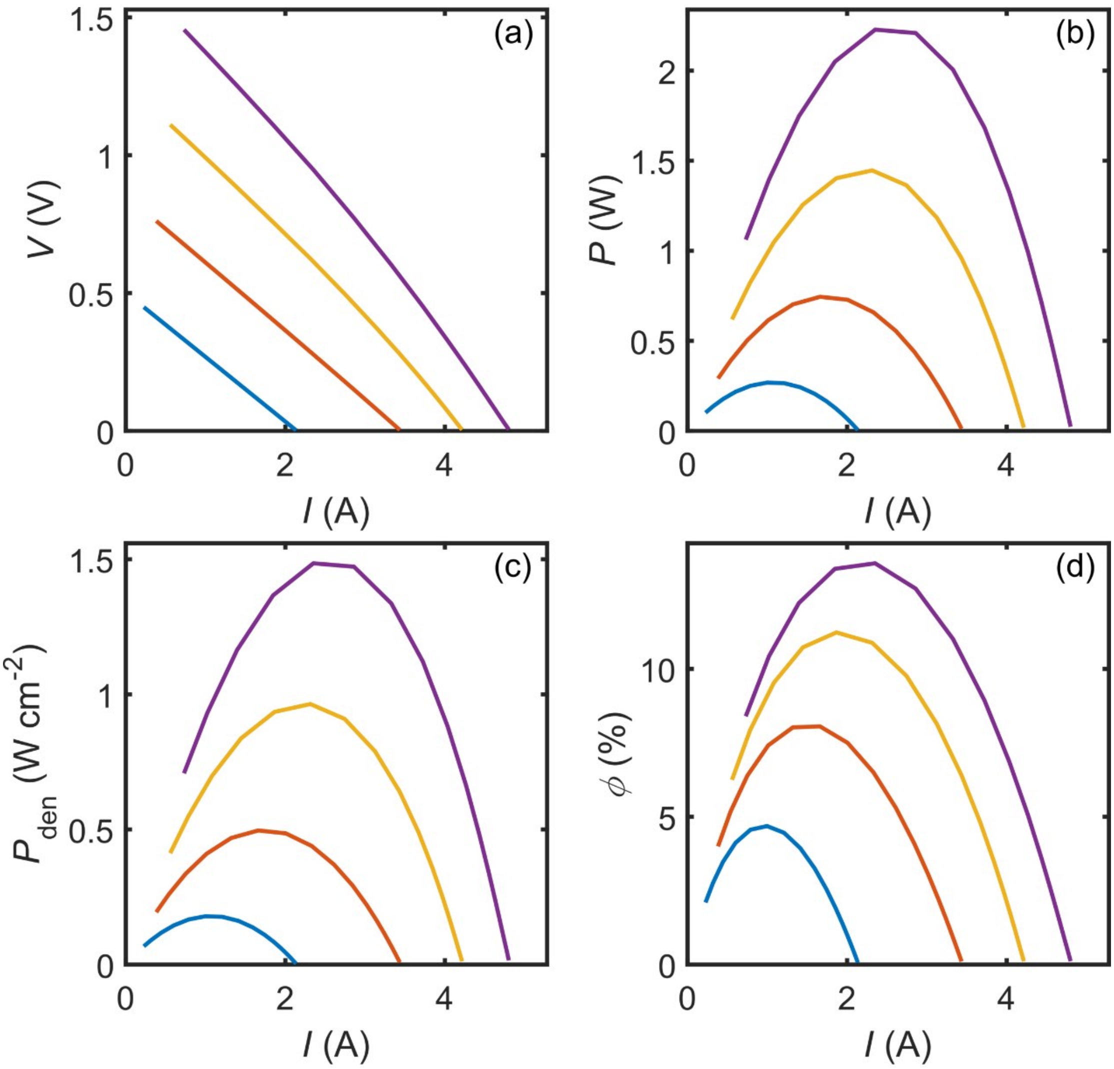

Fig. S53 Device simulation results of as-developed p-type $Ge_{0.89}Cr_{0.03}Sb_{0.08}Te$ and reported n-type $Pb_{0.988}Sb_{0.012}Te$–13%GeTe.[54] Generated (a) voltage (V), (b) output electrical power (P), (c) output electrical power density (P_{den}), and (d) conversion efficiency (ϕ) of the module under cold side temperature of 300 K and hot side temperatures of 480, 580, 680, and 780 K.

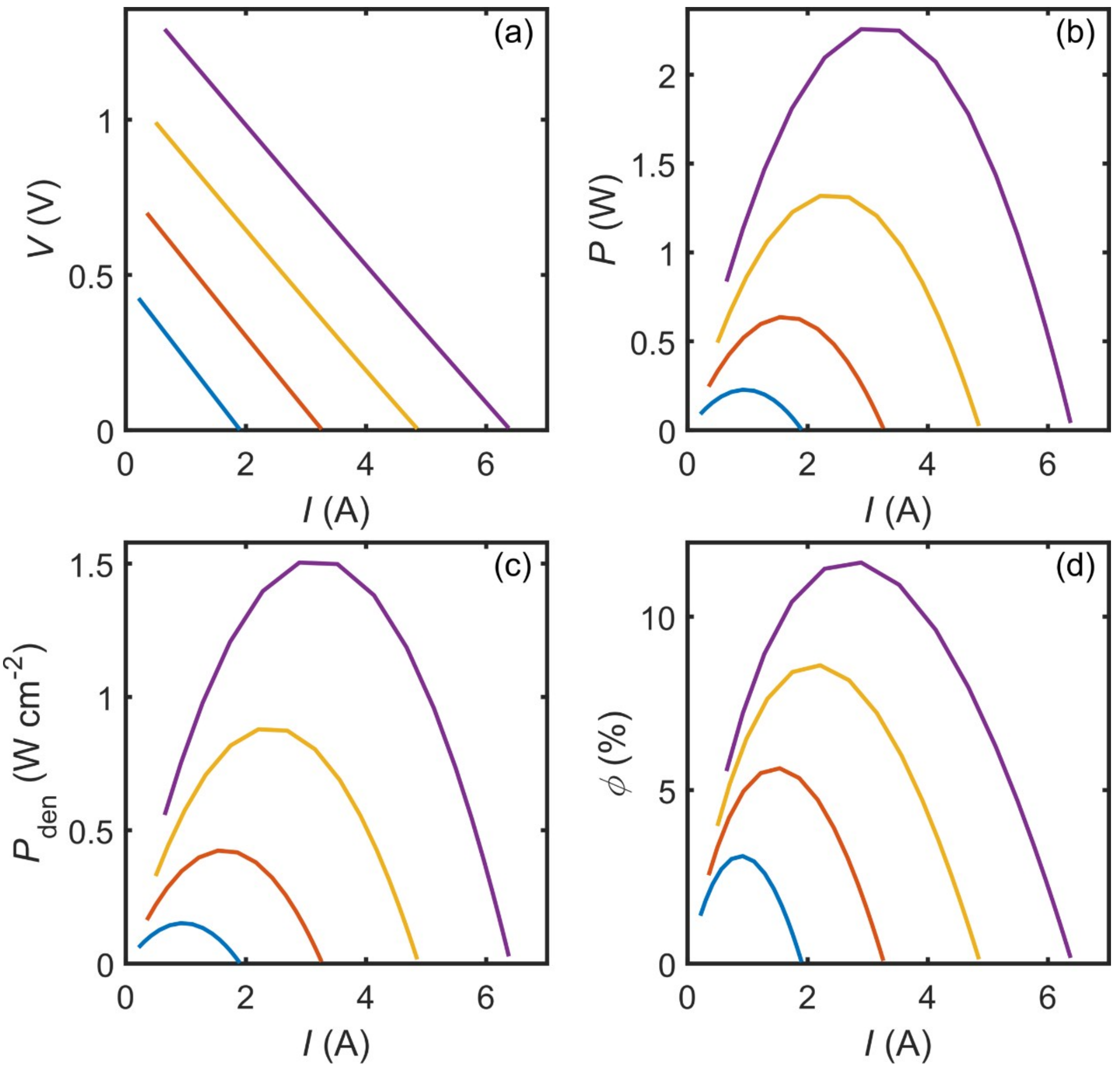

Fig. S54 Device simulation results of as-developed p-type $Ge_{0.89}Cr_{0.03}Sb_{0.08}Te$ and reported n-type PbTe-4%InSb.[55] Generated (a) voltage (V), (b) output electrical power (P), (c) output electrical power density (P_{den}), and (d) conversion efficiency (ϕ) of the module under cold side temperature of 300 K and hot side temperatures of 480, 580, 680, and 780 K.

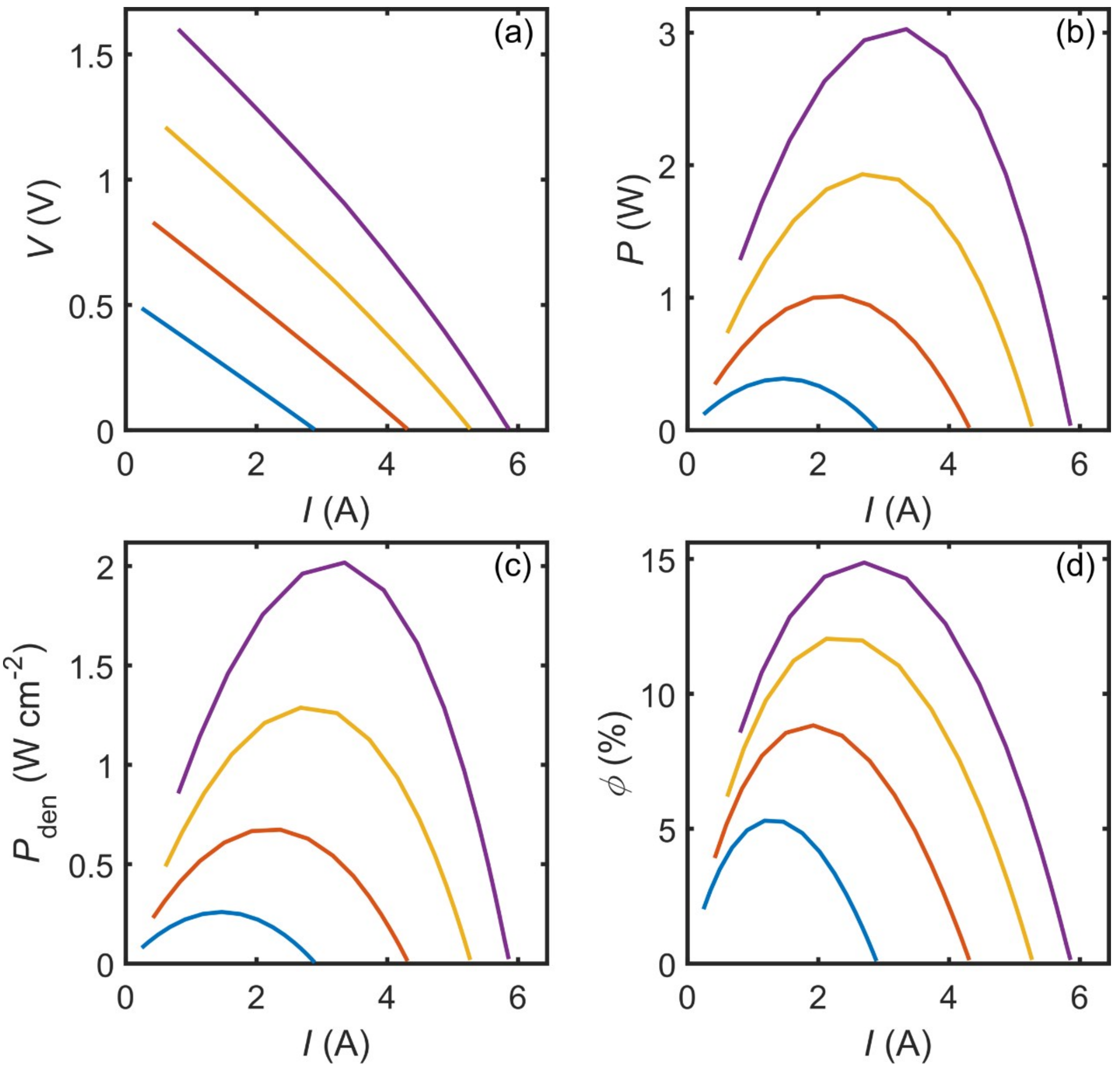

Fig. S55 Device simulation results of as-developed p-type $Ge_{0.89}Cr_{0.03}Sb_{0.08}Te$ and reported n-type $AgPb_mSbTe_{2+m}$.[56] Generated (a) voltage (V), (b) output electrical power (P), (c) output electrical power density (P_{den}), and (d) conversion efficiency (ϕ) of the module under cold side temperature of 300 K and hot side temperatures of 480, 580, 680, and 780 K.

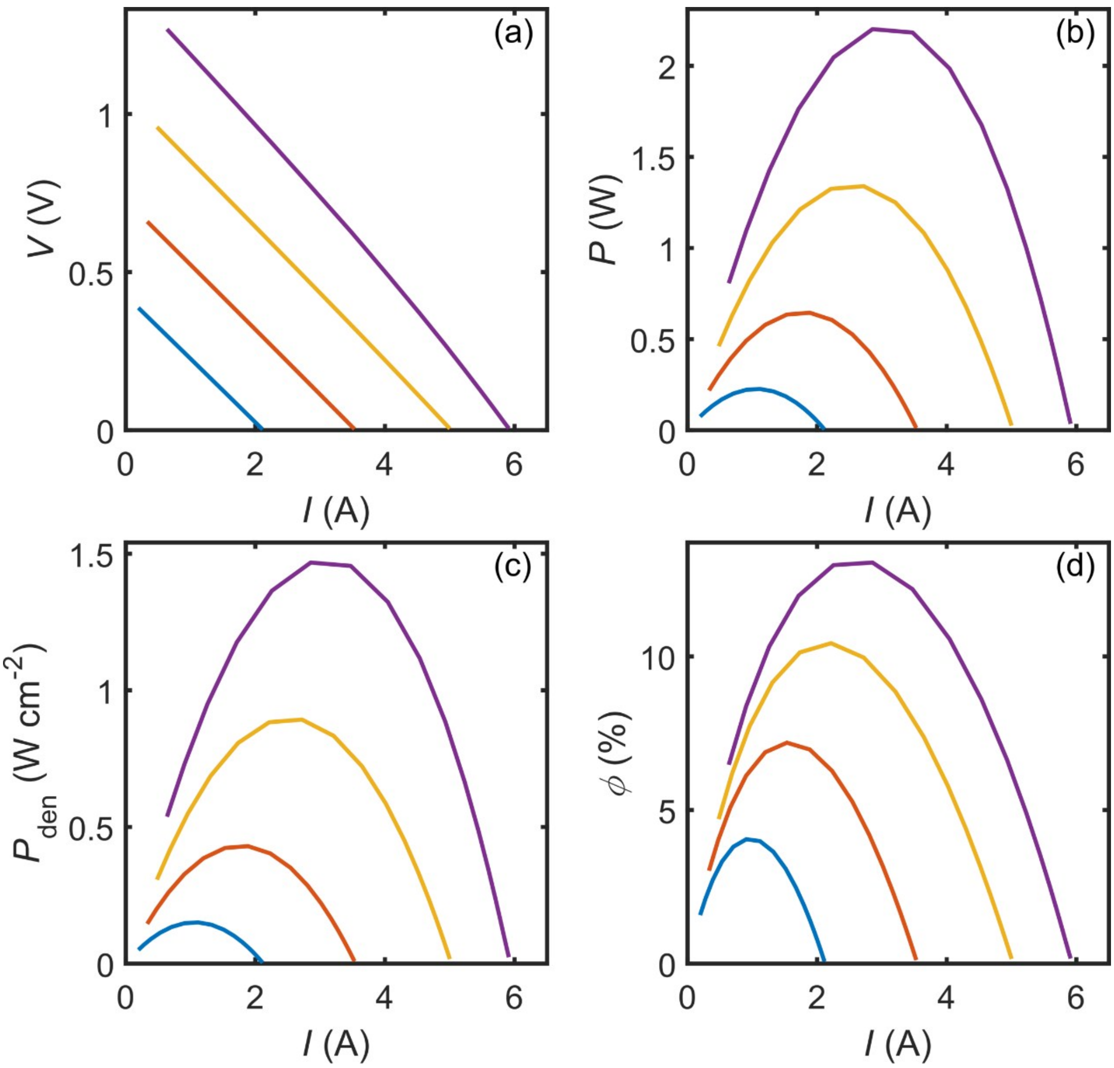

Fig. S56 Device simulation results of as-developed p-type $Ge_{0.89}Cr_{0.03}Sb_{0.08}Te$ and reported n-type $Pb_{0.9955}Sb_{0.0045}Se$–12%GeSe.[57] Generated (a) voltage (V), (b) output electrical power (P), (c) output electrical power density (P_{den}), and (d) conversion efficiency (ϕ) of the module under cold side temperature of 300 K and hot side temperatures of 480, 580, 680, and 780 K.

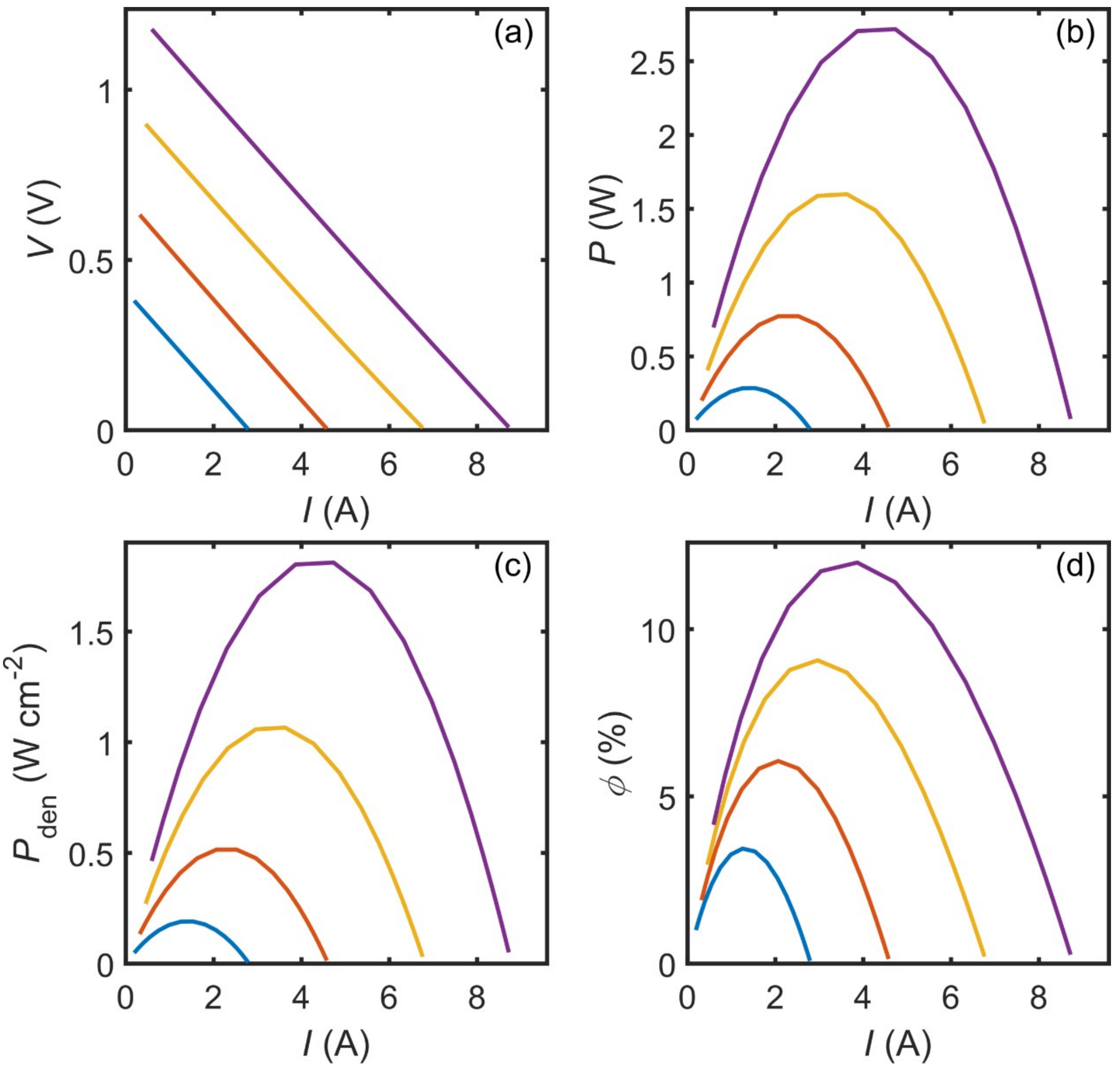

Fig. S57 Device simulation results of as-developed p-type $Ge_{0.89}Cr_{0.03}Sb_{0.08}Te$ and reported n-type PbTe-5.5%Cu_2Te.[58] Generated (a) voltage (V), (b) output electrical power (P), (c) output electrical power density (P_{den}), and (d) conversion efficiency (ϕ) of the module under cold side temperature of 300 K and hot side temperatures of 480, 580, 680, and 780 K.

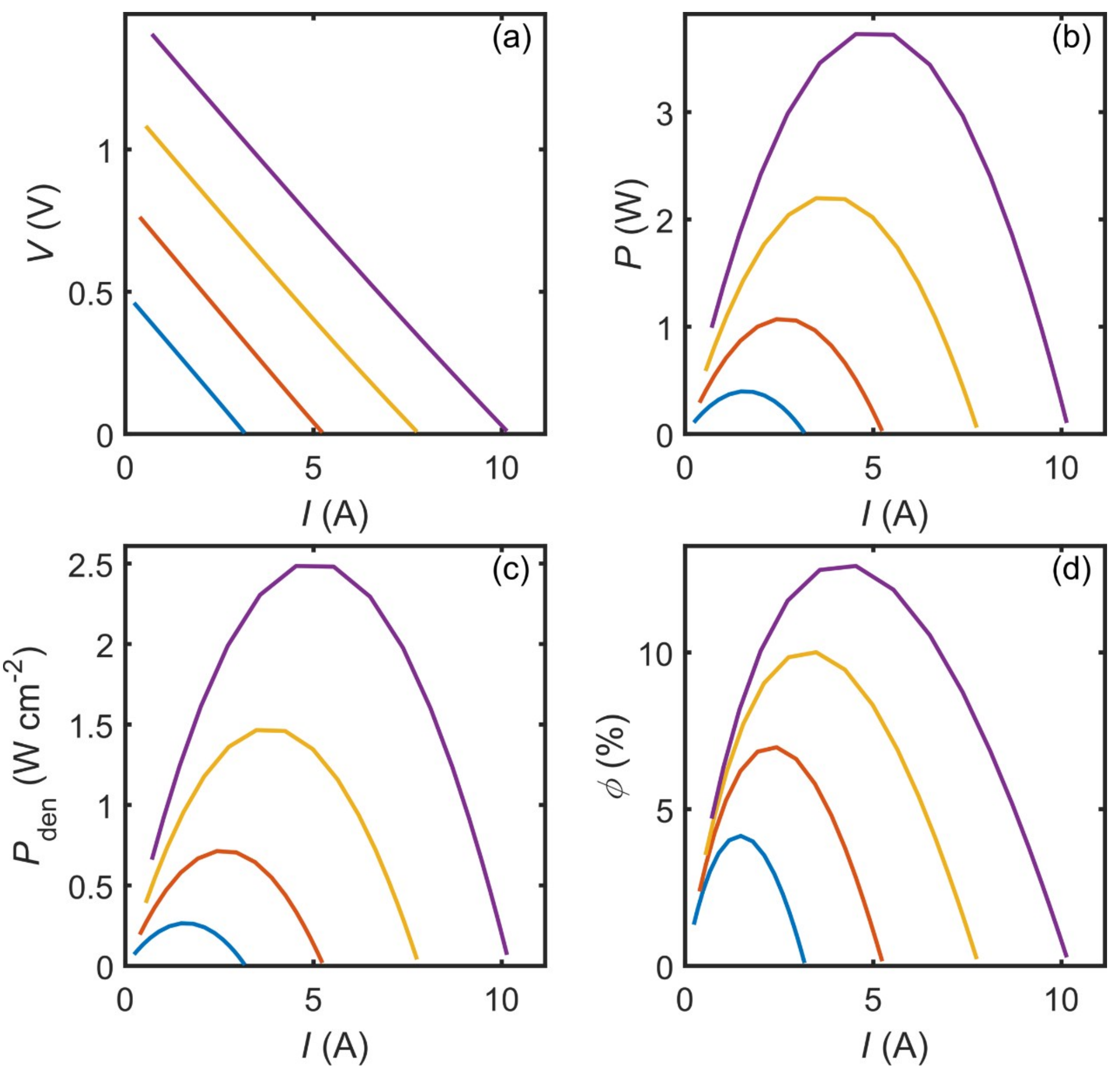

Fig. S58 Device simulation results of as-developed p-type $Ge_{0.89}Cr_{0.03}Sb_{0.08}Te$ and reported n-type $Mg_2Sn_{0.75}Ge_{0.25}$.[59] Generated (a) voltage (V), (b) output electrical power (P), (c) output electrical power density (P_{den}), and (d) conversion efficiency (ϕ) of the module under cold side temperature of 300 K and hot side temperatures of 480, 580, 680, and 780 K.

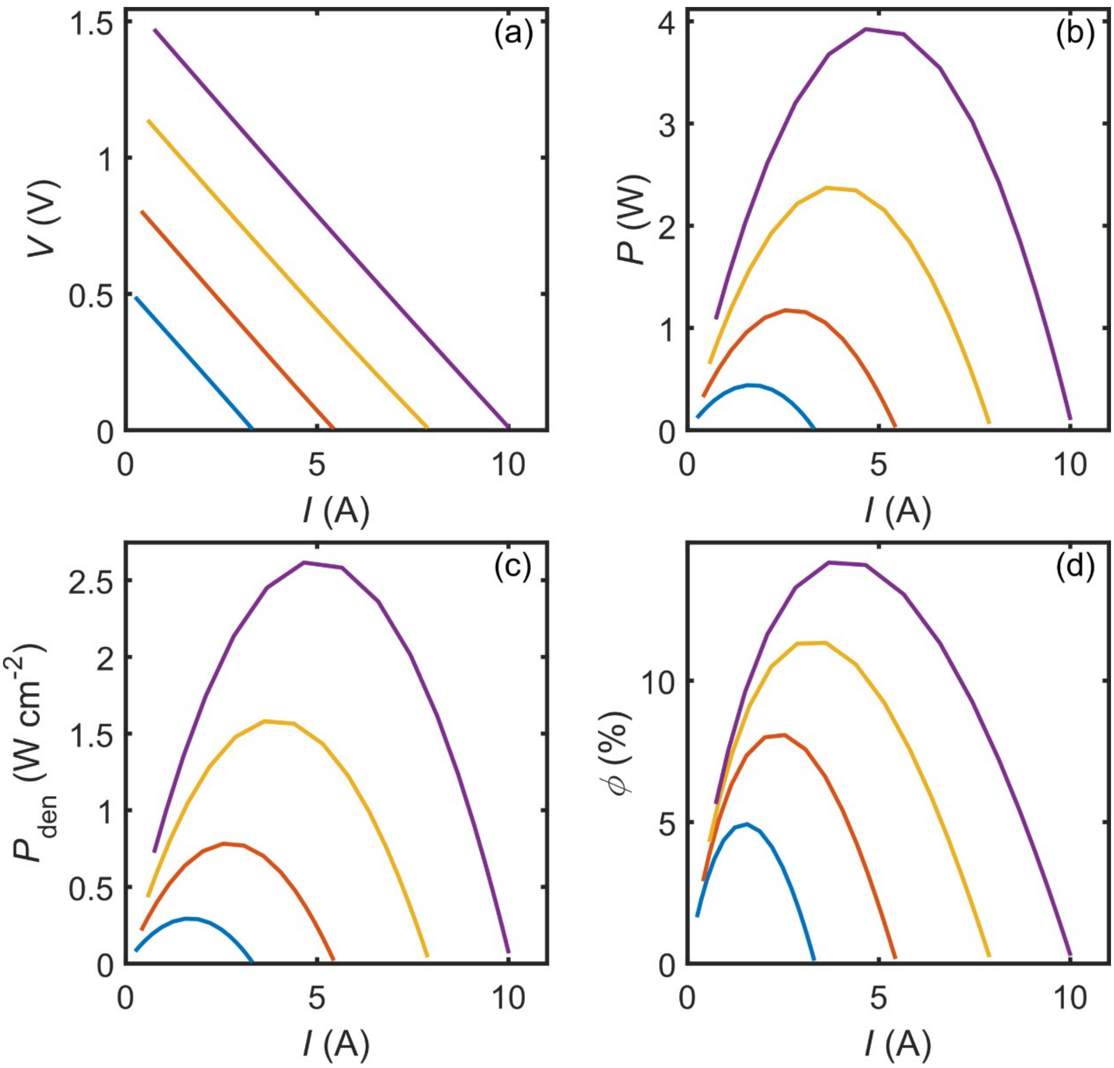

Fig. S59 Device simulation results of as-developed p-type $Ge_{0.89}Cr_{0.03}Sb_{0.08}Te$ and reported n-type $Mg_2Si_{0.3}Sn_{0.7}Sb_{0.006}$.[60] Generated (a) voltage (V), (b) output electrical power (P), (c) output electrical power density (P_{den}), and (d) conversion efficiency (ϕ) of the module under cold side temperature of 300 K and hot side temperatures of 480, 580, 680, and 780 K.

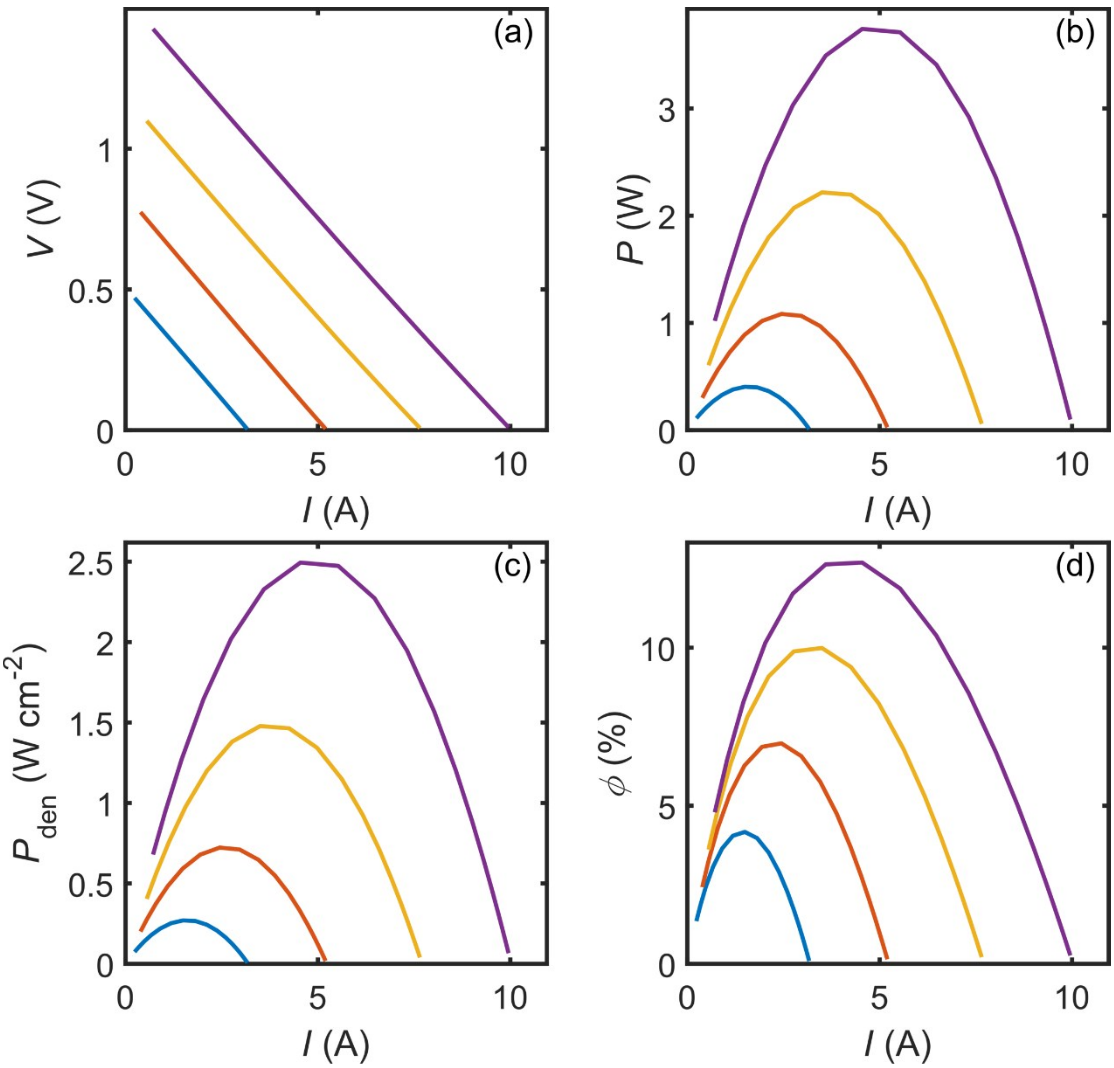

Fig. S60 Device simulation results of as-developed p-type $Ge_{0.89}Cr_{0.03}Sb_{0.08}Te$ and reported n-type $Mg_2Sn_{0.78}Ge_{0.2}Sb_{0.02}$.[61] Generated (a) voltage (V), (b) output electrical power (P), (c) output electrical power density (P_{den}), and (d) conversion efficiency (ϕ) of the module under cold side temperature of 300 K and hot side temperatures of 480, 580, 680, and 780 K.

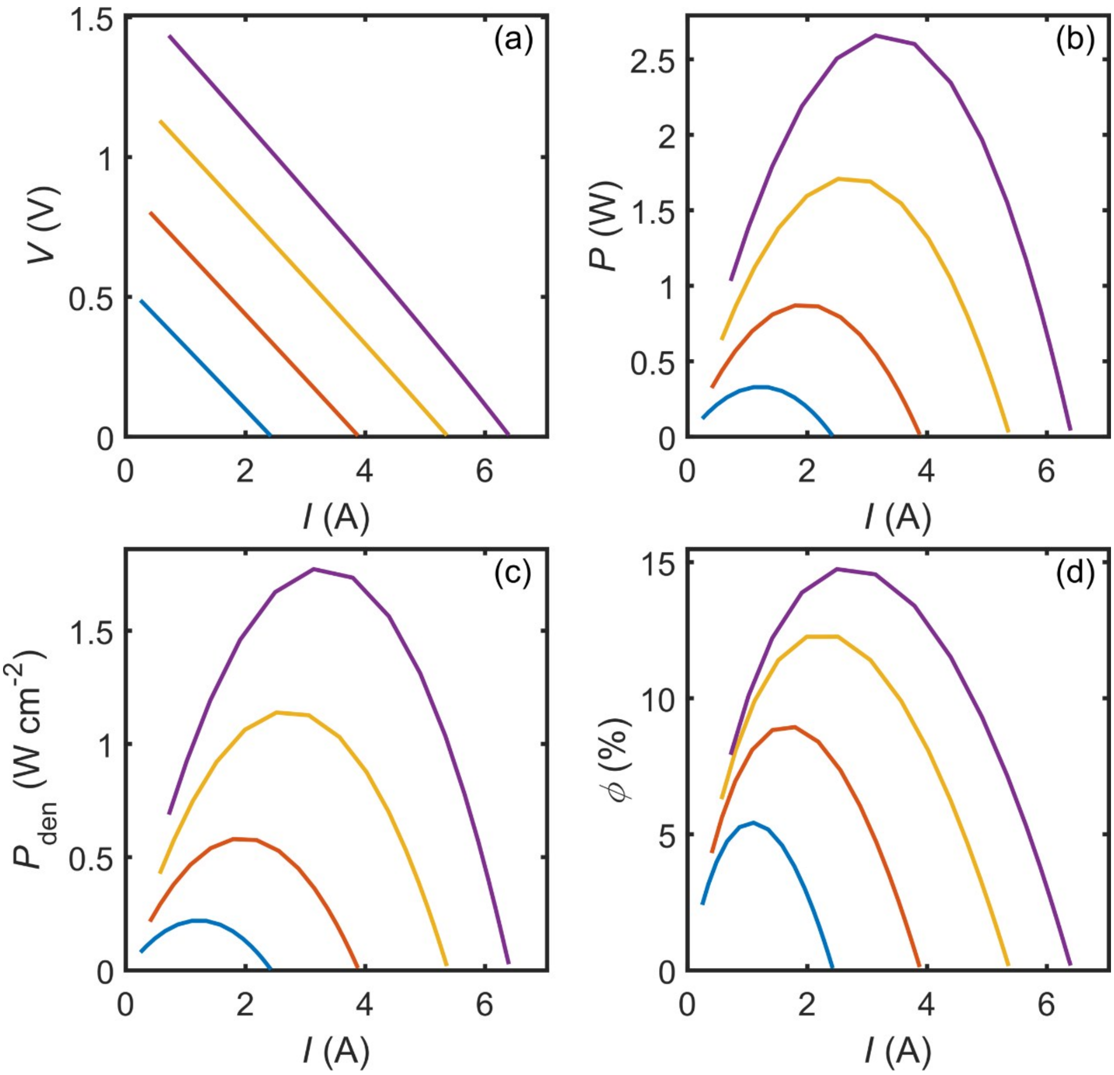

Fig. S61 Device simulation results of as-developed p-type $Ge_{0.89}Cr_{0.03}Sb_{0.08}Te$ and reported n-type Sb-doped $Mg_2Si_{0.5}Sn_{0.5}$.[62] Generated (a) voltage (V), (b) output electrical power (P), (c) output electrical power density (P_{den}), and (d) conversion efficiency (ϕ) of the module under cold side temperature of 300 K and hot side temperatures of 480, 580, 680, and 780 K.

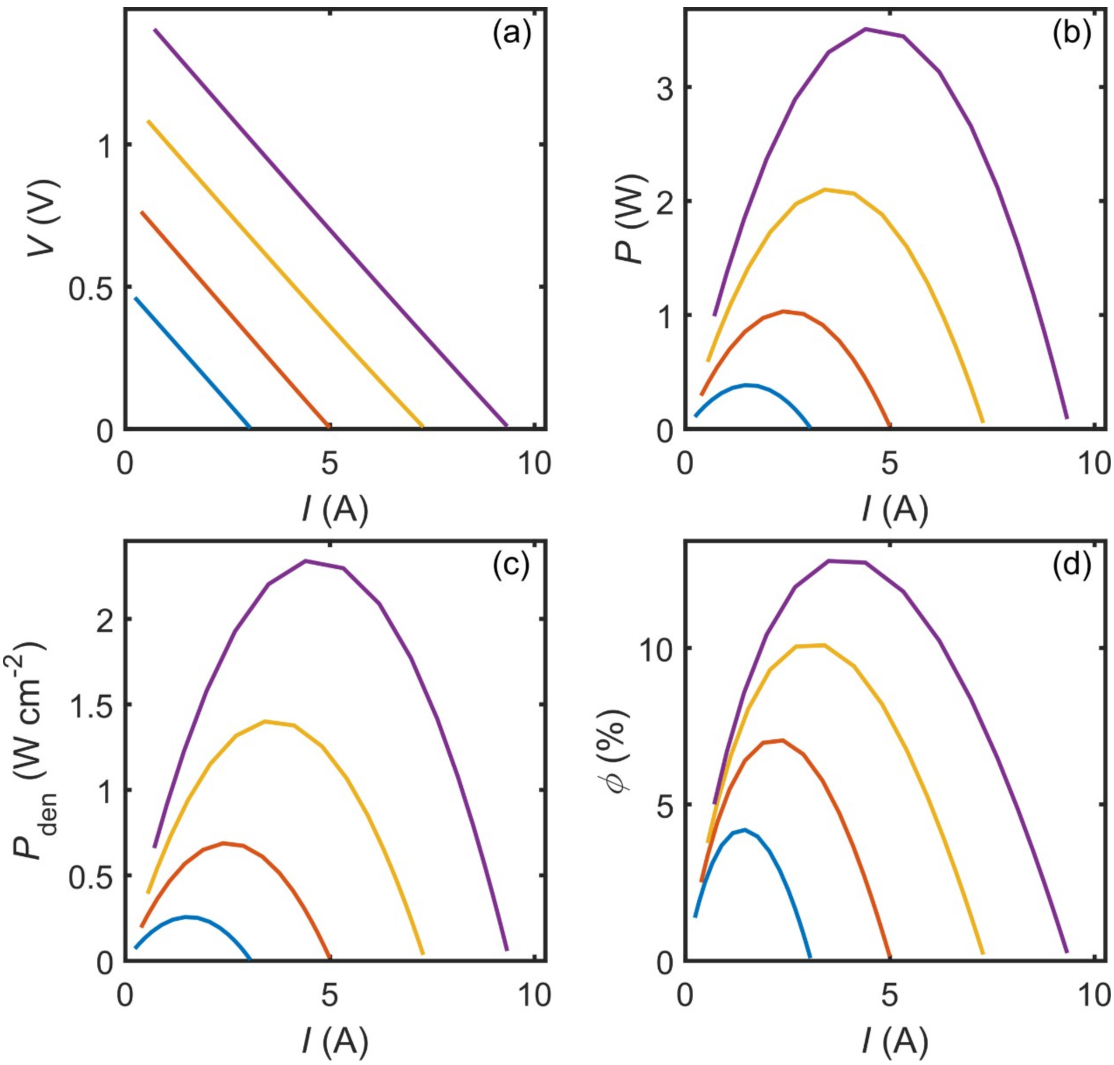

Fig. S62 Device simulation results of as-developed p-type $Ge_{0.89}Cr_{0.03}Sb_{0.08}Te$ and reported n-type Sb-doped $Mg_2Si_{0.3}Sn_{0.7}$.[63] Generated (a) voltage (V), (b) output electrical power (P), (c) output electrical power density (P_{den}), and (d) conversion efficiency (ϕ) of the module under cold side temperature of 300 K and hot side temperatures of 480, 580, 680, and 780 K.

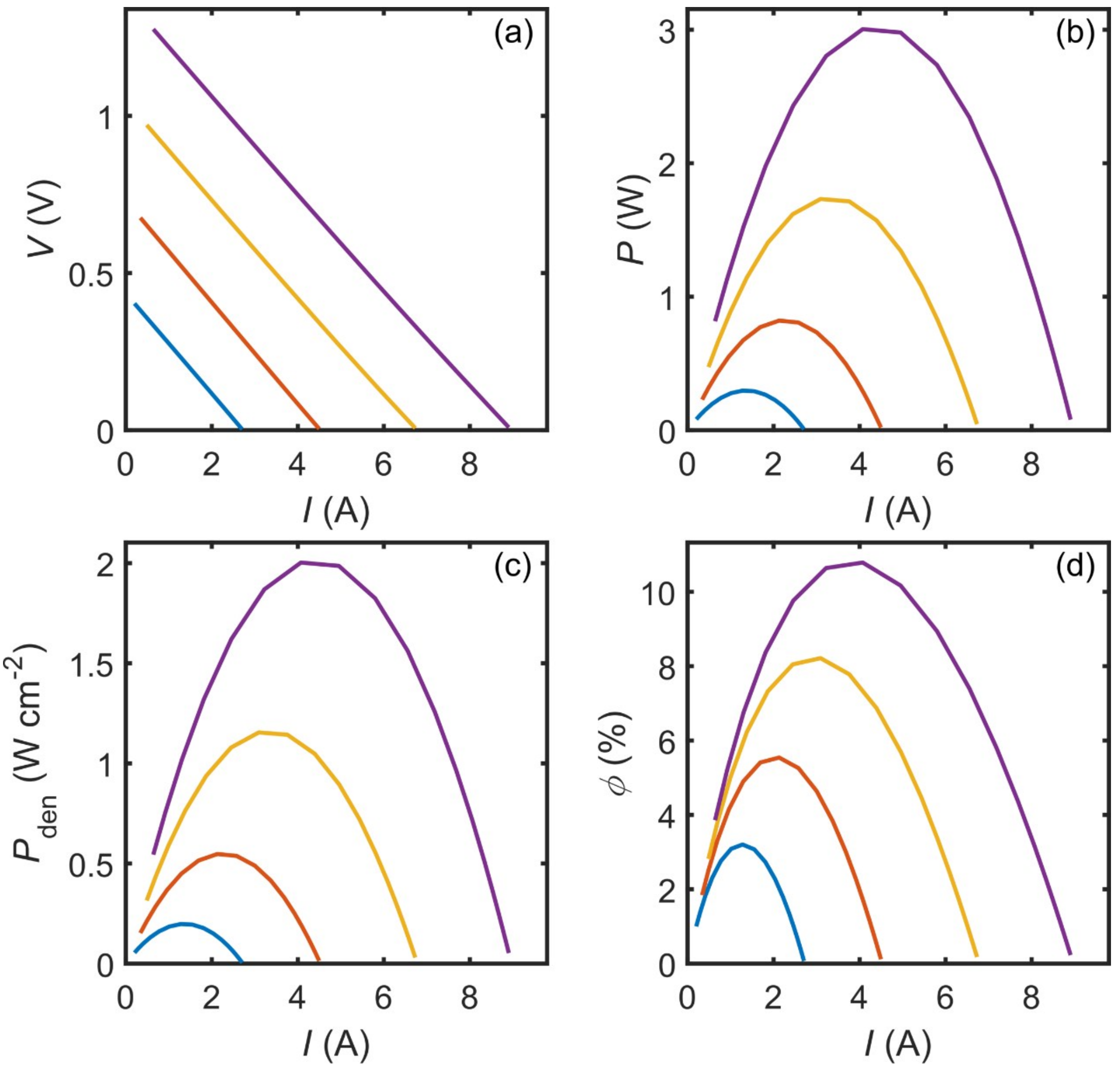

Fig. S63 Device simulation results of as-developed p-type $Ge_{0.89}Cr_{0.03}Sb_{0.08}Te$ and reported n-type Sb-doped $Mg_2Si_{0.4}Sn_{0.6}$.[64] Generated (a) voltage (V), (b) output electrical power (P), (c) output electrical power density (P_{den}), and (d) conversion efficiency (ϕ) of the module under cold side temperature of 300 K and hot side temperatures of 480, 580, 680, and 780 K.

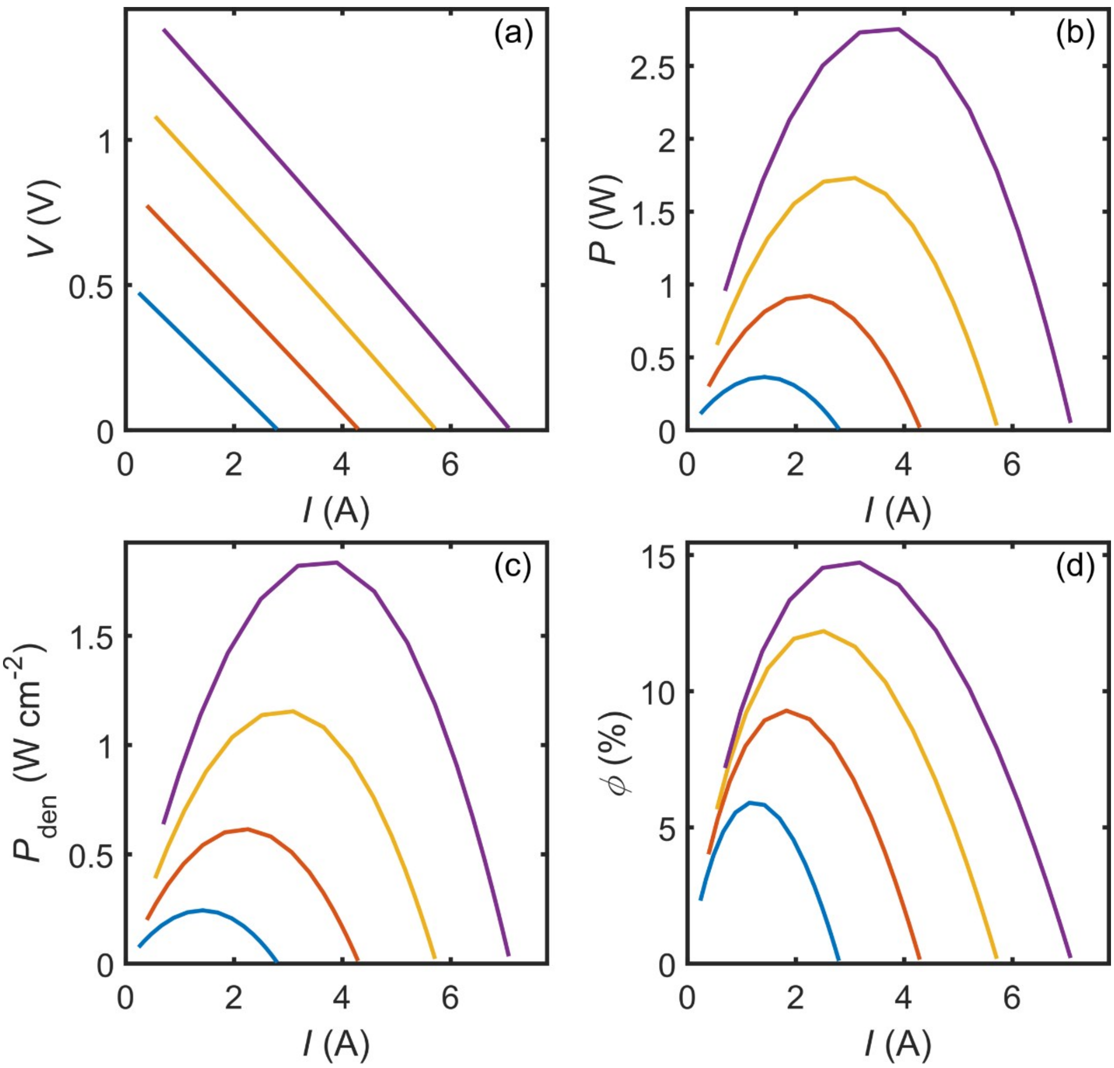

Fig. S64 Device simulation results of as-developed p-type $Ge_{0.89}Cr_{0.03}Sb_{0.08}Te$ and reported n-type $Mg_3Sb_{0.6}Bi_{1.4}$.[65] Generated (a) voltage (V), (b) output electrical power (P), (c) output electrical power density (P_{den}), and (d) conversion efficiency (ϕ) of the module under cold side temperature of 300 K and hot side temperatures of 480, 580, 680, and 780 K.

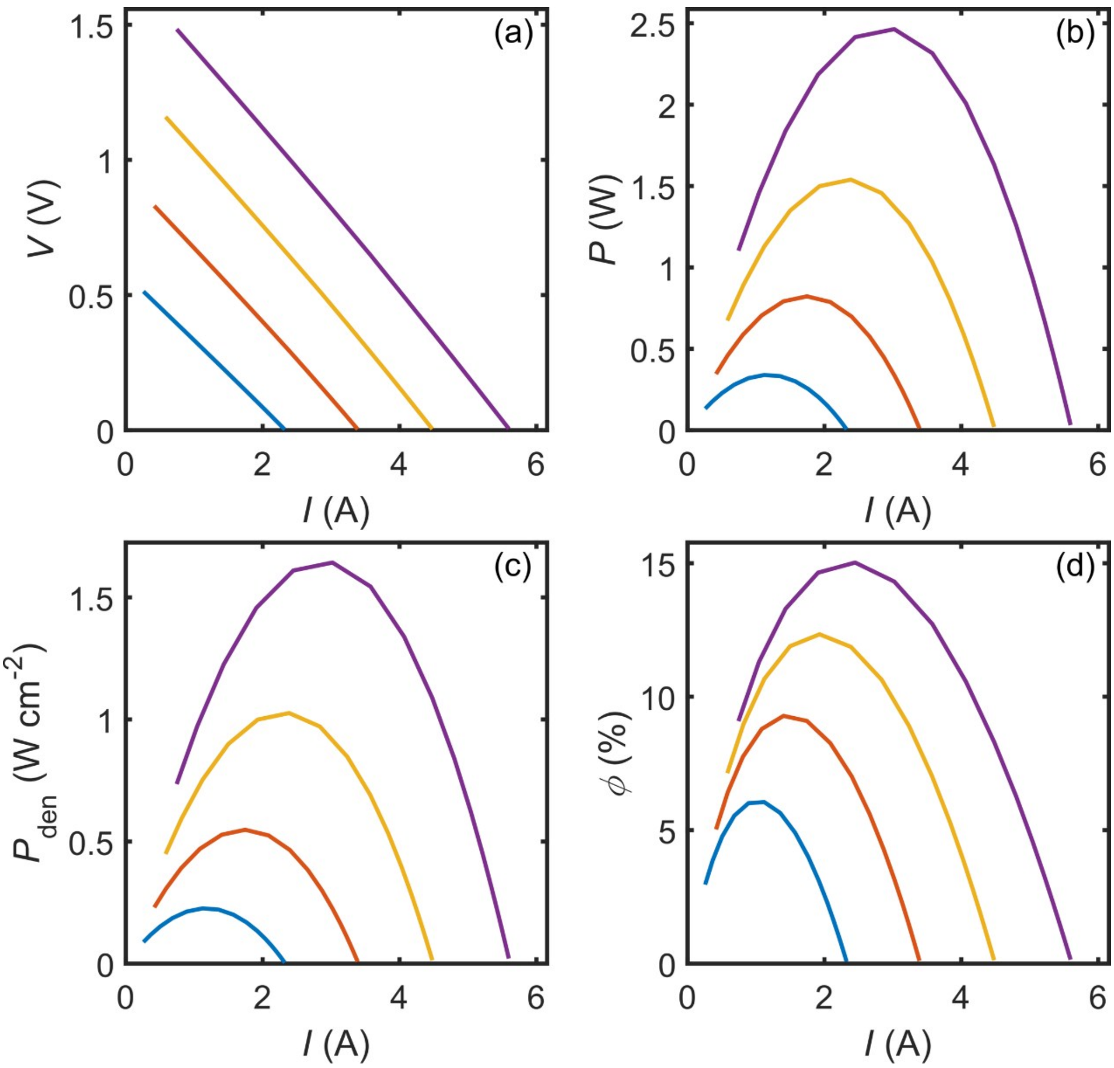

Fig. S65 Device simulation results of as-developed p-type $Ge_{0.89}Cr_{0.03}Sb_{0.08}Te$ and reported n-type $Mg_{3+\delta}Sb_{1.49}Bi_{0.5}$Te0.01.[66] Generated (a) voltage (V), (b) output electrical power (P), (c) output electrical power density (P_{den}), and (d) conversion efficiency (ϕ) of the module under cold side temperature of 300 K and hot side temperatures of 480, 580, 680, and 780 K.

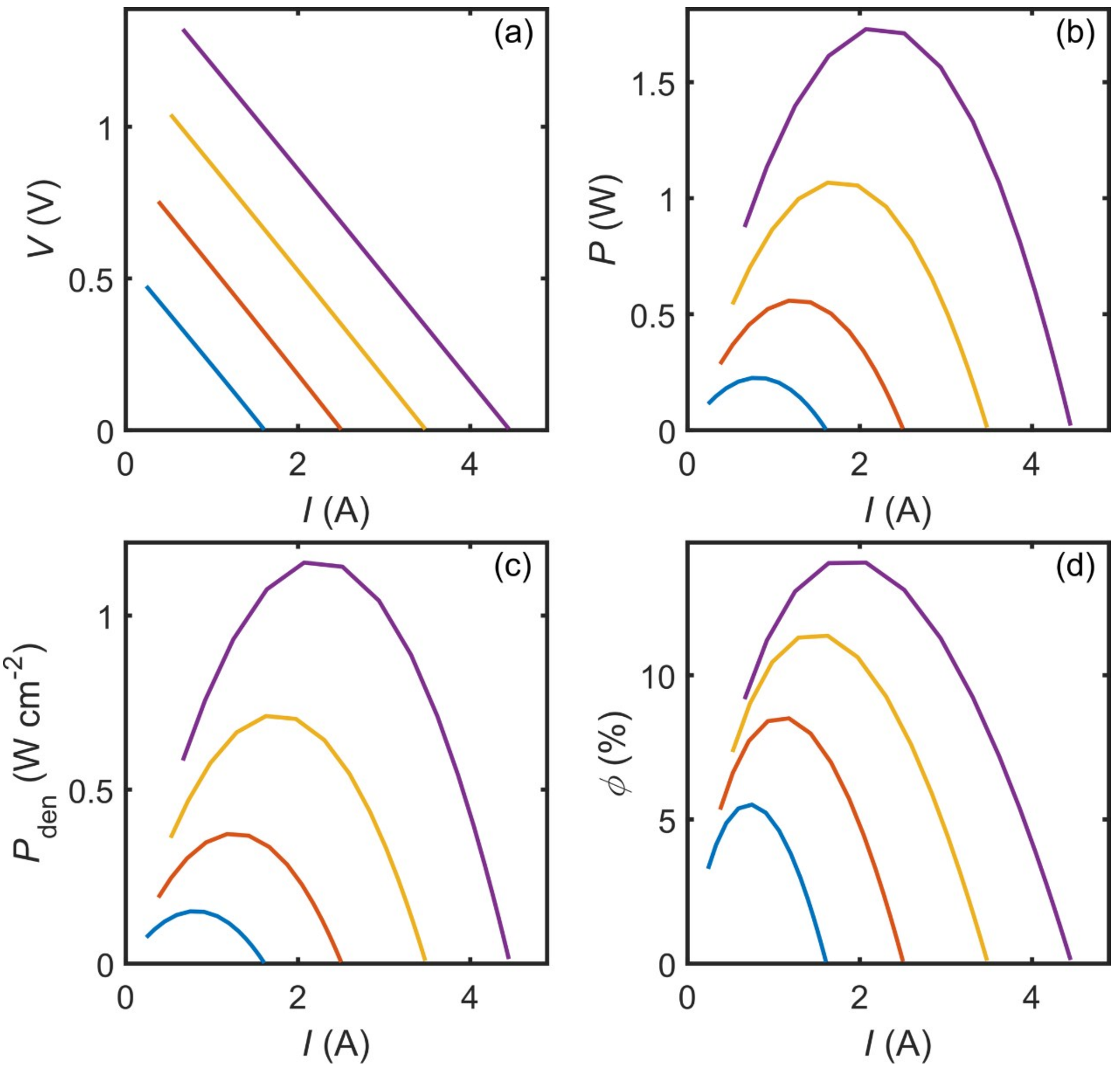

Fig. S66 Device simulation results of as-developed p-type $Ge_{0.89}Cr_{0.03}Sb_{0.08}Te$ and reported n-type Bi_2Te_3.[67] Generated (a) voltage (V), (b) output electrical power (P), (c) output electrical power density (P_{den}), and (d) conversion efficiency (ϕ) of the module under cold side temperature of 300 K and hot side temperatures of 480, 580, 680, and 780 K.

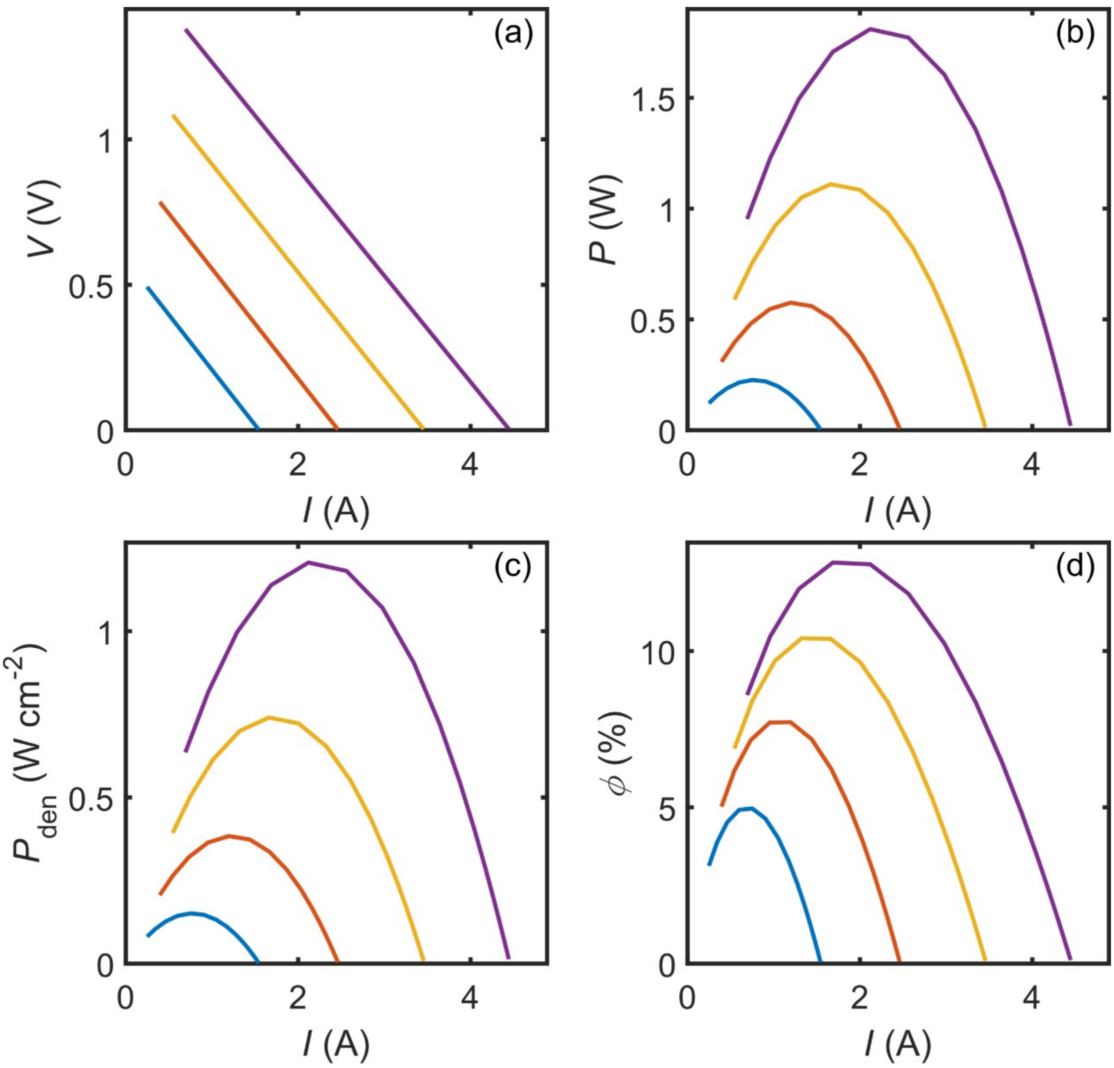

Fig. S67 Device simulation results of as-developed p-type $Ge_{0.89}Cr_{0.03}Sb_{0.08}Te$ and reported n-type $(Bi_2Te_3)_{0.85}(Bi_2Se_3)_{0.15}$.[68] Generated (a) voltage (V), (b) output electrical power (P), (c) output electrical power density (P_{den}), and (d) conversion efficiency (ϕ) of the module under cold side temperature of 300 K and hot side temperatures of 480, 580, 680, and 780 K.

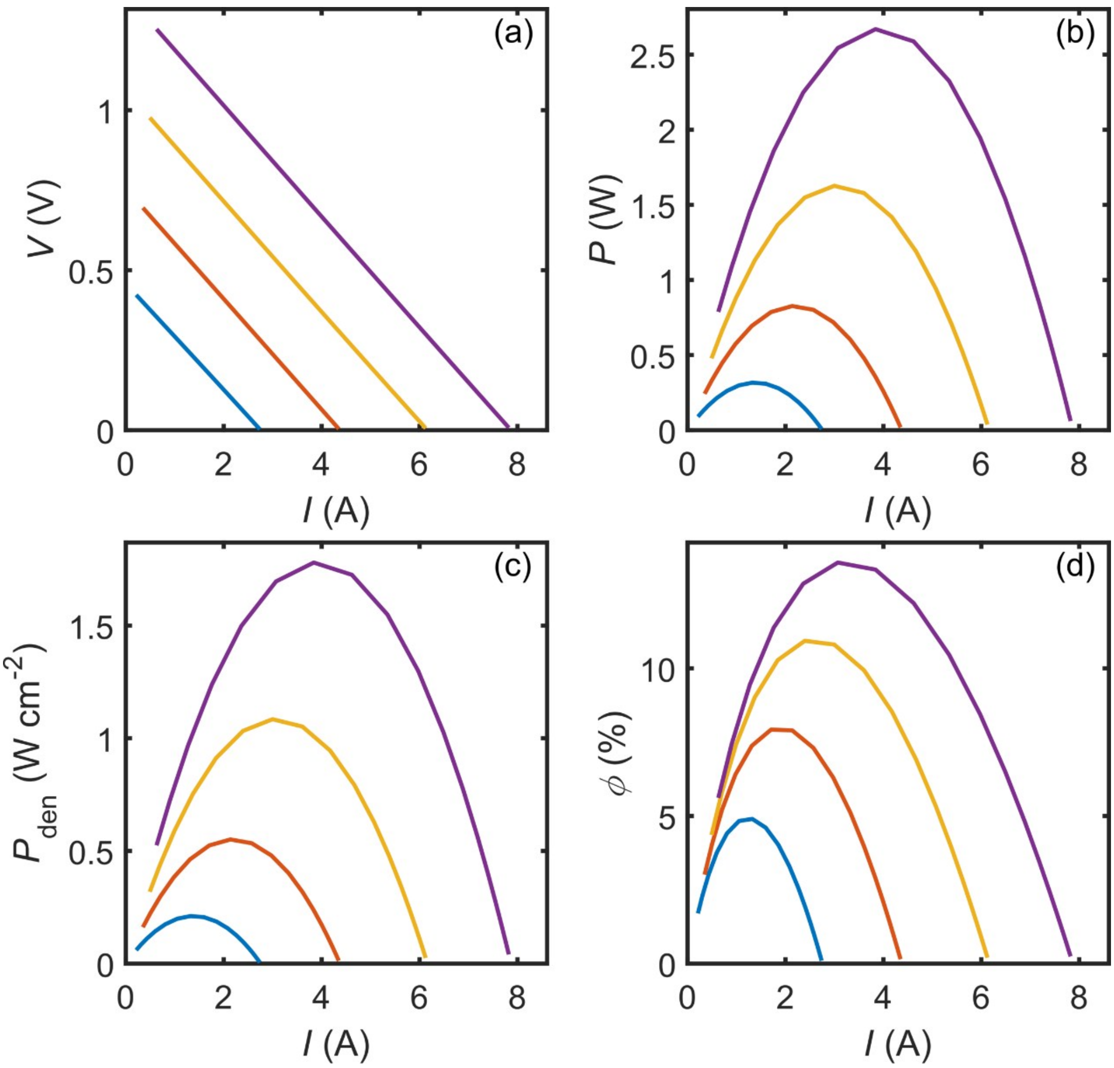

Fig. S68 Device simulation results of as-developed p-type $Ge_{0.89}Cr_{0.03}Sb_{0.08}Te$ and reported n-type $Bi_2(Te_{1-x}Se_x)_3$-I(0.08%).[69] Generated (a) voltage (V), (b) output electrical power (P), (c) output electrical power density (P_{den}), and (d) conversion efficiency (ϕ) of the module under cold side temperature of 300 K and hot side temperatures of 480, 580, 680, and 780 K.

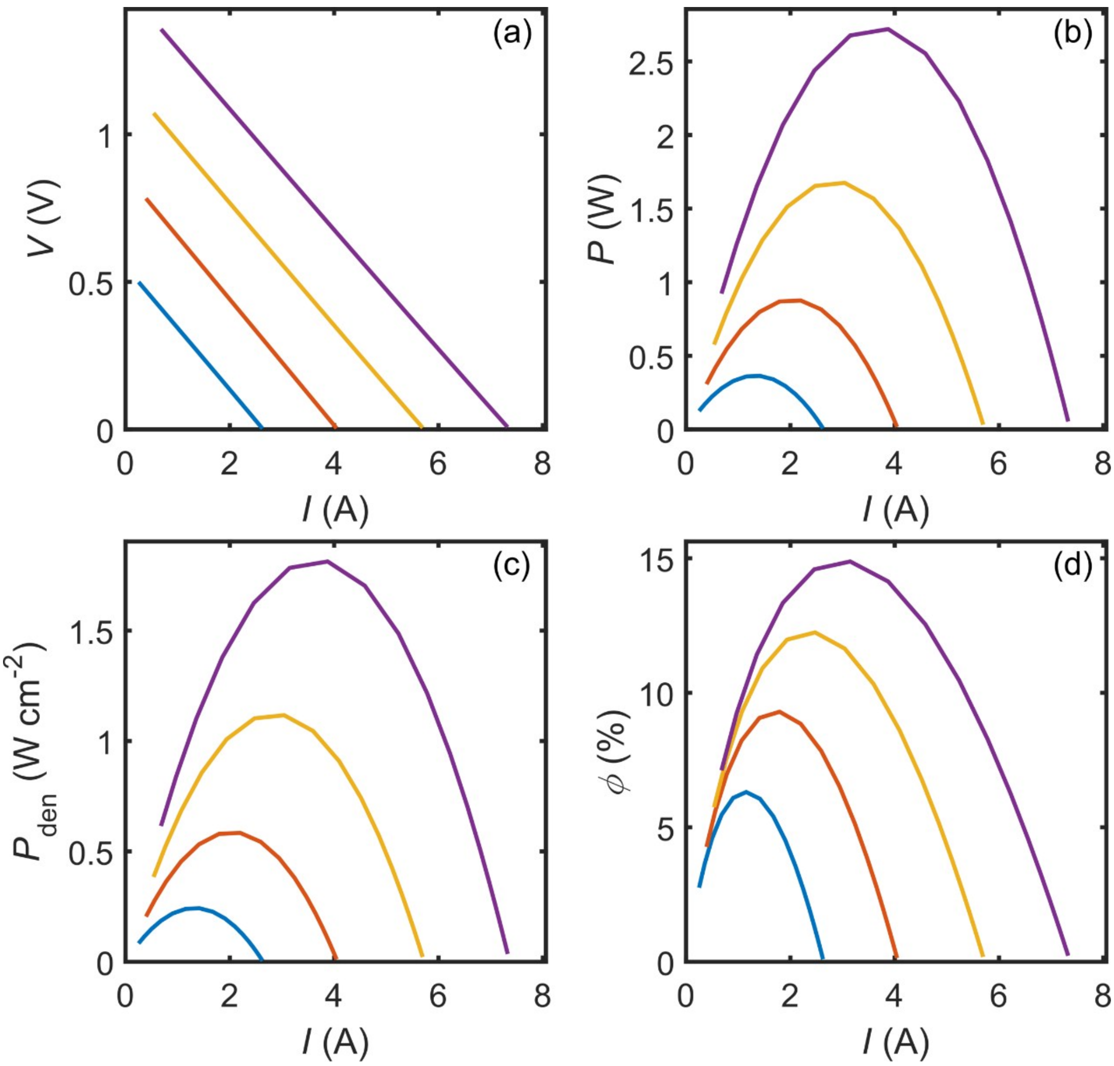

Fig. S69 Device simulation results of as-developed p-type $Ge_{0.89}Cr_{0.03}Sb_{0.08}Te$ and reported n-type $Cu_{0.01}Bi_2Te_{2.7}Se_{0.3}$.[70] Generated (a) voltage (V), (b) output electrical power (P), (c) output electrical power density (P_{den}), and (d) conversion efficiency (ϕ) of the module under cold side temperature of 300 K and hot side temperatures of 480, 580, 680, and 780 K.

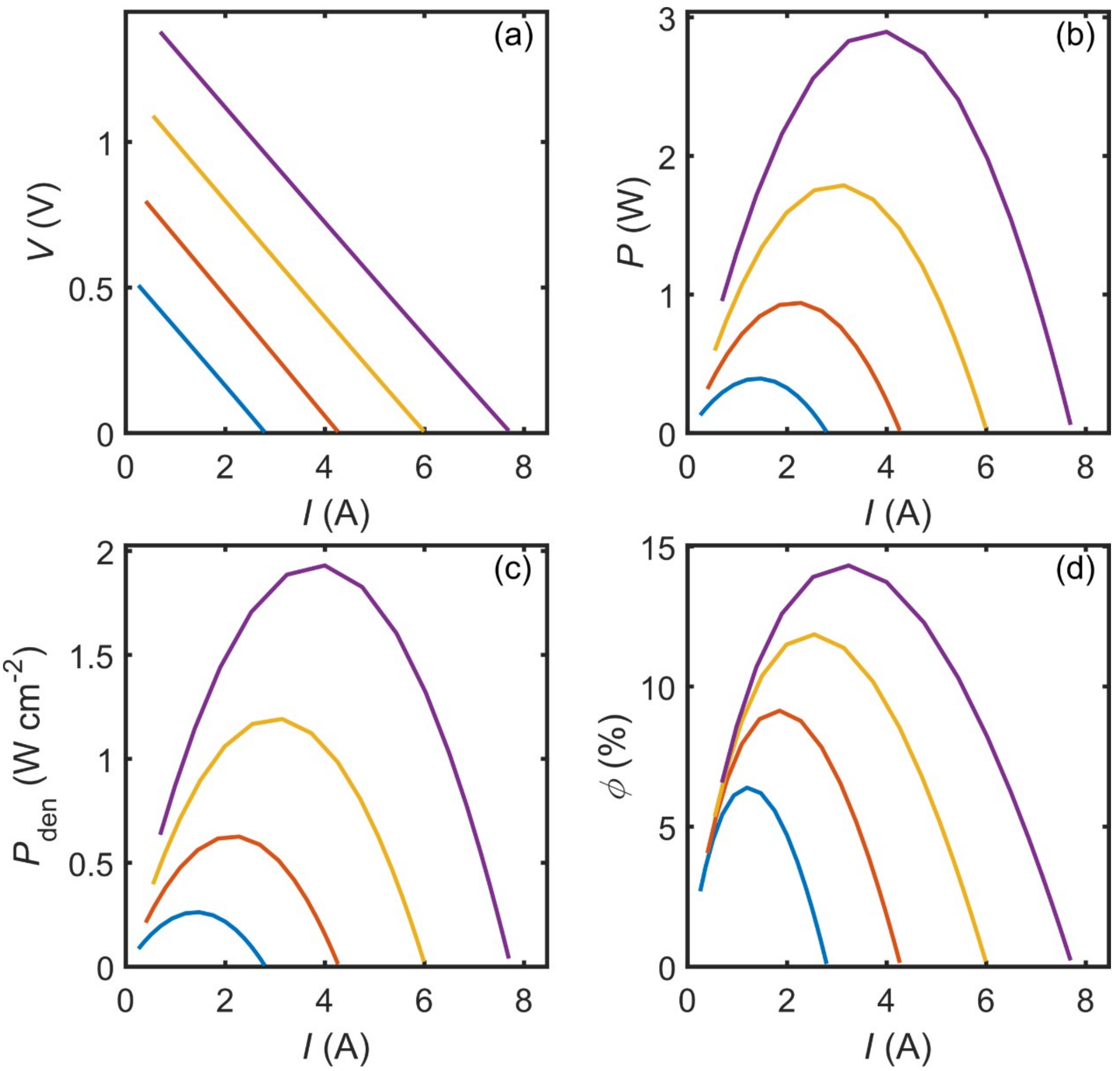

Fig. S70 Device simulation results of as-developed p-type $Ge_{0.89}Cr_{0.03}Sb_{0.08}Te$ and reported n-type $Bi_2Te_{2.79}Se_{0.21}$.[14] Generated (a) voltage (V), (b) output electrical power (P), (c) output electrical power density (P_{den}), and (d) conversion efficiency (ϕ) of the module under cold side temperature of 300 K and hot side temperatures of 480, 580, 680, and 780 K.

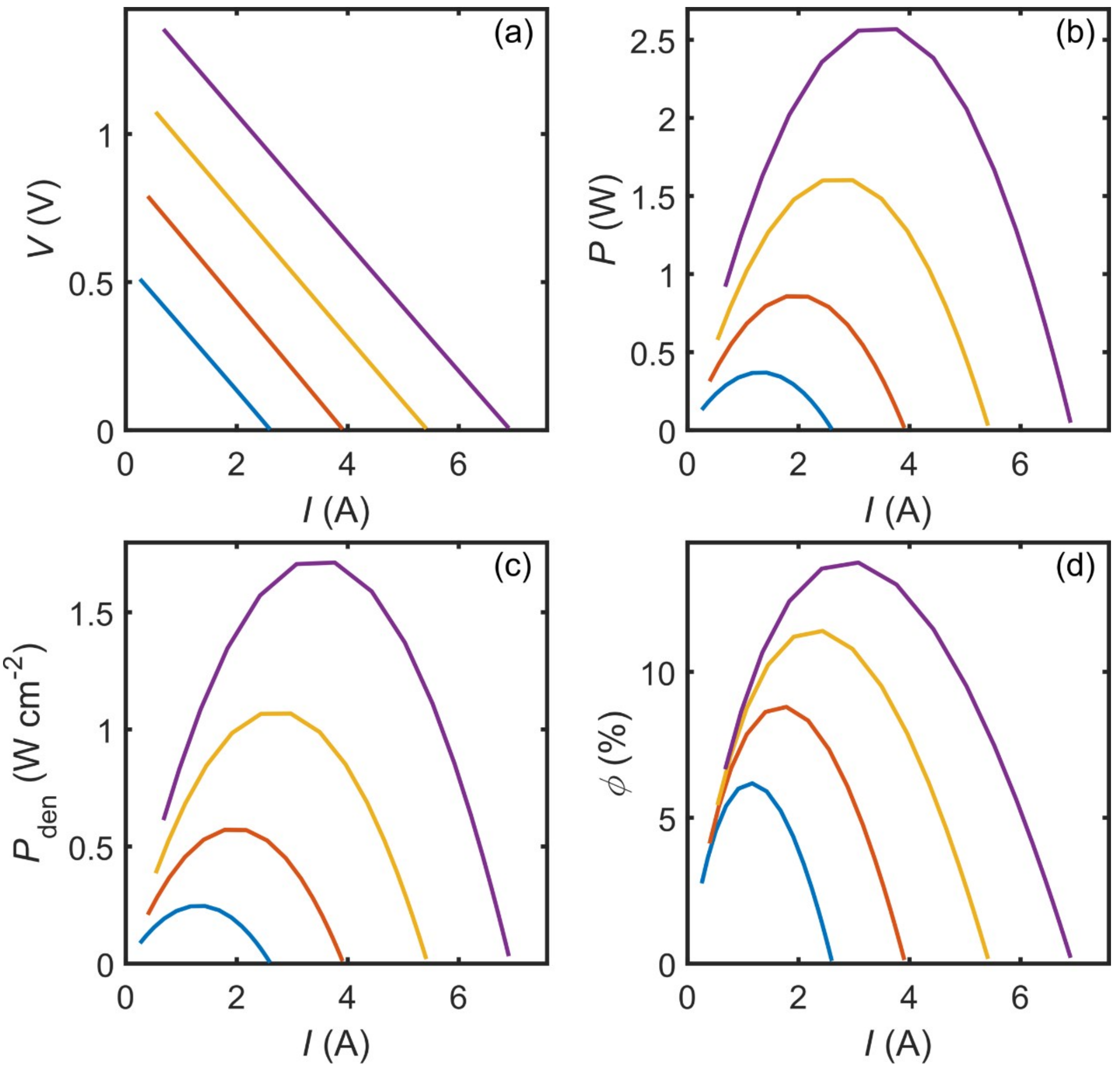

Fig. S71 Device simulation results of as-developed p-type $Ge_{0.89}Cr_{0.03}Sb_{0.08}Te$ and reported n-type $Bi_2Te_{2.7}Se_{0.3}$.[71] Generated (a) voltage (V), (b) output electrical power (P), (c) output electrical power density (P_{den}), and (d) conversion efficiency (ϕ) of the module under cold side temperature of 300 K and hot side temperatures of 480, 580, 680, and 780 K.

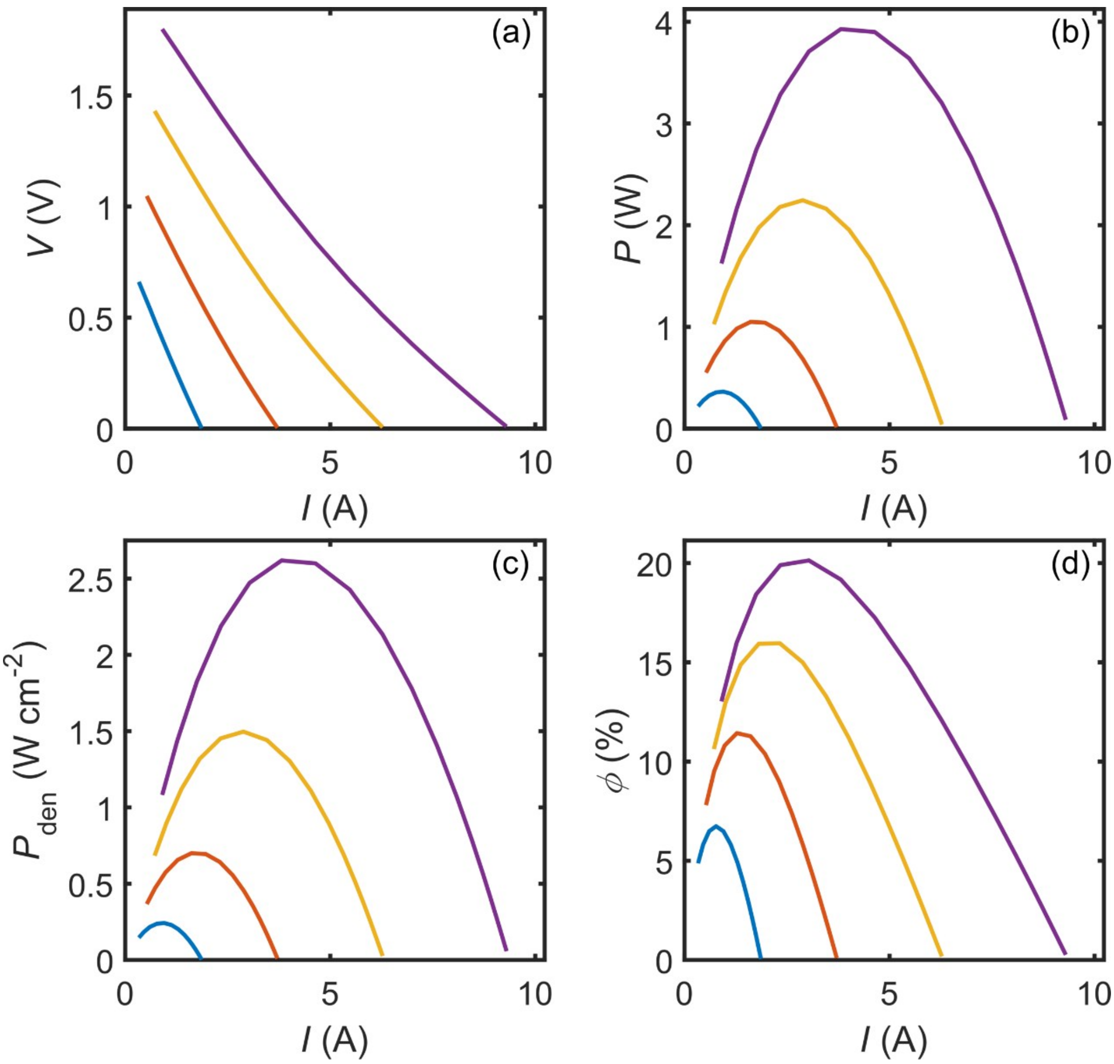

Fig. S72 Device simulation results of as-developed p-type $Ge_{0.89}Cr_{0.03}Sb_{0.08}Te$ and reported n-type $AgIn_5Se_8$.[72] Generated (a) voltage (V), (b) output electrical power (P), (c) output electrical power density (P_{den}), and (d) conversion efficiency (ϕ) of the module under cold side temperature of 300 K and hot side temperatures of 480, 580, 680, and 780 K.

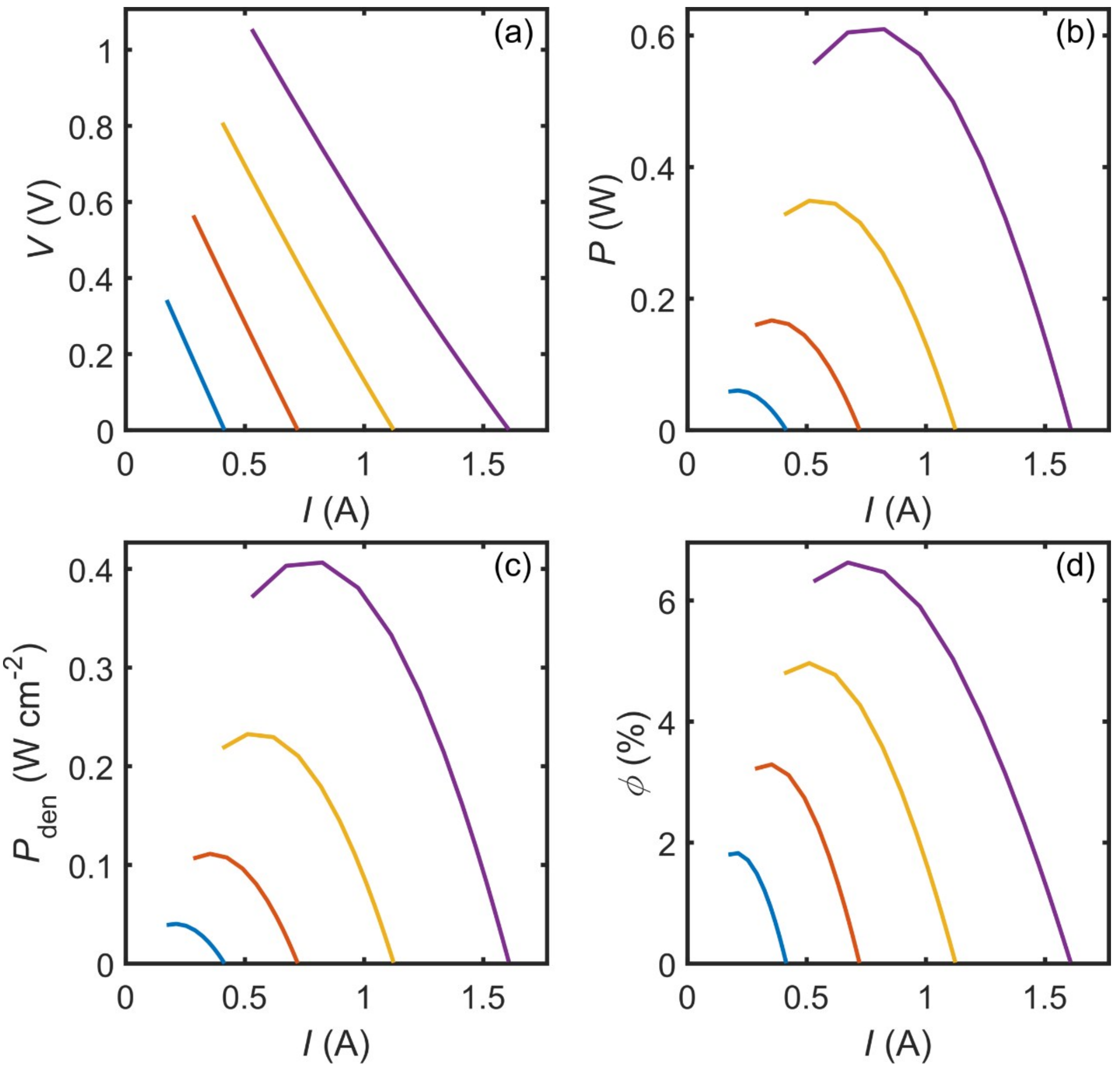

Fig. S73 Device simulation results of as-developed p-type $Ge_{0.89}Cr_{0.03}Sb_{0.08}Te$ and reported n-type $Ag_{0.9}InZn_{0.1}Se_2$.[73] Generated (a) voltage (V), (b) output electrical power (P), (c) output electrical power density (P_{den}), and (d) conversion efficiency (ϕ) of the module under cold side temperature of 300 K and hot side temperatures of 480, 580, 680, and 780 K.

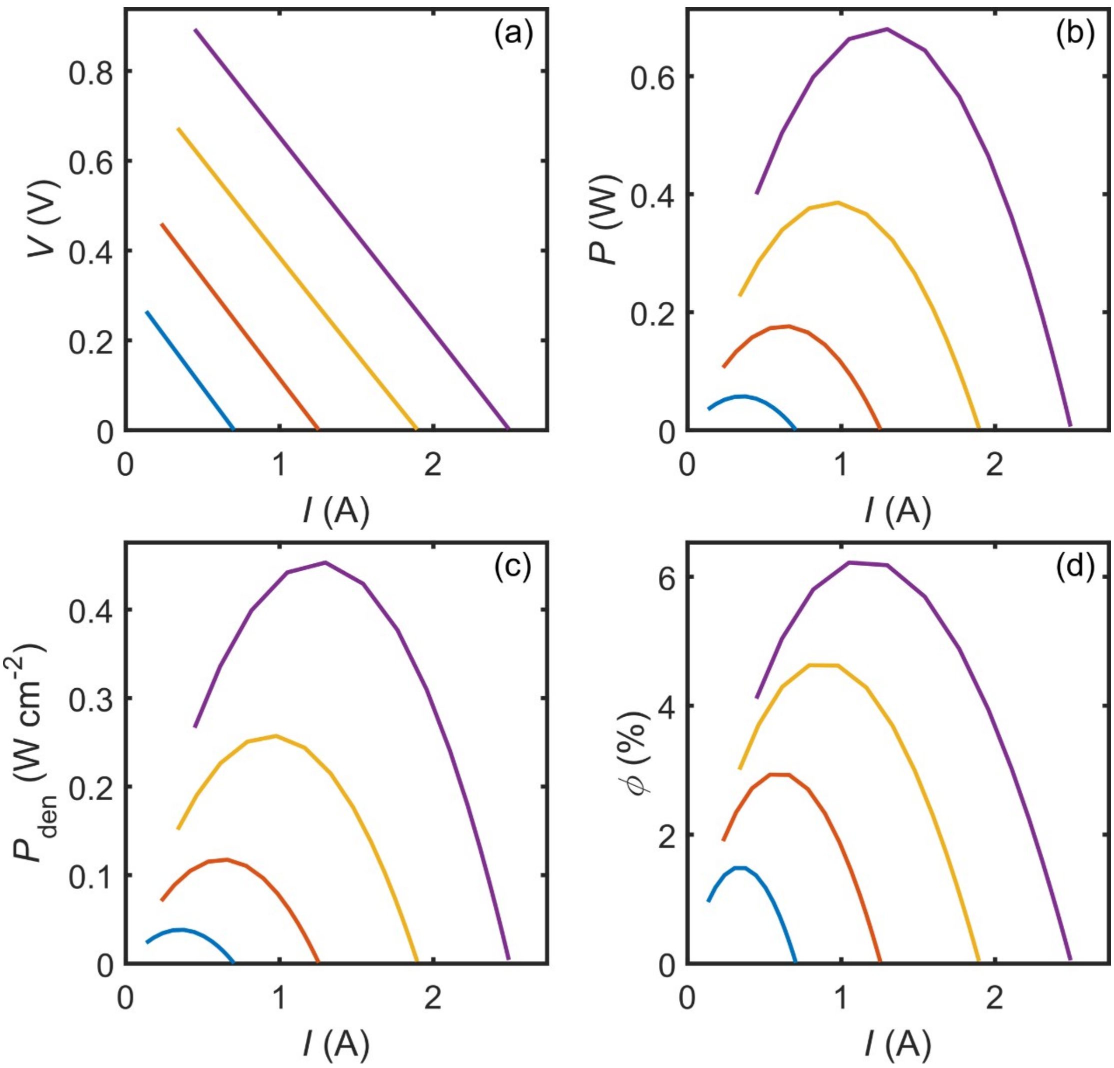

Fig. S74 Device simulation results of as-developed p-type $Ge_{0.89}Cr_{0.03}Sb_{0.08}Te$ and reported n-type $Ag_{0.96}Nb_{0.04}BiSe_2$.[74] Generated (a) voltage (V), (b) output electrical power (P), (c) output electrical power density (P_{den}), and (d) conversion efficiency (ϕ) of the module under cold side temperature of 300 K and hot side temperatures of 480, 580, 680, and 780 K.

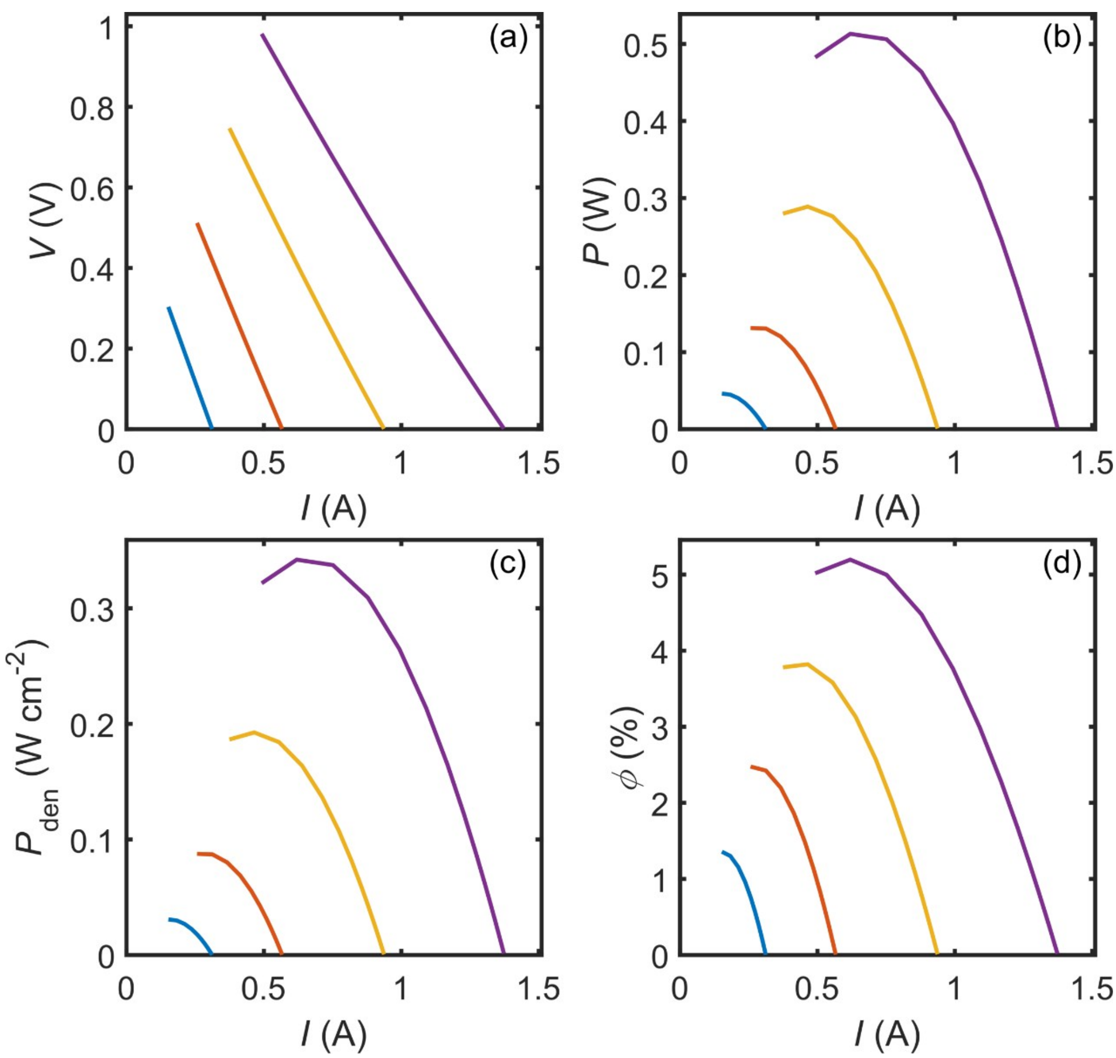

Fig. S75 Device simulation results of as-developed p-type $Ge_{0.89}Cr_{0.03}Sb_{0.08}Te$ and reported n-type $(GeSe)_{0.5}(AgBiSe_2)_{0.5}$.[75] Generated (a) voltage (V), (b) output electrical power (P), (c) output electrical power density (P_{den}), and (d) conversion efficiency (ϕ) of the module under cold side temperature of 300 K and hot side temperatures of 480, 580, 680, and 780 K.

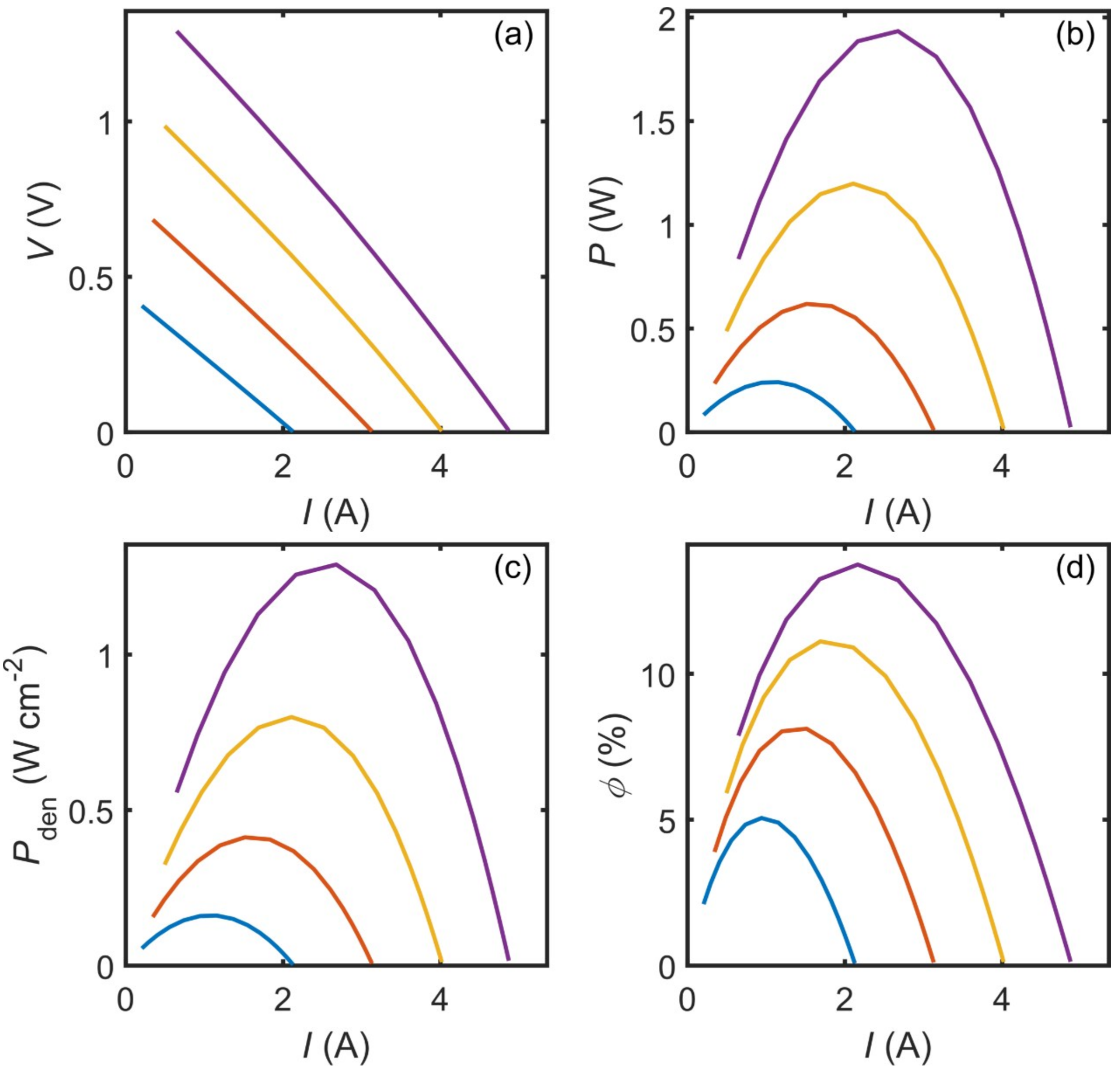

Fig. S76 Device simulation results of as-developed p-type $Ge_{0.89}Cr_{0.03}Sb_{0.08}Te$ and reported n-type $In_4Se_{2.35}$.[76] Generated (a) voltage (V), (b) output electrical power (P), (c) output electrical power density (P_{den}), and (d) conversion efficiency (ϕ) of the module under cold side temperature of 300 K and hot side temperatures of 480, 580, 680, and 780 K.

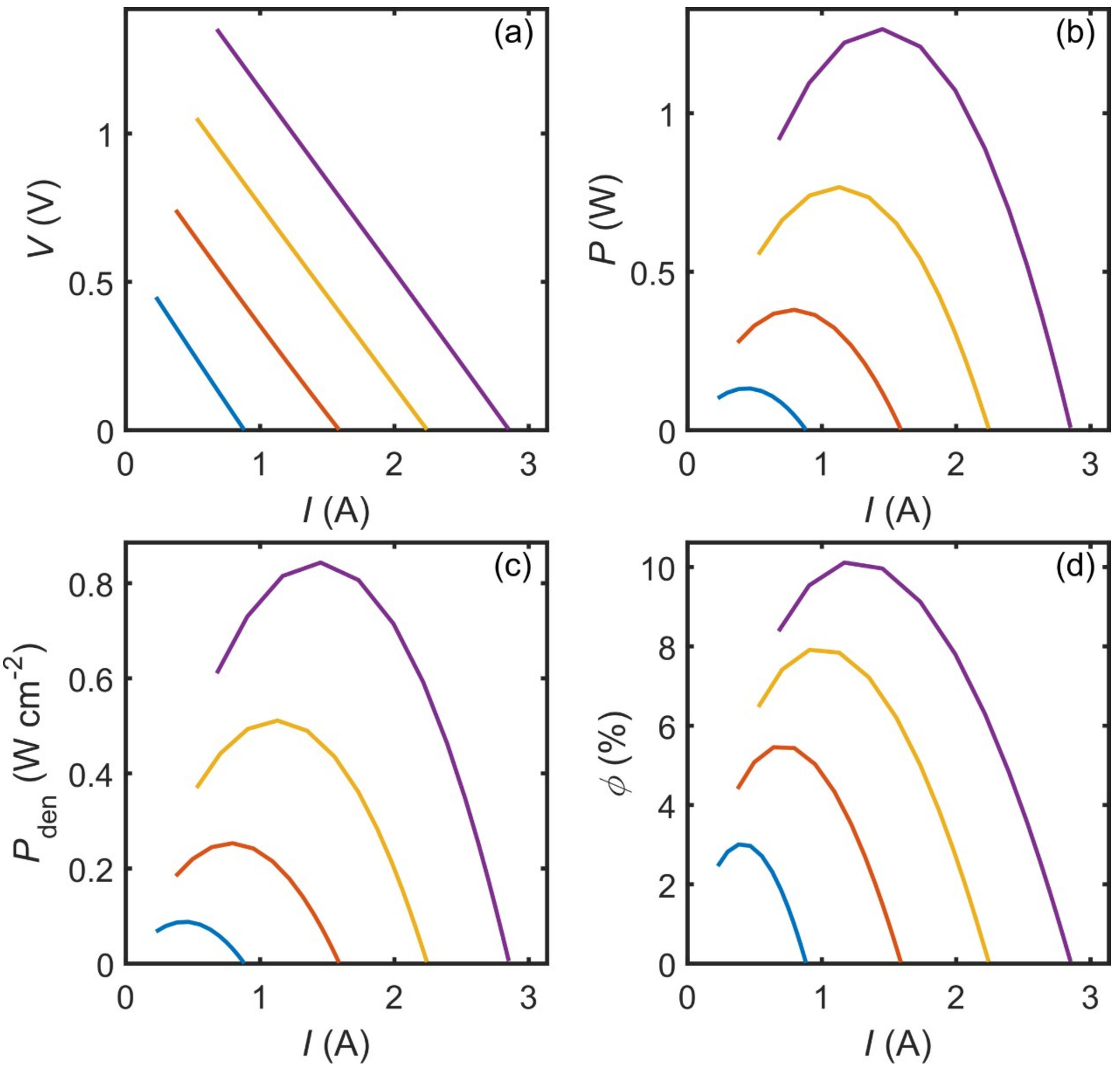

Fig. S77 Device simulation results of as-developed p-type $Ge_{0.89}Cr_{0.03}Sb_{0.08}Te$ and reported n-type $K_{0.95}Pb_{20}Sb_{1.2}Te_{22}$.[77] Generated (a) voltage (V), (b) output electrical power (P), (c) output electrical power density (P_{den}), and (d) conversion efficiency (ϕ) of the module under cold side temperature of 300 K and hot side temperatures of 480, 580, 680, and 780 K.

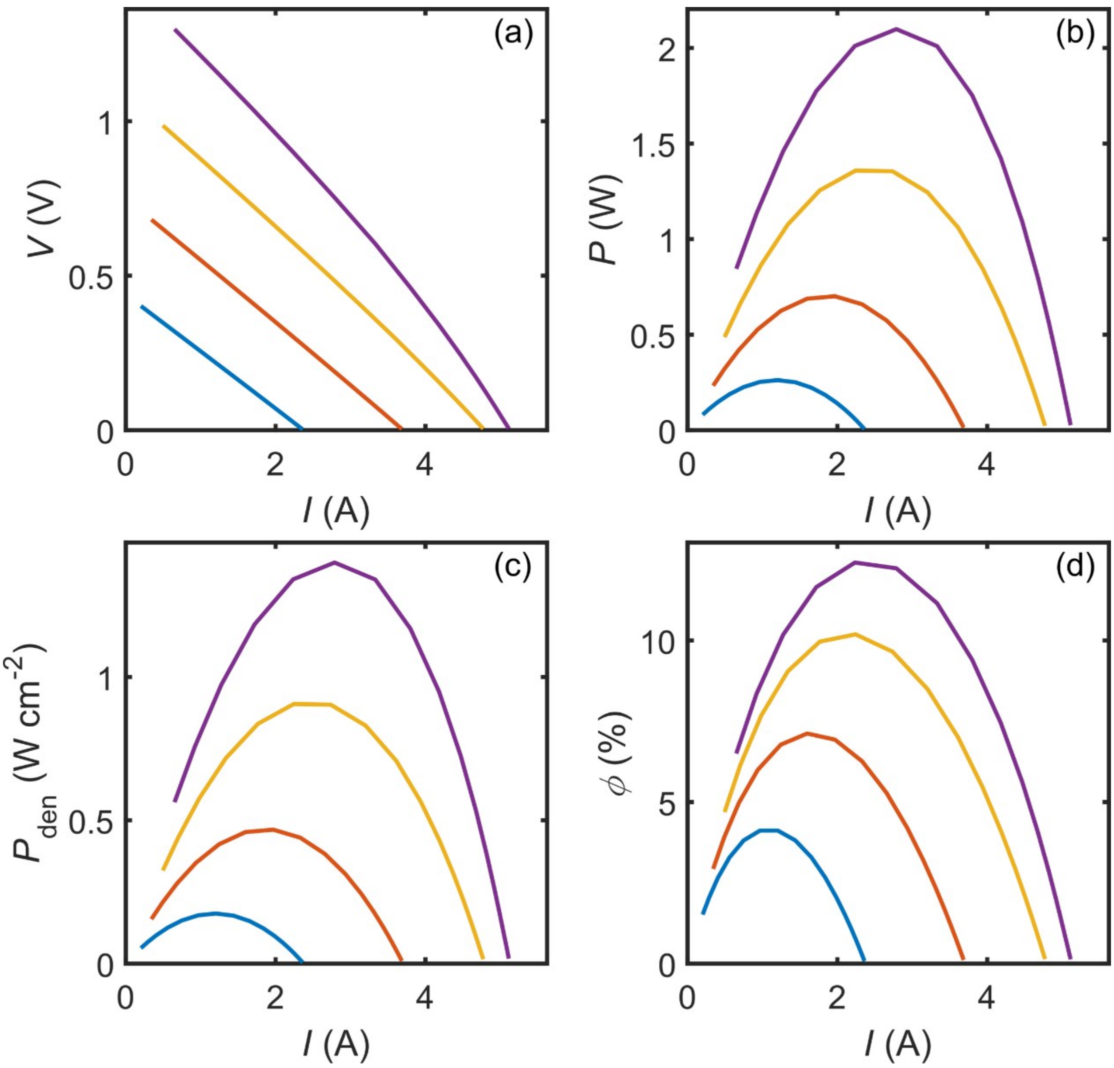

Fig. S78 Device simulation results of as-developed p-type $Ge_{0.89}Cr_{0.03}Sb_{0.08}Te$ and reported n-type $Ag_{0.4}Pb_{22.5}SbTe_{20}$.[78] Generated (a) voltage (V), (b) output electrical power (P), (c) output electrical power density (P_{den}), and (d) conversion efficiency (ϕ) of the module under cold side temperature of 300 K and hot side temperatures of 480, 580, 680, and 780 K.

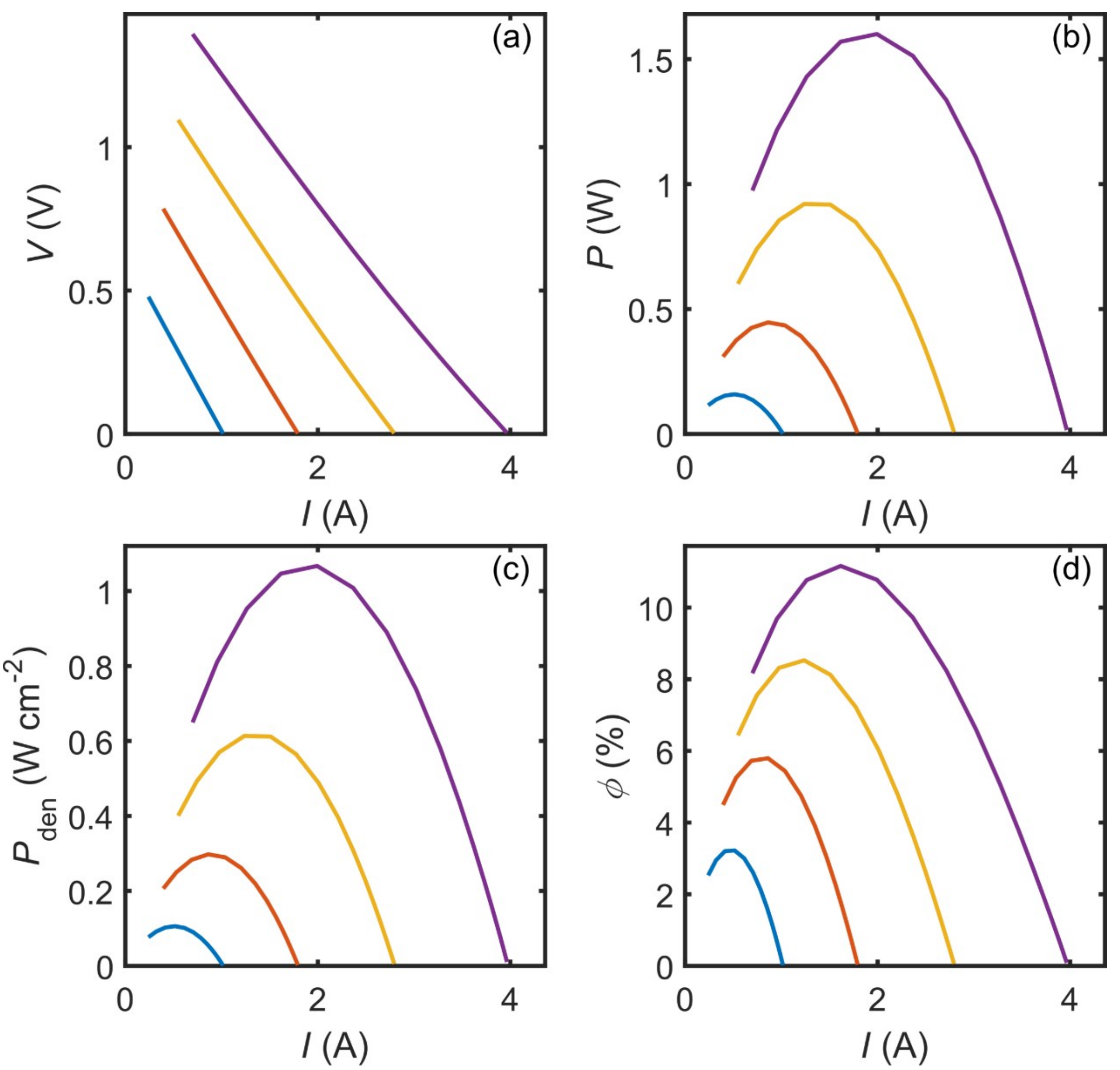

Fig. S79 Device simulation results of as-developed p-type $Ge_{0.89}Cr_{0.03}Sb_{0.08}Te$ and reported n-type $AgPb_{20}SbTe_{20}$.[79] Generated (a) voltage (V), (b) output electrical power (P), (c) output electrical power density (P_{den}), and (d) conversion efficiency (ϕ) of the module under cold side temperature of 300 K and hot side temperatures of 480, 580, 680, and 780 K.

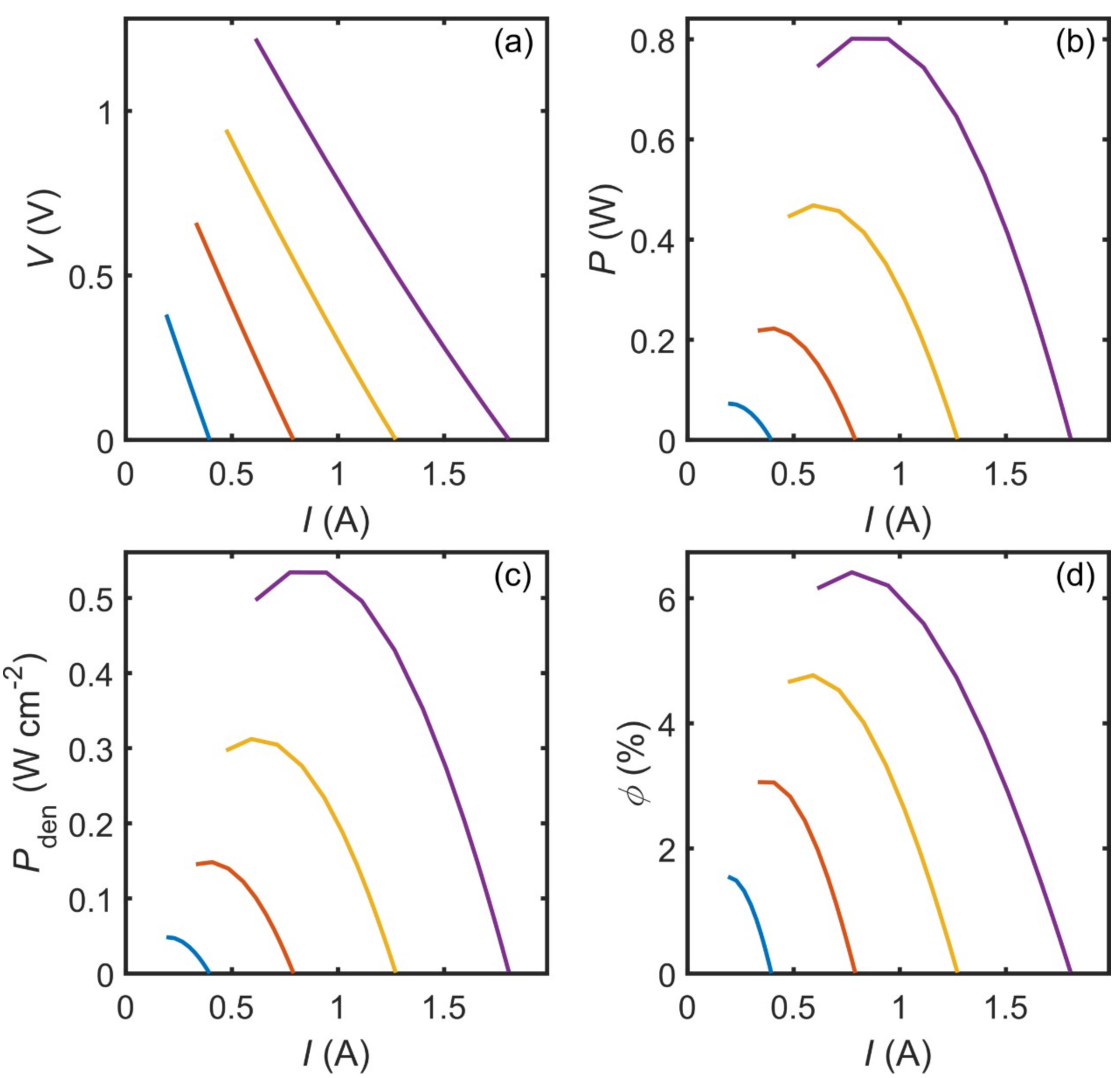

Fig. S80 Device simulation results of as-developed p-type $Ge_{0.89}Cr_{0.03}Sb_{0.08}Te$ and reported n-type $AgPb_{18}SbSe_{19.928}Cl_{0.072}$.[80] Generated (a) voltage (V), (b) output electrical power (P), (c) output electrical power density (P_{den}), and (d) conversion efficiency (ϕ) of the module under cold side temperature of 300 K and hot side temperatures of 480, 580, 680, and 780 K.

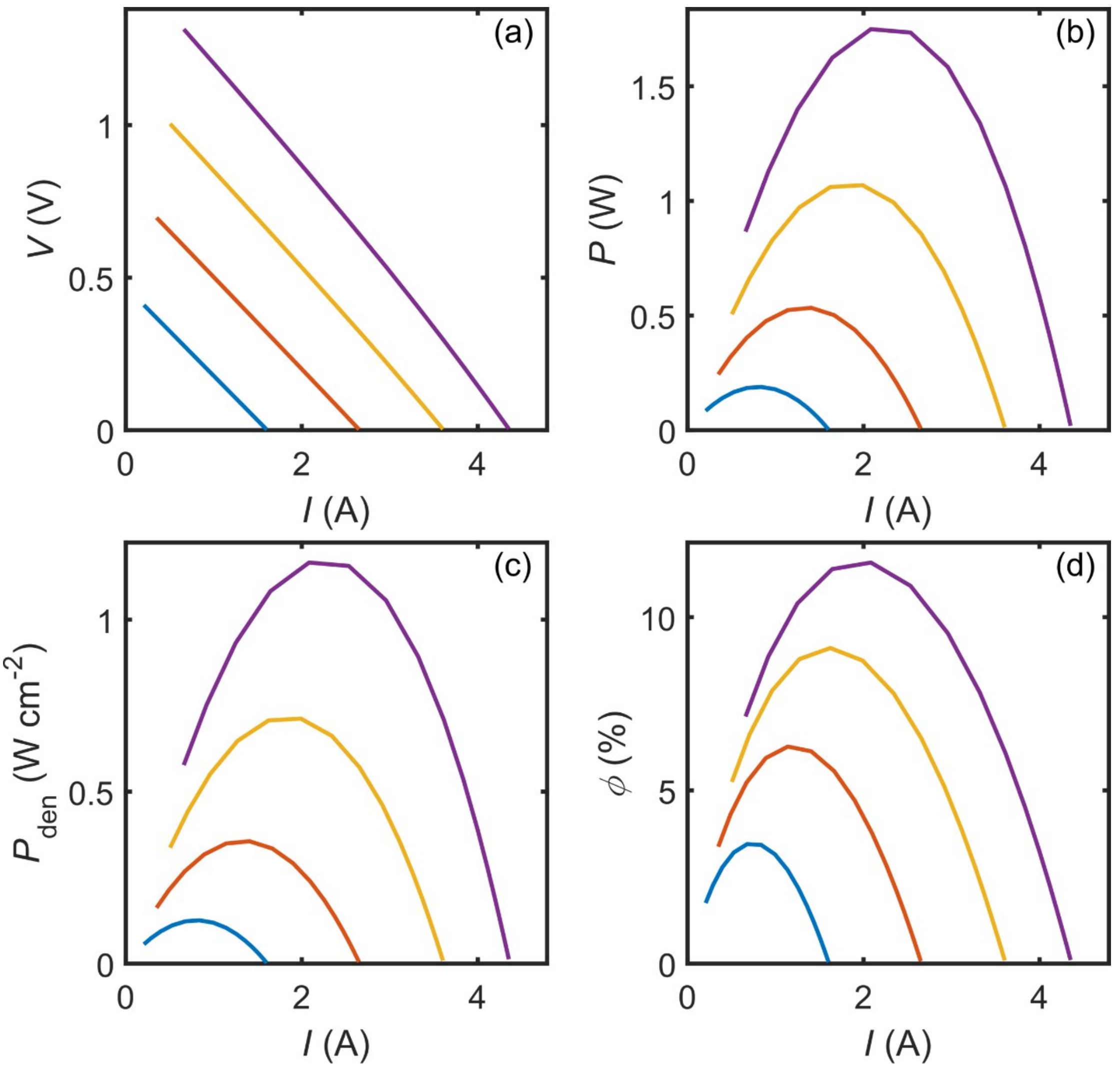

Fig. S81 Device simulation results of as-developed p-type $Ge_{0.89}Cr_{0.03}Sb_{0.08}Te$ and reported n-type $AgPb_{22.5}SbTe_{20}$.[81] Generated (a) voltage (V), (b) output electrical power (P), (c) output electrical power density (P_{den}), and (d) conversion efficiency (ϕ) of the module under cold side temperature of 300 K and hot side temperatures of 480, 580, 680, and 780 K.

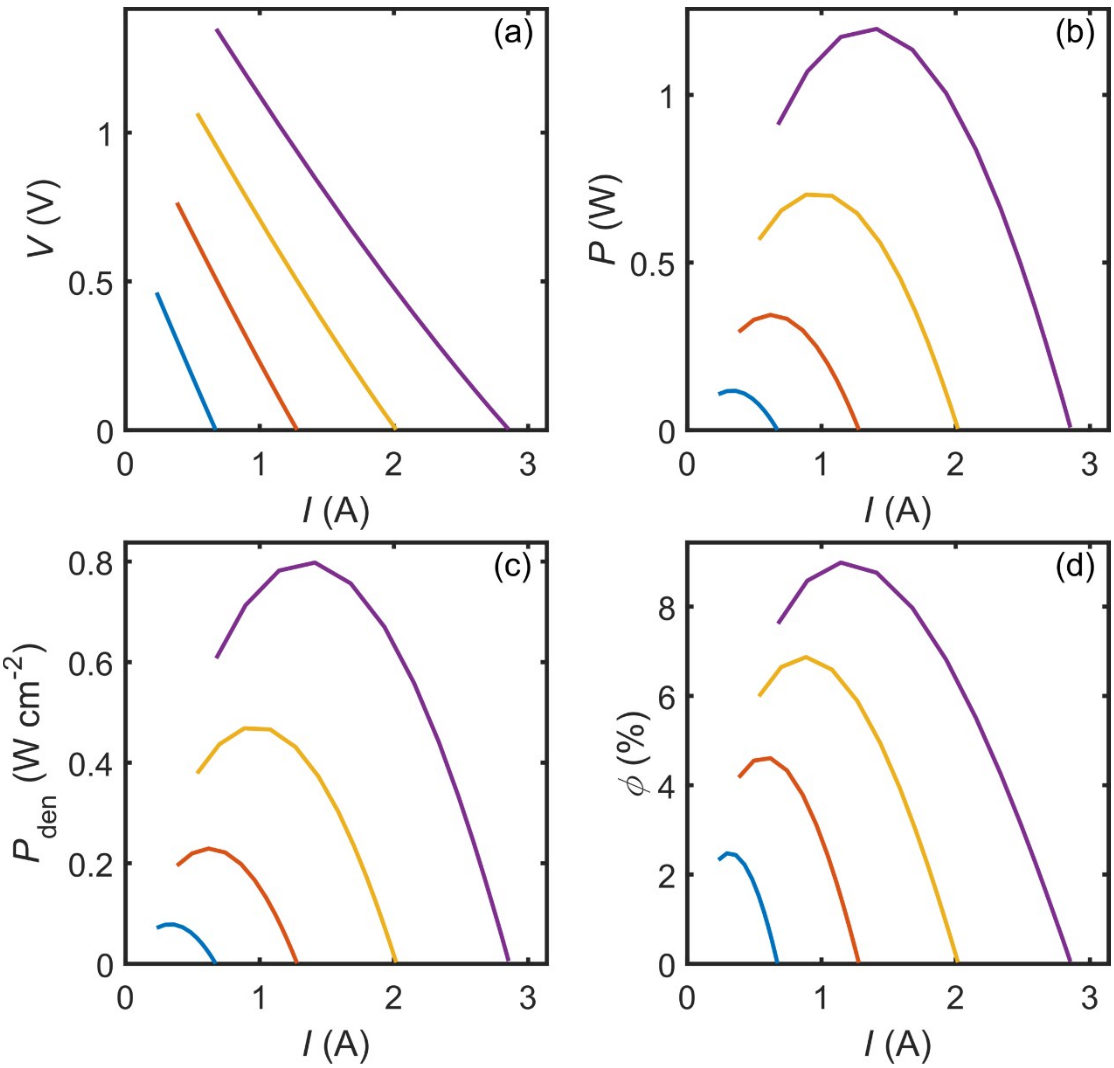

Fig. S82 Device simulation results of as-developed p-type $Ge_{0.89}Cr_{0.03}Sb_{0.08}Te$ and reported n-type Ge-doped $AgBiSe_2$.[82] Generated (a) voltage (V), (b) output electrical power (P), (c) output electrical power density (P_{den}), and (d) conversion efficiency (ϕ) of the module under cold side temperature of 300 K and hot side temperatures of 480, 580, 680, and 780 K.

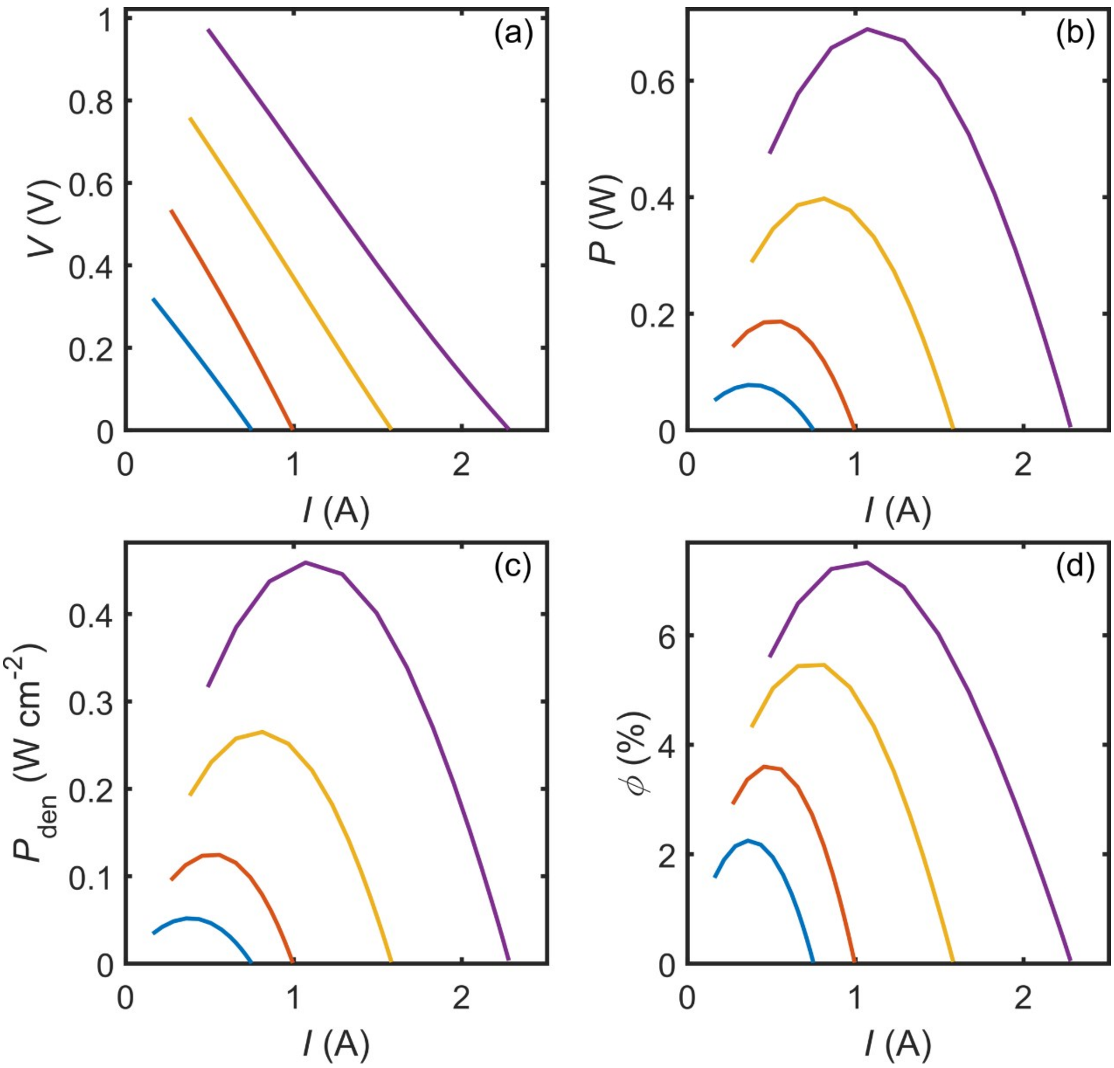

Fig. S83 Device simulation results of as-developed p-type $Ge_{0.89}Cr_{0.03}Sb_{0.08}Te$ and reported n-type $Ag_2Se_{0.5}Te_{0.5}$.[83] Generated (a) voltage (V), (b) output electrical power (P), (c) output electrical power density (P_{den}), and (d) conversion efficiency (ϕ) of the module under cold side temperature of 300 K and hot side temperatures of 480, 580, 680, and 780 K.

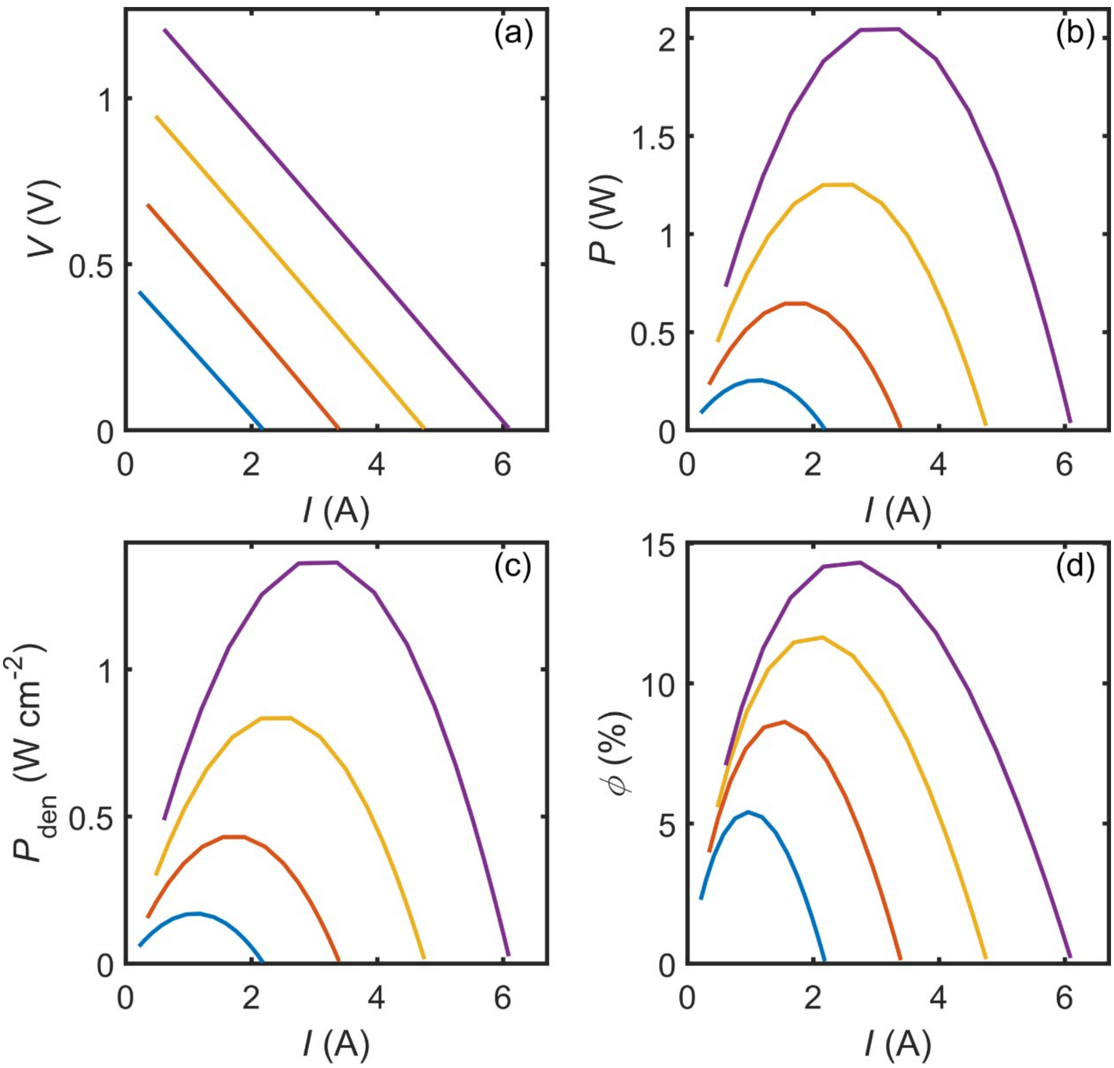

Fig. S84 Device simulation results of as-developed p-type $Ge_{0.89}Cr_{0.03}Sb_{0.08}Te$ and reported n-type $Ag_2Se_{1.08}$.[84] Generated (a) voltage (V), (b) output electrical power (P), (c) output electrical power density (P_{den}), and (d) conversion efficiency (ϕ) of the module under cold side temperature of 300 K and hot side temperatures of 480, 580, 680, and 780 K.

References

1. M. Hong, Z.-G. Chen, Y. Pei, L. Yang and J. Zou, *Phys. Rev. B*, 2016, **94**, 161201.
2. Y. Pei, Z. M. Gibbs, B. Balke, W. G. Zeier and G. J. Snyder, *Adv. Energy Mater.*, 2014, **4**, 1400486.
3. W. Liu, K. C. Lukas, K. McEnaney, S. Lee, Q. Zhang, C. P. Opeil, G. Chen and Z. Ren, *Energy Environ. Sci.*, 2013, **6**, 552-560.
4. J. Koenig, M. Winkler, T. Dankwort, A. L. Hansen, H. F. Pernau, V. Duppel, M. Jaegle, K. Bartholome, L. Kienle and W. Bensch, *Dalton Trans.*, 2015, **44**, 2835-2843.
5. S. Perumal, S. Roychowdhury, D. S. Negi, R. Datta and K. Biswas, *Chem. Mater.*, 2015, **27**, 7171-7178.
6. J. Li, Z. Chen, X. Zhang, Y. Sun, J. Yang and Y. Pei, *NPG Asia Mater.*, 2017, **9**, e353.
7. J. Li, X. Zhang, S. Lin, Z. Chen and Y. Pei, *Chem. Mater.*, 2016, **29**, 605-611.
8. M. Samanta and K. Biswas, *J. Am. Chem. Soc.*, 2017, **139**, 9382-9391.
9. M. Hong, Y. Wang, W. Liu, S. Matsumura, H. Wang, J. Zou and Z.-G. Chen, *Adv. Energy Mater.*, 2018, **8**, 1801837.
10. D. Wu, L. Zhao, S. Hao, Q. Jiang, F. Zheng, J. W. Doak, H. Wu, H. Chi, Y. Gelbstein, C. Uher, C. Wolverton, M. Kanatzidis and J. He, *J. Am. Chem. Soc.*, 2014, **136**, 11412-11419.
11. J. Li, X. Zhang, Z. Chen, S. Lin, W. Li, J. Shen, I. T. Witting, A. Faghaninia, Y. Chen, A. Jain, L. Chen, G. J. Snyder and Y. Pei, *Joule*, 2018, **2**, 976-987.
12. B. Poudel, Q. Hao, Y. Ma, Y. Lan, A. Minnich, B. Yu, X. Yan, D. Wang, A. Muto, D. Vashaee, X. Chen, J. Liu, M. S. Dresselhaus, G. Chen and Z. Ren, *Science*, 2008, **320**, 634-638.
13. J. Zhang, L. Song, S. H. Pedersen, H. Yin, L. T. Hung and B. B. Iversen, *Nat. Commun.*, 2017, **8**, 13901.

14. L. Hu, H. Wu, T. Zhu, C. Fu, J. He, P. Ying and X. Zhao, *Adv. Energy Mater.*, 2015, **5**, 1500411.
15. J. P. Dismukes, L. Ekstrom, E. F. Steigmeier, I. Kudman and D. S. Beers, *J. Appl. Phys.*, 1964, **35**, 2899-2907.
16. X. W. Wang, H. Lee, Y. C. Lan, G. H. Zhu, G. Joshi, D. Z. Wang, J. Yang, A. J. Muto, M. Y. Tang, J. Klatsky, S. Song, M. S. Dresselhaus, G. Chen and Z. F. Ren, *Appl. Phys. Lett.*, 2008, **93**, 193121.
17. Y. Tang, Z. M. Gibbs, L. A. Agapito, G. Li, H.-S. Kim, M. B. Nardelli, S. Curtarolo and G. J. Snyder, *Nat. Mater.*, 2015, **14**, 1223-1228.
18. Y. Tang, Y. Qiu, L. Xi, X. Shi, W. Zhang, L. Chen, S.-M. Tseng, S.-w. Chen and G. J. Snyder, *Energy Environ. Sci.*, 2014, **7**, 812-819.
19. Y. Tang, R. Hanus, S.-w. Chen and G. J. Snyder, *Nat. Commun.*, 2015, **6**, 7584.
20. W. Zhao, Z. Liu, P. Wei, Q. Zhang, W. Zhu, X. Su, X. Tang, J. Yang, Y. Liu, J. Shi, Y. Chao, S. Lin and Y. Pei, *Nat. Nano.*, 2016, **12**, 55-60.
21. W. Zhao, Z. Liu, Z. Sun, Q. Zhang, P. Wei, X. Mu, H. Zhou, C. Li, S. Ma, D. He, P. Ji, W. Zhu, X. Nie, X. Su, X. Tang, B. Shen, X. Dong, J. Yang, Y. Liu and J. Shi, *Nature*, 2017, **549**, 247-251.
22. X. Meng, Z. Liu, B. Cui, D. Qin, H. Geng, W. Cai, L. Fu, J. He, Z. Ren and J. Sui, *Adv. Energy Mater.*, 2017, **7**, 1602582.
23. H. Li, X. Su, X. Tang, Q. Zhang, C. Uher, G. J. Snyder and U. Aydemir, *J. Materiomics*, 2017, **3**, 273-279.
24. B. Duan, P. C. Zhai, L. S. Liu and Q. J. Zhang, *Mater. Res. Bull.*, 2012, **47**, 1670-1673.
25. X. Shi, J. Yang, J. R. Salvador, M. Chi, J. Y. Cho, H. Wang, S. Bai, J. Yang, W. Zhang and L. Chen, *J. Am. Chem. Soc.*, 2011, **133**, 7837-7846.
26. A. F. May, E. S. Toberer, A. Saramat and G. J. Snyder, *Phys. Rev. B*, 2009, **80**.

27. S. Wang, J. R. Salvador, J. Yang, P. Wei, B. Duan and J. Yang, *NPG Asia Mater.*, 2016, **8**, e285.
28. T. Berry, S. Ouardi, G. H. Fecher, B. Balke, G. Kreiner, G. Auffermann, W. Schnelle and C. Felser, *Phys. Chem. Chem. Phys.*, 2017, **19**, 1543-1550.
29. S. Chen, K. C. Lukas, W. Liu, C. P. Opeil, G. Chen and Z. Ren, *Adv. Energy Mater.*, 2013, **3**, 1210-1214.
30. G. Joshi, X. Yan, H. Wang, W. Liu, G. Chen and Z. Ren, *Adv. Energy Mater.*, 2011, **1**, 643-647.
31. Y. Xing, R. Liu, J. Liao, Q. Zhang, X. Xia, C. Wang, H. Huang, J. Chu, M. Gu, T. Zhu, C. Zhu, F. Xu, D. Yao, Y. Zeng, S. Bai, C. Uher and L. Chen, *Energy Environ. Sci.*, 2019, **12**, 3390-3399.
32. Y. Liu, H. Xie, C. Fu, G. J. Snyder, X. Zhao and T. Zhu, *J. Mater. Chem. A*, 2015, **3**, 22716-22722.
33. K. Xia, P. Nan, S. Tan, Y. Wang, B. Ge, W. Zhang, S. Anand, X. B. Zhao, G. J. Snyder and T. Zhu, *Energy Environ. Sci.*, 2019, DOI: 10.1039/C8EE03654C.
34. Y. Yan, W. Geng, J. Qiu, H. Ke, C. Luo, J. Yang, C. Uher and X. Tang, *RSC Adv.*, 2018, **8**, 15796-15803.
35. C. Chang, M. Wu, D. He, Y. Pei, C.-F. Wu, X. Wu, H. Yu, F. Zhu, K. Wang, Y. Chen, L. Huang, J.-F. Li, J. He and L.-D. Zhao, *Science*, 2018, **360**, 778-783.
36. A. T. Duong, V. Q. Nguyen, G. Duvjir, V. T. Duong, S. Kwon, J. Y. Song, J. K. Lee, J. E. Lee, S. Park, T. Min, J. Lee, J. Kim and S. Cho, *Nat. Commun.*, 2016, **7**, 13713.
37. H. Wang, Y. Pei, A. D. LaLonde and G. J. Snyder, *Proc. Natl. Acad. Sci. USA*, 2012, **109**, 9705-9709.
38. H. Wang, E. Schechtel, Y. Pei and G. J. Snyder, *Adv. Energy Mater.*, 2013, **3**, 488-495.

39. Z. Chen, B. Ge, W. Li, S. Lin, J. Shen, Y. Chang, R. Hanus, G. J. Snyder and Y. Pei, *Nat. Commun.*, 2017, **8**, 13828.

40. Q. Zhang, F. Cao, K. Lukas, W. Liu, K. Esfarjani, C. Opeil, D. Broido, D. Parker, D. J. Singh, G. Chen and Z. Ren, *J. Am. Chem. Soc.*, 2012, **134**, 17731-17738.

41. Q. Zhang, E. K. Chere, K. McEnaney, M. Yao, F. Cao, Y. Ni, S. Chen, C. Opeil, G. Chen and Z. Ren, *Adv. Energy Mater.*, 2015, **5**, 1401977.

42. A. D. LaLonde, Y. Pei and G. J. Snyder, *Energy Environ. Sci.*, 2011, **4**, 2090-2096.

43. L. Zhao, S. H. Lo, J. He, H. Li, K. Biswas, J. Androulakis, C.-I. Wu, T. P. Hogan, D.-Y. Chung, V. P. Dravid and M. G. Kanatzidis, *J. Am. Chem. Soc.*, 2011, **133**, 20476-20487.

44. S. N. Girard, J. He, C. Li, S. Moses, G. Wang, C. Uher, V. P. Dravid and M. G. Kanatzidis, *Nano Lett.*, 2010, **10**, 2825-2831.

45. H. Zhang, J. Luo, H.-T. Zhu, J.-K. Liang, L.-M. Ruan, Q.-L. Liu, J.-B. Li and G.-Y. Liu, *Acta Mater.*, 2012, **60**, 7241-7248.

46. J. Q. Li, X. X. Li, F. S. Liu, W. Q. Ao and H. T. Li, *J. Electron. Mater.*, 2013, **42**, 366-371.

47. X. X. Li, J. Q. Li, F. S. Liu, W. Q. Ao, H. T. Li and L. C. Pan, *J. Alloy. Compd.*, 2013, **547**, 86-90.

48. P. K. Rawat, B. Paul and P. Banerji, *ACS Appl. Mater. Interf.*, 2014, **6**, 3995-4004.

49. Q. Zhang, H. Wang, W. Liu, H. Wang, B. Yu, Q. Zhang, Z. Tian, G. Ni, S. Lee, K. Esfarjani, G. Chen and Z. Ren, *Energy Environ. Sci.*, 2012, **5**, 5246-5251.

50. J. Androulakis, I. Todorov, J. He, D.-Y. Chung, V. Dravid and M. Kanatzidis, *J. Am. Chem. Soc.*, 2011, **133**, 10920-10927.

51. L. Fu, M. Yin, D. Wu, W. Li, D. Feng, L. Huang and J. He, *Energy Environ. Sci.*, 2017, **10**, 2030-2040.

52. Y. Xiao, D. Wang, B. Qin, J. Wang, G. Wang and L.-D. Zhao, *J. Am. Chem. Soc.*, 2018, **140**, 13097-13102.
53. Y. Xiao, H. Wu, J. Cui, D. Wang, L. Fu, Y. Zhang, Y. Chen, J. He, S. J. Pennycook and L.-D. Zhao, *Energy Environ. Sci.*, 2018, DOI: 10.1039/C8EE01151F.
54. Z.-Z. Luo, X. Zhang, X. Hua, G. Tan, T. P. Bailey, J. Xu, C. Uher, C. Wolverton, V. P. Dravid, Q. Yan and M. G. Kanatzidis, *Adv. Funct. Mater.*, 2018, **28**, 1801617.
55. J. Zhang, D. Wu, D. He, D. Feng, M. Yin, X. Qin and J. He, *Adv. Mater.*, 2017, **29**, 1703148.
56. K. F. Hsu, S. Loo, F. Guo, W. Chen, J. S. Dyck, C. Uher, T. Hogan, E. K. Polychroniadis and M. G. Kanatzidis, *Science*, 2004, **303**, 818-821.
57. Z.-Z. Luo, S. Hao, X. Zhang, X. Hua, S. Cai, G. Tan, T. P. Bailey, R. Ma, C. Uher, C. Wolverton, V. P. Dravid, Q. Yan and M. G. Kanatzidis, *Energy Environ. Sci.*, 2018, **11**, 3220-3230.
58. Y. Xiao, H. Wu, W. Li, M. Yin, Y. Pei, Y. Zhang, L. Fu, Y. Chen, S. J. Pennycook, L. Huang, J. He and L.-D. Zhao, *J. Am. Chem. Soc.*, 2017, **139**, 18732-18738.
59. W. Liu, H. S. Kim, S. Chen, Q. Jie, B. Lv, M. Yao, Z. Ren, C. P. Opeil, S. Wilson, C.-W. Chu and Z. Ren, *Proc. Natl. Acad. Sci. USA*, 2015, **112**, 3269-3274.
60. W. Liu, X. Tan, K. Yin, H. Liu, X. Tang, J. Shi, Q. Zhang and C. Uher, *Phys. Rev. Lett.*, 2012, **108**, 166601.
61. W. Liu, J. Zhou, Q. Jie, Y. Li, H. S. Kim, J. Bao, G. Chen and Z. Ren, *Energy Environ. Sci.*, 2015, **9**, 530-539.
62. H. Ning, G. D. Mastrorillo, S. Grasso, B. Du, T. Mori, C. Hu, Y. Xu, K. Simpson, G. Maizza and M. J. Reece, *J. Mater. Chem. A*, 2015, **3**, 17426-17432.
63. K. Yin, X. Su, Y. Yan, C. Uher and X. Tang, *RSC Adv.*, 2016, **6**, 16824-16831.

64. V. K. Zaitsev, M. I. Fedorov, E. A. Gurieva, I. S. Eremin, P. P. Konstantinov, A. Y. Samunin and M. V. Vedernikov, *Phys. Rev. B*, 2006, **74**, 045207.
65. K. Imasato, S. D. Kang and G. J. Snyder, *Energy Environ. Sci.*, 2019, **12**, 965-971.
66. M. Wood, J. J. Kuo, K. Imasato and G. J. Snyder, *Adv. Mater.*, 2019, **31**, 1902337.
67. R. J. Mehta, Y. Zhang, C. Karthik, B. Singh, R. W. Siegel, T. Borca-Tasciuc and G. Ramanath, *Nat. Mater.*, 2012, **11**, 233-240.
68. Y. Min, J. W. Roh, H. Yang, M. Park, S. I. Kim, S. Hwang, S. M. Lee, K. H. Lee and U. Jeong, *Adv. Mater.*, 2013, **25**, 1425-1429.
69. S. Wang, G. Tan, W. Xie, G. Zheng, H. Li, J. Yang and X. Tang, *J. Mater. Chem.*, 2012, **22**, 20943-20951.
70. W.-S. Liu, Q. Zhang, Y. Lan, S. Chen, X. Yan, Q. Zhang, H. Wang, D. Wang, G. Chen and Z. Ren, *Adv. Energy Mater.*, 2011, **1**, 577-587.
71. X. Yan, B. Poudel, Y. Ma, W. S. Liu, G. Joshi, H. Wang, Y. Lan, D. Wang, G. Chen and Z. F. Ren, *Nano Lett.*, 2010, **10**, 3373-3378.
72. J. L. Cui, Y. Y. Li, Y. Deng, Q. S. Meng, Y. L. Gao, H. Zhou and Y. P. Li, *Intermetallics.*, 2012, **31**, 217-224.
73. L. Wang, P. Ying, Y. Deng, H. Zhou, Z. Du and J. Cui, *RSC Adv.*, 2014, **4**, 33897-33904.
74. L. Pan, D. Bérardan and N. Dragoe, *J. Am. Chem. Soc.*, 2013, **135**, 4914-4917.
75. S. Roychowdhury, T. Ghosh, R. Arora, U. V. Waghmare and K. Biswas, *Angew. Chem. Int. Edit.*, 2018, **57**, 15167-15171.
76. G. H. Zhu, Y. C. Lan, H. Wang, G. Joshi, Q. Hao, G. Chen and Z. F. Ren, *Phys. Rev. B*, 2011, **83**, 115201.
77. P. F. P. Poudeu, A. Guéguen, C.-I. Wu, T. Hogan and M. G. Kanatzidis, *Chem. Mater.*, 2010, **22**, 1046-1053.

78. M. Zhou, J.-F. Li, H. Wang, T. Kita, L. Li and Z. Chen, *J. Electron. Mater.*, 2011, **40**, 862-866.

79. Z.-Y. Li and J.-F. Li, *J. Electron. Mater.*, 2012, **41**, 1365-1369.

80. Q. Zhang, Y. Lan, S. Yang, F. Cao, M. Yao, C. Opeil, D. Broido, G. Chen and Z. Ren, *Nano Energy*, 2013, **2**, 1121-1127.

81. Z.-Y. Li and J.-F. Li, *Adv. Energy Mater.*, 2014, **4**, 1300937.

82. H. J. Wu, P. C. Wei, H. Y. Cheng, J. R. Deng and Y. Y. Chen, *Acta Mater.*, 2017, **141**, 217-229.

83. F. Drymiotis, T. W. Day, D. R. Brown, N. A. Heinz and G. J. Snyder, *Appl. Phys. Lett.*, 2013, **103**, 143906.

84. W. Mi, P. Qiu, T. Zhang, Y. Lv, X. Shi and L. Chen, *Appl. Phys. Lett.*, 2014, **104**, 133903.